Title	ATOMIC AND ELECTRONIC STRUCTURE OF ULTRATHIN IRON FILMS ON Si(111) AND MgO(001) SURFACES
Author(s)	Urano, Toshio
Citation	大阪大学, 1987, 博士論文
Version Type	VoR
URL	https://hdl.handle.net/11094/24525
rights	
Note	

ATOMIC AND ELECTRONIC STRUCTURE OF ULTRATHIN IRON FILMS ON Si(111) AND MgO(001) SURFACES

by Toshio URANO

DISSERTATION IN PHYSICS

THE OSAKA UNIVERSITY
GRADUATE SCHOOL OF SCIENCE
TOYONAKA, OSAKA

ATOMIC AND ELECTRONIC STRUCTURE OF ULTRATHIN IRON FILMS ON Si(111) AND MgO(001) SURFACES

by Toshio URANO

Synopsis

For studies of crystal surfaces and deposited thin films, a compound apparatus of angle resolved ultraviolet photoelectron spectroscopy (ARUPS), low energy electron diffraction (LEED) and Auger electron spectroscopy (AES), has been newly constructed. In addition, a simple semi-automatic system of LEED spot-tracing has been developed.

The following systems have been studied so far by use of the apparatus. The I-V curves of LEED of MgO(001) clean surfaces are obtained for three samples prepared by different heat treatments. The curves which are quite similar one another yield no appreciable surface relaxation in comparison with the theoretical ones obtained by dynamical calculations. Further, no change of the degree of the surface rumpling due to heat treatments is recognized.

Iron films deposited on Si(111)7x7 and MgO(001) surfaces grow layer-by-layer and form an Fe(111) and an Fe(001) epitaxial film at room temperature, respectively. The structure of iron films more than $\frac{1}{2}$ monolayer(ML) thickness on Si(111) surface has changed from 1x1 to 2x2 superstructure owing to annealing at temperatures higher than 400°C and at the same time a shift of iron d-band electronic state to the higher binding energy side has been observed by ARUPS.

By increasing the thickness iron film on MgO(001) surface begins to change from the body-centered tetragonal to the body-centered cubic structure at about 10 Å thickness and an expansion of valence-band width has been observed by AES simultaneously.

Contents

§2. Experimental apparatus

§3. Experimental results

3-2. Ultra-thin iron films on MgO(001) surface

§5. Electronic structure of iron films

§1. Introduction

In the past two decades, surface science has experienced a great progress, that is, various techniques for surface analysis have been developed and many surfaces (clean surfaces of single crystal which are reconstructed or not, and surfaces on which gas molecules or metal atoms are adsorbed) have been studied. Low energy electron diffraction (LEED) is the most fundamental technique for geometrical analysis of surfaces, that is, from a diffracted pattern on a fluorescent screen, two-dimensional symmetry of surface structure is easily obtained. In order to determine relative atomic positions, however, it is necessary that the spot intensity versus electron energy curves (so-called I-V curves) for several reciprocal rods are measured and those curves are compared with theoretical ones. Due to the strong coulomb interaction of electrons, the kinematical analysis is not useful except for a special case (that is, constant momentum transfer averaging (CMTA) method) and the dynamical analysis is necessary. In the case of very large two-dimensional unit cell in which many atoms are included, this calculation becomes very difficult. In addition, as a unique solution is not always obtained, it is desirable that a suitable structure model can be imagined from the other experimental or theoretical considerations. Because of these, particularly in Japan, the dynamical analysis has not been carried out except for a few studies1). But now, these situations have slightly changed, that is, (i) calculation speed of a large computer has become sufficiently fast, and (ii) a set of the computer program which can be extensively used has been published2,3). Consequently, it seems that extensive LEED analysis has become possible. One part of this paper is assigned to a construction of a simple semi-automatic system for

LEED spot-tracing and to a few applications for structure analysis of surfaces.

On the other hand, ultra-violet photoelectron spectroscopy (UPS) is a good method for analysis of the electronic properties of surfaces 4). In recent years, due to the development of the angle resolved (AR) spectroscopy technique, the dispersion relation of electrons in the single crystal surface5) and in the two-dimensional adsorbate layer on a crystal6) were studied by several researchers. Further, it is pointed out that the sit-site of the adsorbed atoms in the two-dimensional ordered layer can also be determined by ARUPS according to so-called the "symmetry analysis" of angular distribution and photon-polarization dependence of electron emission from the adsorbate7,8). Another part of this paper is assigned to an outline of design of an apparatus for ARUPS and to a preliminary experiment for iron deposited films on Si(111) surface.

The purpose of this paper is to clarify a microscopic atomic and electronic structure of ultra-thin iron films on Si(111) and MgO(001) surfaces by means of above mentioned experimental methods. Iron is an important material of catalysis for several chemical reactions, for example, NH_3 synthesis for industrial use. In order to study a microscopic reaction process on iron surface, well-defined clean surface must be prepared. Unfortunately, because a pure iron material is generated from iron-sulfide, sulfer atoms are taken into the bulk and often segregate on the surface after the heat treatment. Further, as an iron is very active, it is difficult to maintain a clean surface once obtained during a long time. Therefore, it has been tried to produce a clean surface by means of vapour deposition. Preliminary experiments revealed that iron films grew layer-by-layer both on Si(111) and MgO(001) surfaces, and Fe(111) and Fe(001) epitaxial films were produced, respectively.

On the other hand, from a viewpoint of the reliability and the durability of a semiconductor device and an aspect of interest for the Shottky barrier, investigations for microscopic behaviour of an interface of metal-semiconductor and/or metal-insulator are important. Although it is not now that iron is an important material for a device, the results obtained in this study are suggestive and the apparatus and the method must be applicable to study another metal-semiconductor/insulator interface. Although many papers have been published9), which describe behaviours of metal films on silicon, particularly, silicide formation at low temperature, only a few studies of iron films on Si have been made. For example, according to Lau et al. for 1000-1500 Å α-Fe film deposited on Si, a compound layer of FeSi is produced at 450°C and $FeSi_2$ formation begins at 550°C10).

It is interesting to know whether a thin film of a ferromagnetic material on a non-magnetic substrate is magnetic or not. Metal vapour deposition offers opportunities synthesizing metastable crystalline phases with novel physical properties. For example, fcc iron epitaxial films on Cu(001) with one to four monolayers have been stabilized11). According to Mate et al. the surface magnetization of a single layer of the ferromagnetic material is dependent on surface-bulk coupling12). Recently, strongly enhanced ferromagnetic moments are predicted for 3d bcc transition metals as overlayer on noble metals13). Comparing the calculated and measured valence band photoemission spectra of Fe on Ag(001), Binns et al. have found that the monolayer film is ferromagnetic14). In this study, however, it is not clear whether the deposited iron films are magnetic or not, and the problem remains as the future subject for research.

§2. Experimental apparatus

2-1. LEED-AES-ARUPS system

For studies of crystal surfaces and deposited thin films, a compound apparatus for ARUPS and LEED-AES has been developed. Ultraviolet photoelectron spectroscopy (UPS) is a useful method for analyzing the valence band electronic states of surfaces. Most troublesome point of this technique is that a photon source must be set up in a vacuum chamber due to an absorption effect of photons by a window material. Therefore, in case of use a discharge type photon source, a differential pumping system between a discharge tube and an ultrahigh vacuum chamber must be provided.

Angle resolved (AR) analysis of photoelectrons gives more valuable information for electronic structures than an angle integrated detection. For example, 2-dimensional dispersion relation and angular distribution of wave functions of electrons for ordered adsorbates can be obtained. In order to do an angle resolved detection, the electron analyzer should be moved around the sample. Since the solid angle for the detection is very small, an input lens system must be operated in optimum conditions in order to improve the detection efficiency.

Because angle resolved photoelectron spectroscopy is a relatively recent refinement of the photoemission technique, only a few research groups set up an apparatus in Japan and there are not many studies obtained with this technique. Although an apparatus equipped with these functions has been put on the market, it is very expensive. Therefore, a hand-made apparatus has been constructed.

2-1-1. Design of apparatus

The newly designed apparatus is indicated schematically in Fig.1. A 127° type cylindrical electron energy analyzer for ARUPS is settled on a turn table which is supported by small stainless-steel balls. It is driven at the rim of the table through a couple of crown gear and pinion. Almost all parts of the turn table and the drive mechanism consist of non-magnetic materials. The photoelectrons are analyzed in a horizontal plane. The UV photon source is also installed in the horizontal plane which is indicated as "Ist stage" in Fig.1.

In order to keep sufficiently wide space in which the 127° energy analyzer moves around the sample crystal, the electrodes of LEED-AES optics and a metal vapour evaporation source are installed in another horizontal plane indicated as "IInd stage" in Fig.1. A long-stroke sample manipulator transfers the sample between these stages. The performance of the sample manipulator newly constructed is as follows: The movable extent of three linear motions (x and y in a horizontal plane and z) are 25mm, 25mm and 200mm, respectively. The flip actuator mechanism built in the rotation feedthrough is translated to the rotation of the sample around the axis normal to its surface. It is rotated using a small rack-and-pinion mechanism.

At the bottom, it is connected to a sputter ion pump and a titanium sublimation pump which is cooled by liq.N_2. A large diameter clapper valve which is used to separate the pumps at the time of putting gas into the chamber is indicated in the figure.

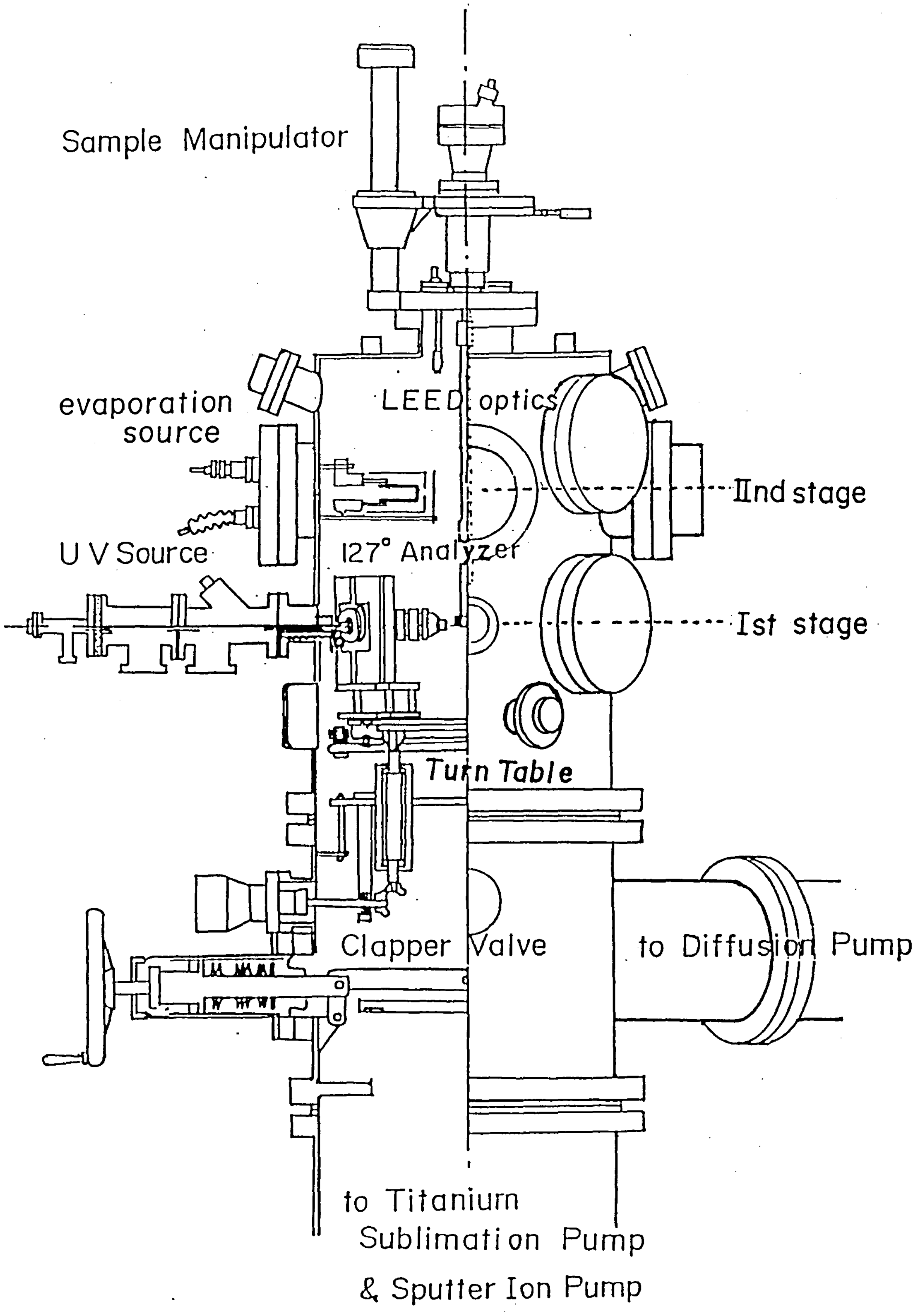

Fig.1 Schematic diagram of the experimental apparatus. At the "Ist stage" the 127°type electron energy analyzer on a turn table and the ultraviolet (UV) photon source are settled, and at the "IInd stage" LEED optics for LEED-AES and a metal vapour evaporation source are installed. A long stroke sample manipulator transfers the sample between these stages.

Schematic diagram of ultra-violet photon source newly constructed is shown in Fig.2. In order to avoid a direct discharge outside the capillary, the discharge path surrounding the capillary had to be obstructed by an insulator. A Teflon cylinder is used for this purpose. The discharge capillary is mechanically supported by this Teflon cylinder, and the discharge electrodes have no mechanical contact with the quartz capillary in order to avoid thermal shock, too. The polarity of the electric potential supplied to the discharge tube is decided on the stand point that the intensity ratio of He I (21.2eV) to He II (40.8eV) is superior when the electrode on the side near the sample is anode15). The flange on which the anode electrode is installed is cooled by water and an air cooled fin is fixed to the flange on which the cathode electrode is installed.

A differential pumping system was used between the UV source and the UHV chamber. In order to restrict the flow of helium gas along the UV light axis, three pylex glass capillaries were inserted

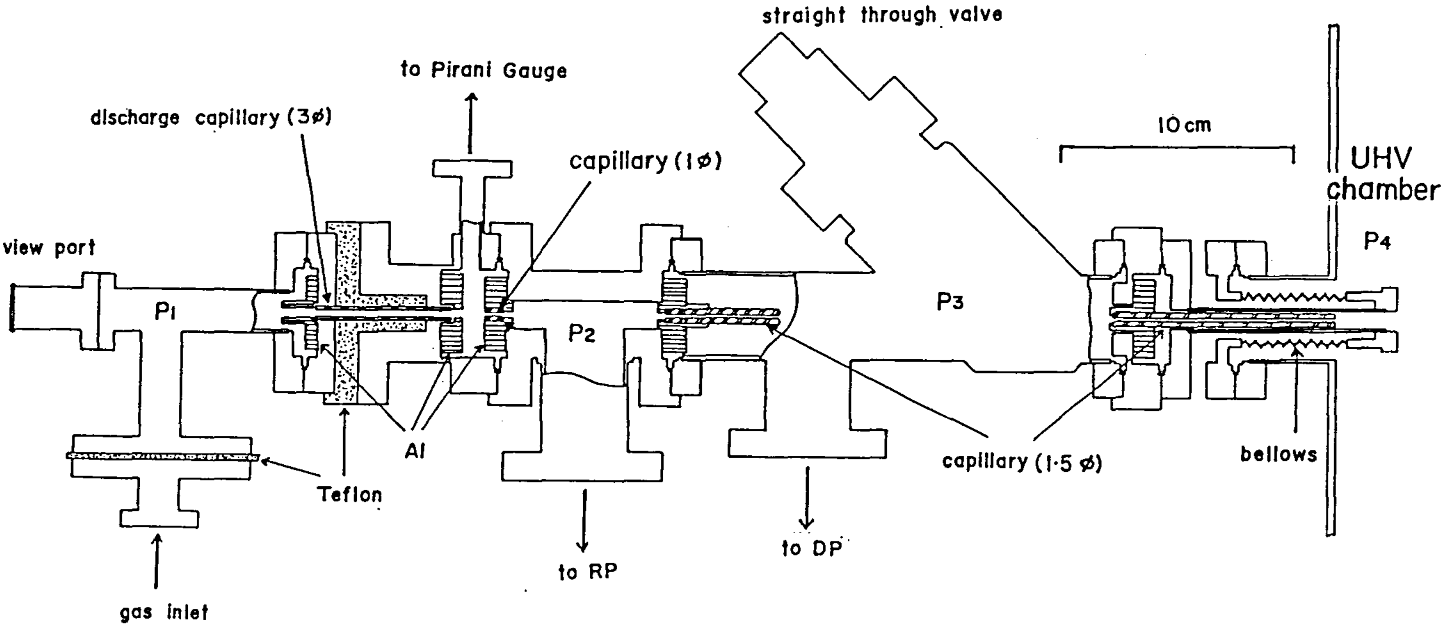

Fig.2 Schematic diagram of the UV photon source. A negative high electric potential (about 3 kV) is supplied to the end electrode on the left hand side. A differential pumping system is used between the discharge part and the UHV chamber. Typical pressures in operation are P_1=260 Pa, P_2=10 Pa,P_3=4x10^{-3}Pa, and P_4=8x10^{-7}Pa, respectively.

between the spaces of different pressures. The diameters of three capillaries are 1 mm, 1.5 mm and 1.5 mm, respectively. Each length of these capillaries is determined by numerical calculations according to the theory of vacuum technology. The length indicated in the figure is a good set which needs a minimum total capillary length. The first stage of a differential pumping system is evacuated by a rotary pump (300 l/min). The 2nd stage of it is evacuated by an oil diffusion pump (320 l/sec) with a cold trap. During the UPS experiment, when the pressure in the discharge capillary was 260 Pa, the typical pressures P_2 (measured by a Pirani gauge), P_3 and P_4 (indicated by ionization gauge) were about 10 Pa, 4×10^{-3} Pa and 8×10^{-7} Pa, respectively. The set angle of UV source to UHV chamber is adjusted using differential-pitch-screw mechanism. A couple of viewing ports which is fitted at the both ends of the light axis is very useful for this adjustment. One of them is indicated in the left hand side in Fig.2 and the other is fitted on UHV chamber at the opposite side of the UV source.

The photoelectrons are analyzed by a so-called "127°coaxial cylindrical analyzer" shown in Fig.3. This analyzer is composed of four parts, that is, "input lens", "deflector", "output lens" and "channeltron". The deflector is formed by a couple of cylindrical sector electrodes made by stainless steel, and its orbiting radius(R) is 25 mm. The actual sector angle is 119°in order to compensate for fringing field effect[16). The surface of inner walls of the sector electrodes (D_1 and D_2) and the two lens electrodes (L_7 and L_8) is covered by molybdenum foils because of the small emission yield of secondary electrons.[17)

Electric potentials of the electrodes are supplied by a several number of power sources. However, in order to change the energy pass-

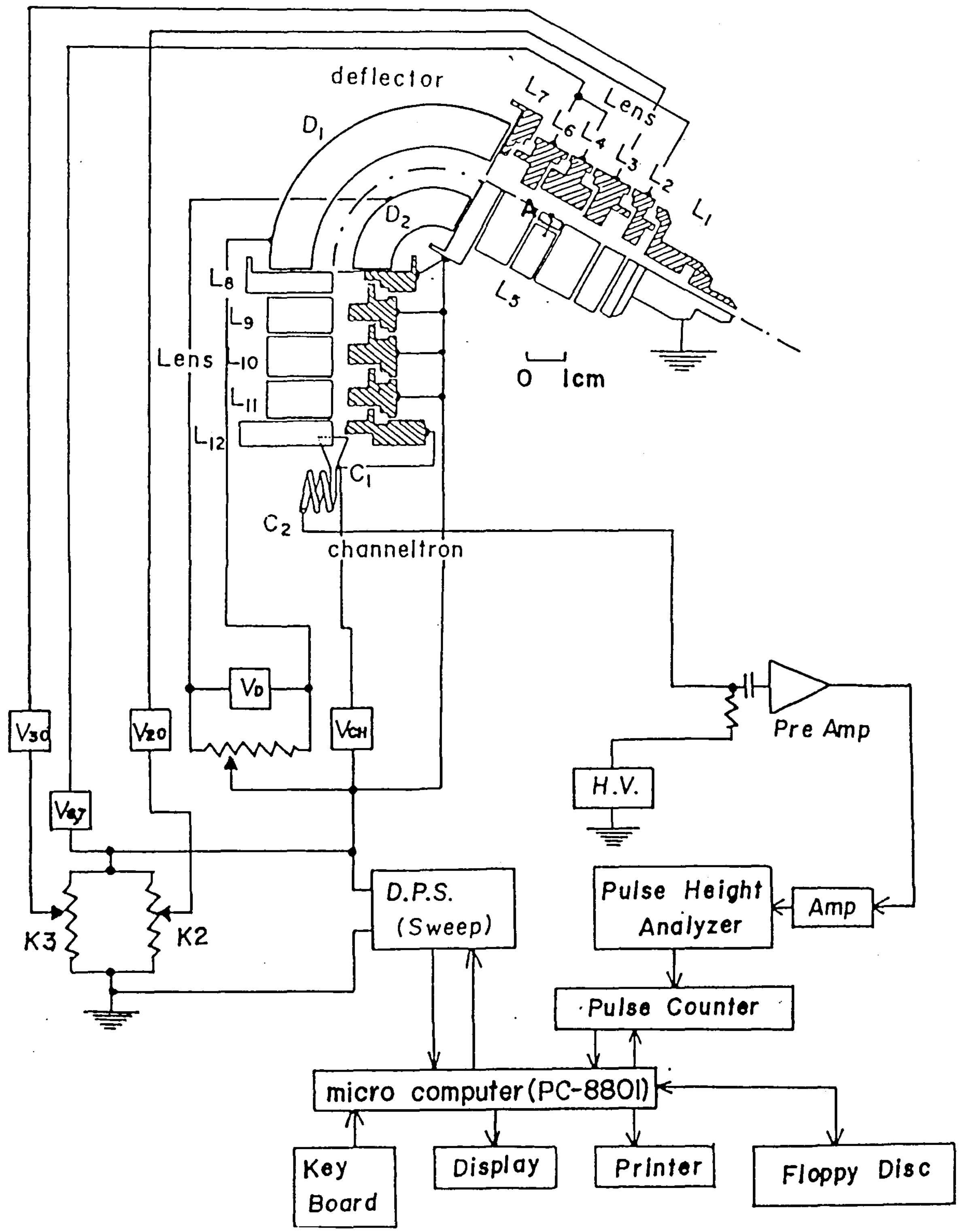

Fig.3 Composition of photoelectron energy analyzer system. The 127°type electron energy analyzer is composed of four parts, namely, "input lens", "deflector", "output lens", and "channeltron". In order to obtain an energy distribution curve electrons are retarded (or accelerated) in the input lens system in proportion to their energies by sweeping the output voltage of a conventional digital programable power source (D.P.S.). In order to remove the aberration the best operation of the input lens system has been determined experimentally (see text).

ing through the analyzer to obtain the spectrum curve, the output voltage of only one power source is changed. This source is a conventional digital programable power source (Kikusui, V50-0.5) indicated as "D.P.S." in Fig.3.

The photoelectrons are detected by a channeltron (Galileo Electro-optics, CEN4028). The pulse signal obtained by the channeltron is amplified and discriminated by a single-channel pulse height analyzer. Finally, the signal pulses are counted in each setting time period. Operations of the analyzer are controlled by a micro-computer (NEC, PC-8801). That is, the passing through energy is controlled and the counted number of the signal pulses at each step of the passing through energy is indicated by a cathode-ray display tube by digital or graphic expression and is saved in a floppy disc. When it is required, the data are treated numerically by the microcomputer.

LEED optics which is transferred from the old UHV system is a conventional 4-mesh LEED-AES electrodes shown in Appendix A.

2-1-2. Operation of photoelectron energy analyzer

To obtain an energy spectrum with electrostatic analyzer, two modes of the operation are well known[17)]. One of them is to sweep the difference of electric potentials of the cylindrical sector electrodes. The other mode is to sweep the retarding potential supplied to the input lens system under the fixed deflector potential. The former is simple, but is faulty in the change of absolute energy resolution. The latter is superior in case of searching for true energy distribution curve, and the analyzer shown in Fig.3 is operated according to this mode.

In the latter case, electrons are retarded (or accelerated) in the input lens system in proportion to their energies, but due to the aberration of the lens, the transparency of the analyzer must be changed depending on its retarding potential. In order to remove this aberration, the input lens system is usually composed more than three electrodes, because it is necessary that the image point is always on the slit of incidence. To obtain the best operation of the input lens system, the potentials, "V_{20}" and "V_{30}", and the ratios of potentiometers, k_2 and k_3 in Fig.3 have to be determined experimentally. The principle of focal properties and the method of determination for the best operation are shown in Appendix B. Finally, one of the best combination has been found as

$$k_2 = 0.20, \quad V_{20} = 12.65 \text{ V} ,$$
$$k_3 = 1.0 , \quad V_{30} = -1.85 \text{ V} .$$

The slit of incidence has a circular shape with a diameter of 0.5mm and the slit of outgoing has a rectangular shape, 0.5x10 mm, which is longitudinally long. Depending on the operation parameters of the deflector electrode, the resolving power of the analyzer is calculated according to a well known method[17)]. The value of FWHM, $\Delta E(=(w/R)E_0)$, shall be 100meV, when the passing through energy of the deflector, E_0, is 5eV, the orbiting radius, R, is 25mm and the two slits have above mentioned width, w. The resolving power is confirmed experimentally using a weak electron beam injected directly into the lens from an electron gun put at the "Ist stage" in Fig.1. The experimental value of FWHM was about 250meV which had small dependence on their energies. The difference between the two values is considered to be caused by an energy spread of thermal electrons.

Using the same electron gun, an angular resolution of the analyzer was measured. In rather high energy region, the values of FWHM of the analyzer was measured as about 2°.

For the output lens system, similar study was tried, but it gave very little improvement of the detect efficiency. Then, in this study the four electrodes of the output lens are connected at the same potential.

2-1-3. Experimental procedure

A typical experimental procedure is as follows: In order to obtain ultra-high vacuum(UHV), a diffusion pump (DP) (Edwards, E04; 600 l/sec) with a liq.N_2 trap (Vg, CCT100), a sputter ion pump (IP) (ANELVA, 912-7060; 400 l/sec) and a Ti-sublimation pump (TSP) with a liq.N_2 vessel are used. After rough evacuation, UHV chamber is baked out at about 150°C and evacuated by DP during 8 or 24 hours. When it is cooled down, the pump is changed to IP. The base pressure of this system is 2×10^{-8} Pa. During the UPS experiment, the DP system is again used to evacuate He gas.

He gas is introduced in the UV source through a variable leak valve (ULVAC, VLV-3) and the pressure in the discharge capillary is adjusted at about 260 Pa. The purity of He gas is 3N up. The open voltage of the power supply for glow discharge is about 3kV. The discharge current is about 200mA.

Residual magnetic field is cancelled by three sets of Helmholtz coils so that low energy electrons ejected from the electron gun run along a straight line.

Iron atoms are evaporated from an iron wire which is directly heated by electric current(Fig.1). Its diameter is 0.03 inches, and its purity is 4N(Material Research Corp., MARZ grade). In order to avoid an effect of impurities, the iron source is pre-heated at the same temperature during the film formation experiment for about ten hours. The temperature is measured by an optical pyrometer and the evaporation rate is monitored by a crystal monitor. A small glass plate is placed during the pre-heating at the position where a substrate crystal is placed during the actual experiment. This glass plate is taken out the chamber after the experiment and the thickness of the film deposited is measured with the interference stripes method to determine the absolute deposition rate.

2-2. Semi-automatic system of LEED spot-tracing

As is well known, the spot intensity versus electron energy relation curve (I-V curve) of LEED gives valuable information for the determination of the surface structure. The intensity of the (00) spot which corresponds to a mirror reflection can be measured easily, but the information obtained from this spot alone is insufficient to confirm the surface structure. The measurement of I-V curves for the other (hk) spot is a laborious task when it is carried out by the manual operation, because the spots move with the change of the electron energy. In order to measure quickly, various practical methods have been developed, namely, photograph18), spot-photometer19) and TV camera20,21) methods. We have constructed a simple semi-automatic system of the LEED spot-tracing based on a spot-photometer method22). Principal idea is as follows; the spot-photometer is driven manually, then the electron energy is changed automatically so that the spot moves to the position on the screen where it is measured by the photometer.

First, the following geometry of the arrangement is assumed.
(i) An incident electron beam impinges onto the crystal surface along its normal,
(ii) the impinging point lies exactly at the center of a sphere concentric with the fluorescent screen.
Moreover, it is assumed that
(iii) an effect of inner potential can be neglected.

In Fig.4, (a) the geometry among a sample, fluorescent screen and the position of an (hk) spot on the screen in real space, and (b) the condition of diffraction in reciprocal space are shown, respectively. If the axis of the photometer telescope is always kept parallel to incident beam, the LEED pattern which is observed by the photometer is the projection of the images on the fluorescent screen on a plane perpendicular to the incident beam. Under these conditions an (hk) spot moves inwards (or outwards) radially to the (00) spot along a straight line on the "plane" of projection with the increase (or decrease) of electron energy.

From the geometry in Fig.4(a), the relation,

$$r_0 \sin\phi = x_{hk}, \tag{2.1}$$

is obtained, where r_0 is the radius of a sphere defined by the segmental sphere of the fluorescent screen and x_{hk} is the distance of an (hk) spot from the (00) spot on the "plane" of projection. On the other hand, in reciprocal space, the relation,

$$1/d_{hk} = (1/\lambda)\sin\phi, \tag{2.2}$$

is obtained, where d_{hk} is a spacing of (hk) plane in the two-dimensional lattice. By using the de-Bloglie relation between a wavelength, λ, and electron energy, E,

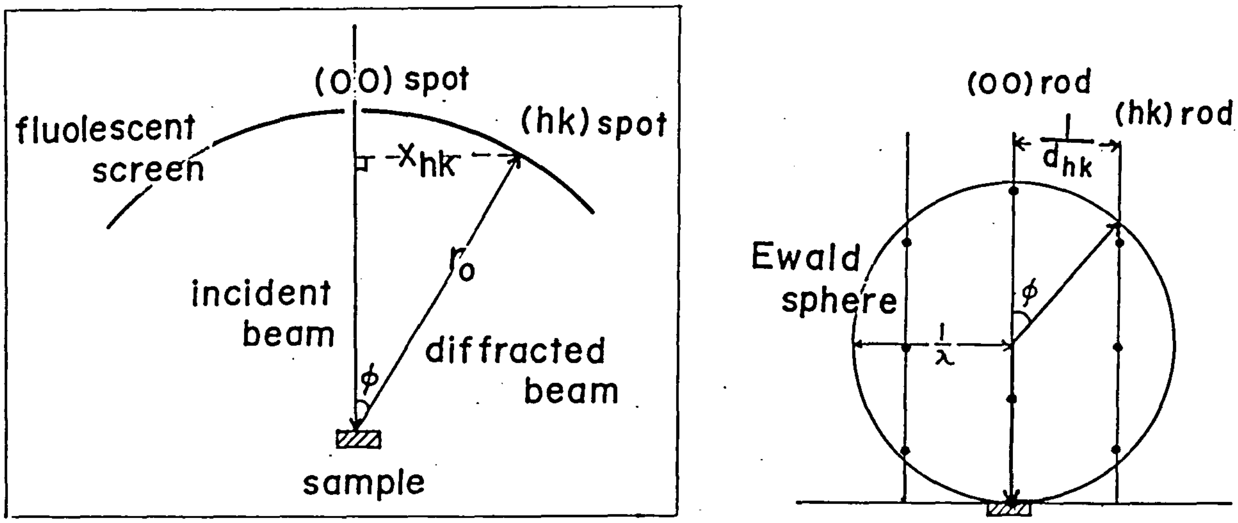

Fig.4 (a) Schematic diagram of the geometry of LEED arrangement in real space and (b) the diffraction condition in reciprocal space.

$$\lambda = h/\sqrt{2mE} \ , \qquad (2.3)$$

where m and h are the electron mass and the Planck constant, the following equation can easily be derived,

$$E = \frac{1}{2m} \left(\frac{r_0 h}{d_{hk}}\right)^2 \frac{1}{x_{hk}^2} \equiv A_{hk} \frac{1}{x_{hk}^2} \ . \qquad (2.4)$$

The electron energy, E, is proportional to the square inverse of the distance of an (hk) spot from the (00) spot on the "plane". A_{hk} takes a value specific to the indices (hk).

In order to obtain an electron energy, E, satisfying eq.(2.4), an electronic circuit specially built for this purpose is used (Fig.5). A linear motion potentiometer is connected mechanically to the photometer. Its resistance is set to be zero when the photometer is located pointing at the (00) spot. (in the case of the normal incidence, pointing at the center of drift tube of an electron gun). By this arrangement, the observed resistance is proportional to the distance, x, and is used for obtaining the electron accelerating voltage which is proportional to x^{-2} by means of an analog division circuit and a squaring circuit shown in Fig.5.

In order to find the proper value of A_{hk} in eq.(2.4), the photometer is driven to another properly chosen position, and the electron accelerating voltage is adjusted by VR_1 and VR_2 in Fig.5 so that the wanted (hk) spot is detected by the photometer. After this procedure the spot follows the photometer automatically, and an I(hk)-V curve can be obtained easily.

When the geometrical conditions assumed above are not realized, eq.(2.4) is not exactly satisfied. Those effects are discussed in Appendix C.

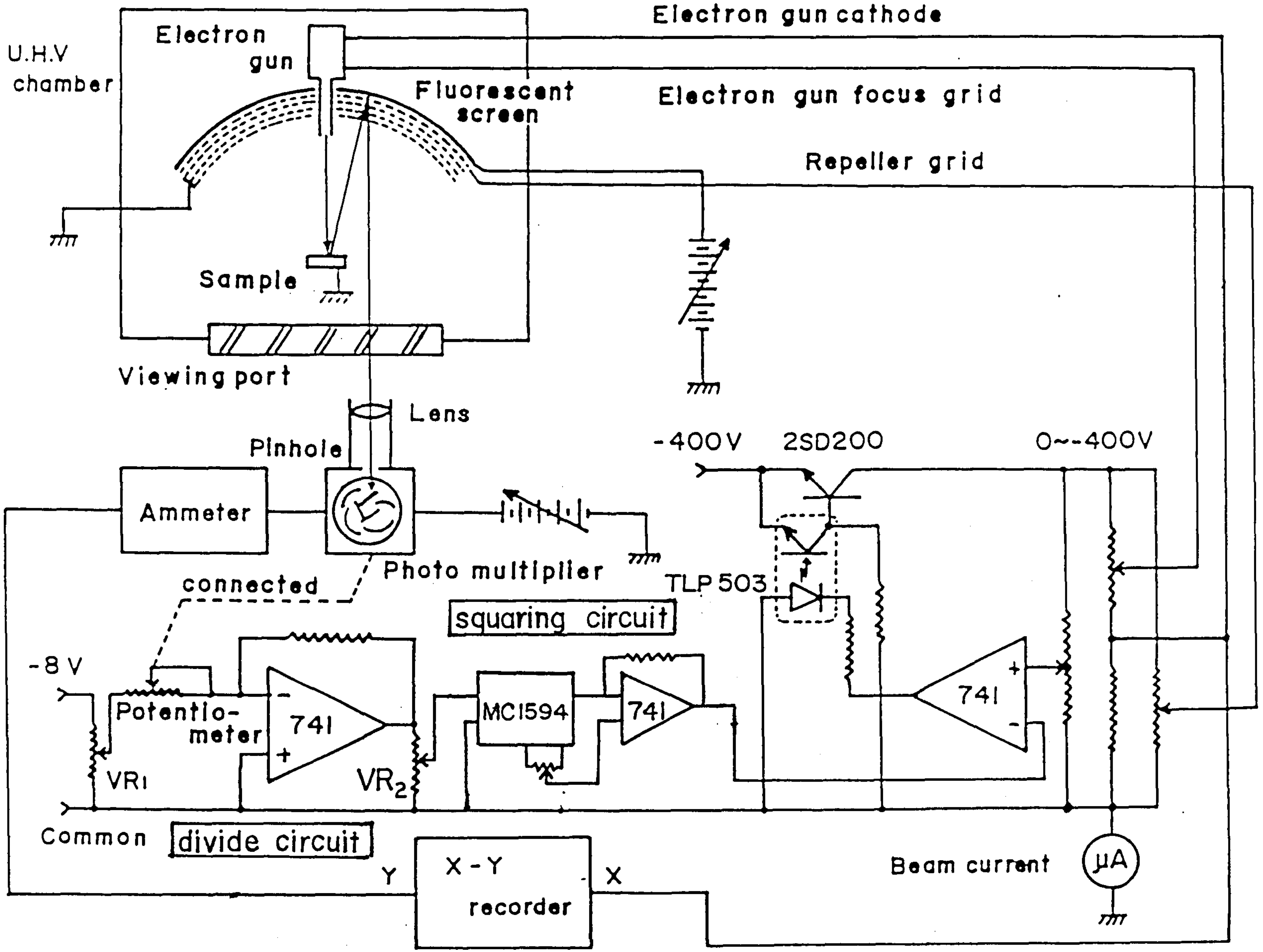

Fig.5 Schematic diagram of the semi-automatic system for measurement of the LEED spot intensity. In order to obtain an I-V curve, the spot-photometer is driven manually, then the electron energy is changed automatically so that the spot concerned moves to the position on the screen where it is measured by the photometer.

In this study the intensity of a primary electron beam current ejected from the electron gun was about 2μA and this value was practically not changed by the change of the electron energy in the region higher than 100eV. Though in the lower energy region the beam intensity increased gradually when the electron energy decreased down to about 30eV, the experimental I-V curves are not corrected in the whole energy region. Though the change of light transparency through the grids slightly deforms the profile of the experimental I-V curves, the obtained curves are not corrected. Although, due to these effects, relative intensity is slightly changed, in particular in lower energy region, the position of peaks and dips should not be affected.

§3. Experimental results

3-1. Ultra-thin iron films on Si(111) surface

In order to study the microscopic atomic and electronic structure of a deposited thin film, it is necessary to know the absolute quantity of the deposited material and the states of atoms, whether they are uniformly distributed or they gather together locally to form islands, etc. In order to see the states of atoms, it is useful to investigate a growth mode of deposited thin films.

It is well known that there are three basic modes of epitaxial growth from the vapour phase, namely, (a)Volmer-Weber (or three-dimensional island) growth mode, (b)Frank-van der Merwe (or layer-by-layer) growth mode and (c) Stranski-Krastanov growth mode. These growth modes are schematically shown in Fig.6. From a macroscopic point of view, the first mode should occur when the surface energy of the film material is larger than that of the substrate. The second and third modes should be typical for the case of a film having the low surface energy on a substrate with the high surface energy. If the

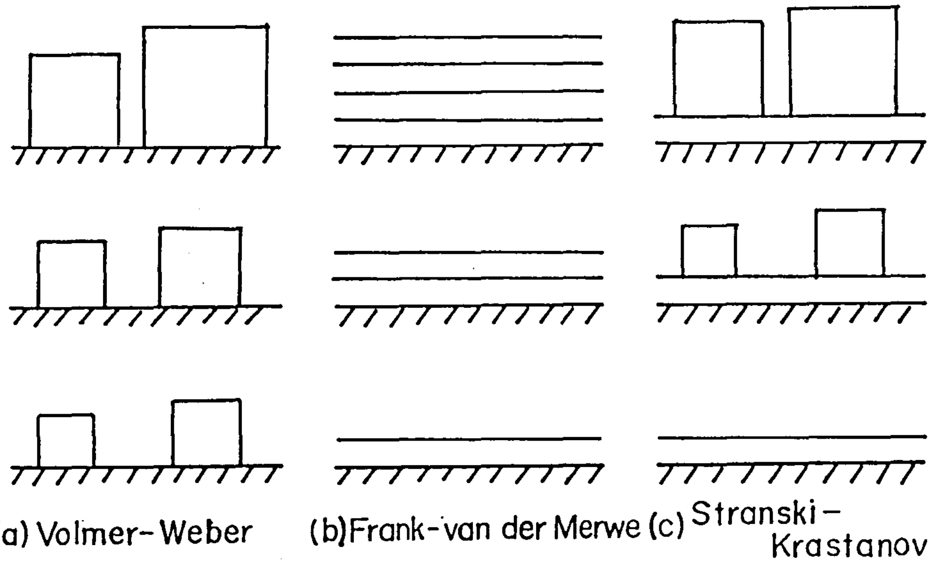

Fig.6 Three basic growth modes: (a) Volmer-Weber (3-D island) growth mode, (b) Frank-van der Merwe (layer-by-layer) growth mode and (c) Stranski-Krastanov growth mode.

strain energy in the film is small compared with the surface energy of the film material, the film should grow by the Frank-van der Merwe mechanism, and if the strain energy is large, the Stranski-Krastanov mode should occur. From a slightly different point of view, if a bonding between the film material and the substrate material is strong, Frank-van der Merwe growth mode should occur and if the interaction is weak, Volmer-Weber growth mode should occur.

Among various well-established techniques for surface analysis, the technique most frequently used for the determination of the growth mode is the Auger electron spectroscopy (AES). Two discrimination methods of growth modes based on AES have been proposed. These are the Palmberg's criterion23) and is the Jackson's criterion24), which will be explained in Appendix D.

3-1-1. Relation between Auger peak height and film thickness

The changing curves of the normalized Auger peak heights of Si-LVV(92eV) and Fe-MVV(48eV) during iron film formation on Si(111) surface at room temperature is indicated25) in Fig.7. The substrate sample for this experiment was a (111) face of B-doped p-type silicon with the resistivity of 0.1 Ωcm, which was mounted on a tuntalum sample holder. Sample cleaning was performed by heating it up to 1200°C. When the Auger signals corresponding to various average film thickness were measured, the deposition was continued without interruption, and the recording of the AES curves was repeated frequently. The substrate crystal was set at the cross point of two beam axis, that is, the axis of the electron beam and the axis of the evaporated iron beam which were perpendicular mutually. The incident angles of the two beams on the substrate surface were both 45°.

In Fig.7 two break points are shown in each curve and, according to the Jacksons's criterion (Appendix D), it is believed that the film grew in layer-by-layer mode. Since the deposition rate was about 0.43 (±0.05) Å per minute, the average thickness of the iron film at the first break point should be about 3.2 Å. This value is consid-

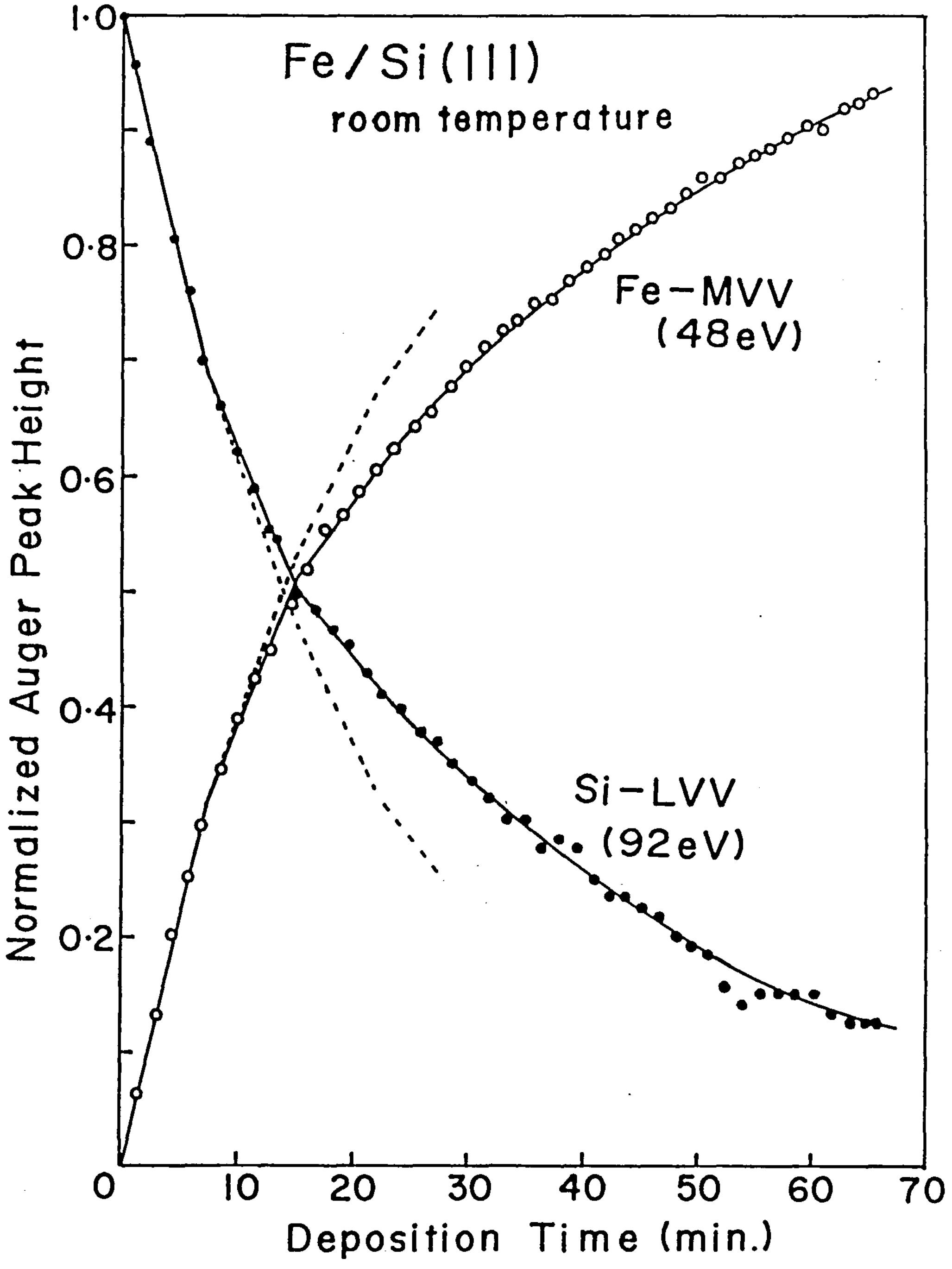

Fig.7 Normalized Auger amplitudes vs. time of deposition for iron film on Si(111) surface at room temperature. Deposition rate is about 0.43 Å/min. Two break points are shown in each curve. According to the Jackson's criterion, it is indicated that the film has grown in layer-by-layer growth mode.

erably larger than the largest interplanar distance in an iron bulk crystal. Therefore, the break point must correspond to the completion of a special structure. Since the 1x1 LEED pattern were observed during film formation and LEED pattern corresponding to an Fe(111) surface was observed finally, it is reasonable to consider that iron (111) plane was constructed from the very early stage of the film formation. The interplanar distance between the (111) planes in a bulk iron crystal is only 0.83 Å and no break point is indicated at such a thickness in Fig.7. However, because the density of iron atoms in the (111) plane is very sparse, the substrate crystal cannot be completely screened by one layer of the iron film. By a geometrical study using a marble model (Fig.8), it seems that three layers are necessary to screen the substrate, and that the break point in Fig.7 may correspond to the completions of three layers. If an iron film

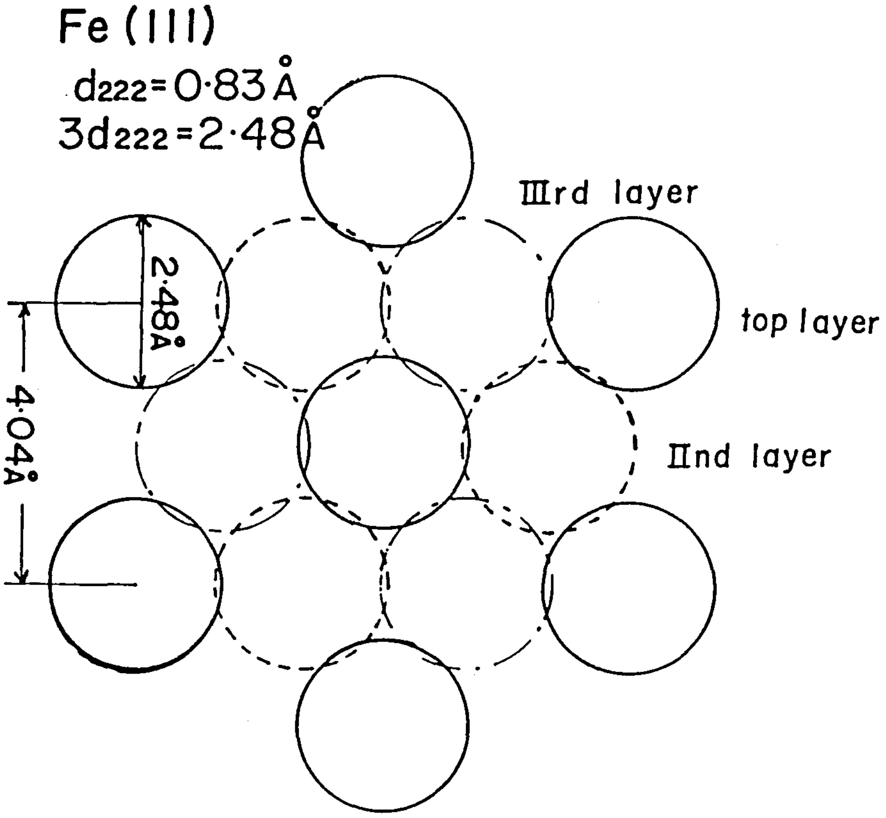

Fig.8 Marble model of the Fe(111) surface. Because the density of iron atoms in the (111) plane is low, three layers are necessary to screen the substrate.

grows in pseudomorphic, two-dimensional atomic distance decreases by 5% (from 4.04 Å to 3.84 Å), but it seems that the above mentioned model need not be changed.

Although an iron film predominantly grows on Si(111) surface in layer-by-layer growth mode, this model cannot explain the observed results completely, because the observed curve deviate markedly from the broken line in Fig.7 which indicates a change of Auger peak height in case of the ideal layer-by-layer growth. This seems to attribute to the film growth at low temperature. So that, if the temperature of the substrate is raised suitably, more perfect film growth is expected. On the other hand, it is well known that iron atoms are mixed with Si atoms and form a silicide at rather low temperatures$^{10)}$. Therefore, the change of the Auger peak height ratio (R) of Fe-MVV (48eV) to Si-LVV(92eV) with the annealing temperature was investigated and is shown in Fig.9. The substrate sample for this study was a (111) face of P-doped n-type silicon wafer with a resistivity of 10-20 Ω cm, mounted on a tuntalum sample holder. Sample heating was performed by electric current directly passing through the sample. The temperature was measured with both an optical pyrometer and a 3%ReW-25%ReW thermocouple. The parameter is the Auger peak height ratio (R_0) immediately after deposition. Iron atoms were deposited on the substrate at room temperature. Sample annealing was performed for 10 minutes at each temperature.

Figure 9 shows that the Auger peak height ratio (R) does not change up to 600°C in the case of R_0 smaller than 0.3. When R_0 is larger than 0.3, R decreases as temperature increases. Even if the initial R_0 values are different, each R approaches 0.3 asymptotically after the high temperature annealing. The Auger peak height ratio of 0.3 corresponds to about one atomic layer (1ML) film thickness of Fe(111) plane.

It is considered that the reduction of the Auger peak height ratio is caused by the following reasons: (i) Iron atoms were evaporated, (ii) iron atoms precipitated together and formed islands, and (iii) iron atoms infiltrated into the substrate. Of these, (i) is not possible because of the very low temperature. The suspected cause (ii) is also removed by the fact that the Fe-LMV (648eV) Auger peak (of which escape length is relatively long) height decreased as well as Fe-MVV (48eV) peak. Therefore, the cause (iii) seems to be most probable. According to Lau et al.[10)], it may be that silicon

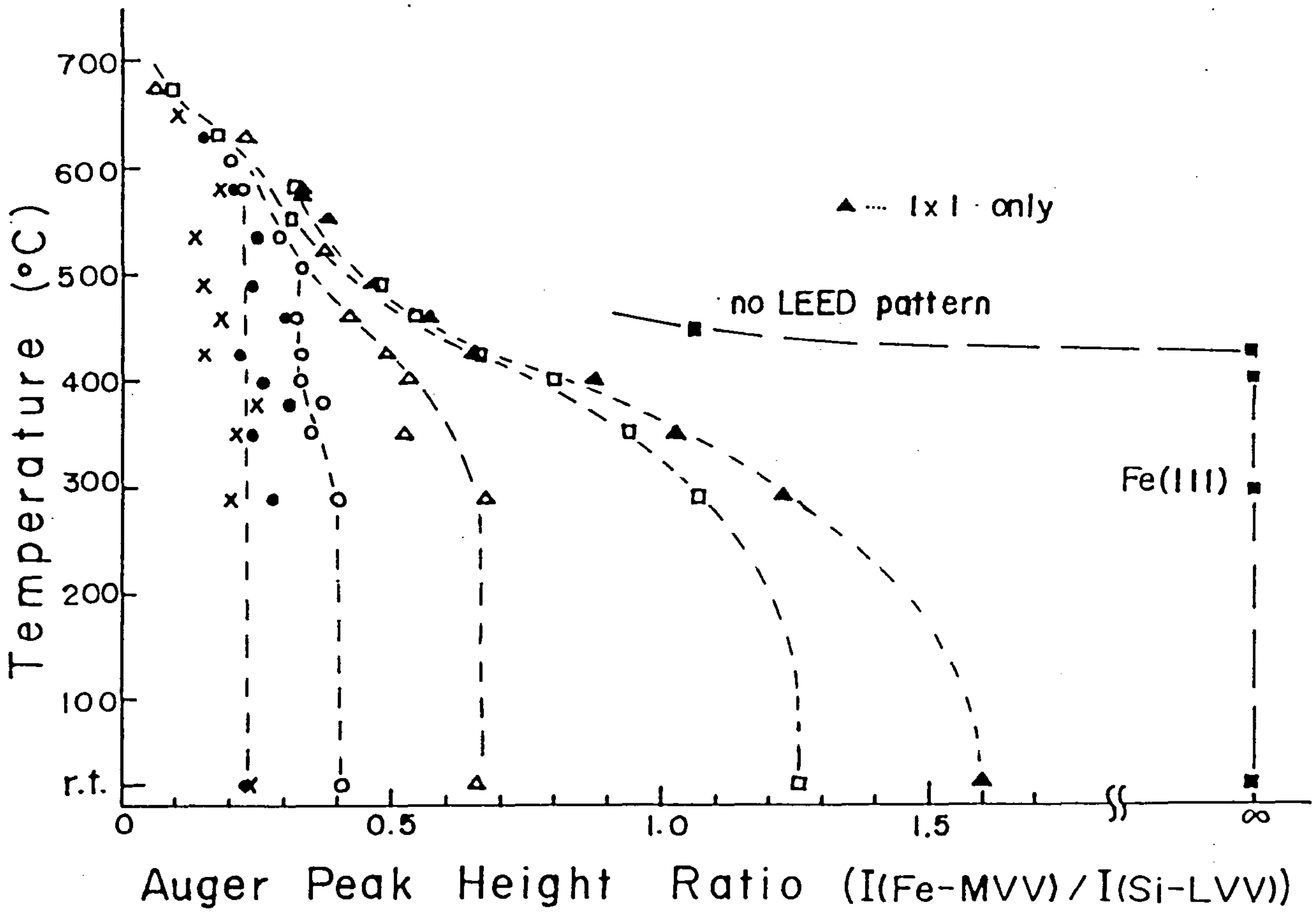

Fig.9 Change of the Auger peak height ratio of Fe-MVV(48eV) to Si-LVV(92eV) with increasing temperature of annealing. The parameter is the Auger peak height ratio immediately after the deposition at room temperature. The ratio of 0.3 corresponds to about one layer (ML) film thickness of Fe(111) plane. For example, the film indicated by a mark □ shows about 1.26 Auger peak height ratio after the deposition, and this value has changed to about 1.1 after annealing at 290°C during 10 minutes. This ratio has changed to 0.95 after annealing at 350°C and so on.

atoms move toward iron rather than iron atoms move toward silicon.

For all films, Auger peak height ratio began to reduce again at temperatures higher than 600°C.

3-1-2. LEED I-V curves of iron films

Results of LEED observation for iron films on Si(111) during the heat treatment are summarized as follows:

(i) For films of which R_0 was more than 0.1 (0.3 ML), 7x7 extra spots disappeared and 1x1 pattern appeared immediately after the deposition at room temperature.

Moreover, after heat trearment,

(ii) films of which R_0 was less than 0.15 (0.5 ML) showed 1x1 spots only up to about 600°C.

(iii) For the films of which R_0 was more than 0.5 ML, LEED pattern changed from 1x1 to 2x2 (or 2x1 of three domains) superstructure

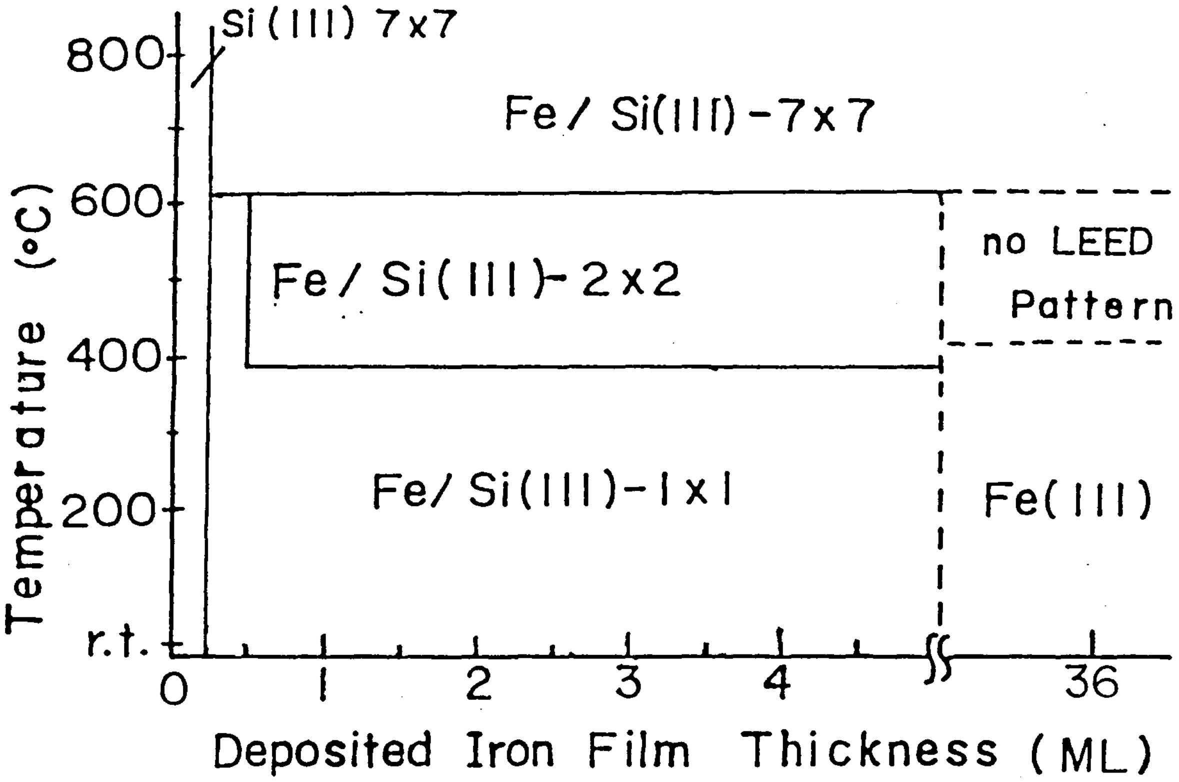

Fig.10 Two-dimensional phase diagram of deposited iron film on Si(111) surface. Iron atoms have been deposited at room temperature, and each film has been annealed at higher temperatures successively. The average thickness of iron film is indicated by that immediately after the deposition.

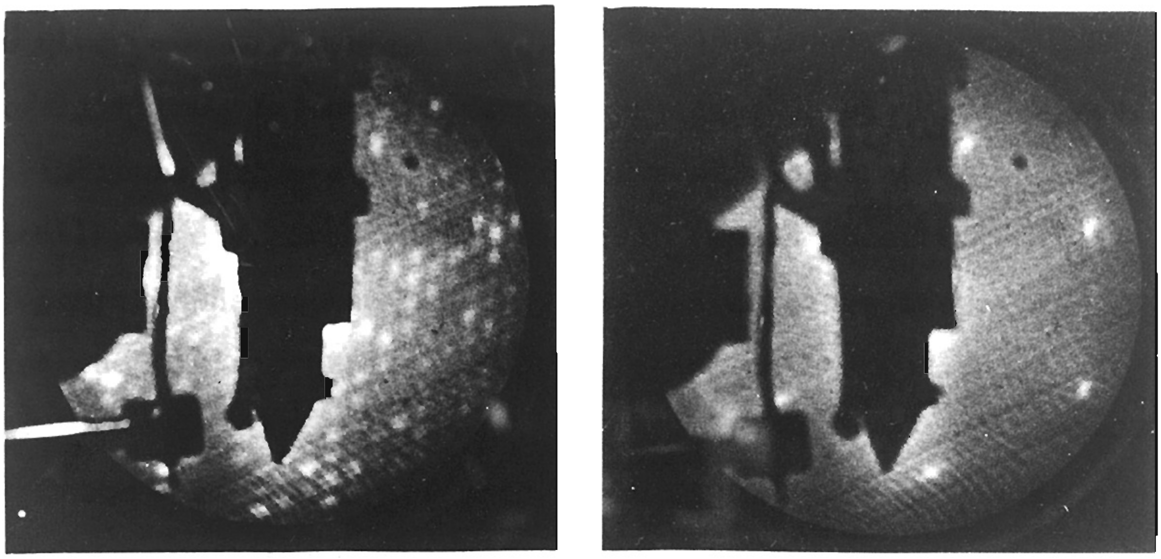

Si(111) 7x7
E = 76 eV

Fe/Si(111) 1x1
E = 81 eV

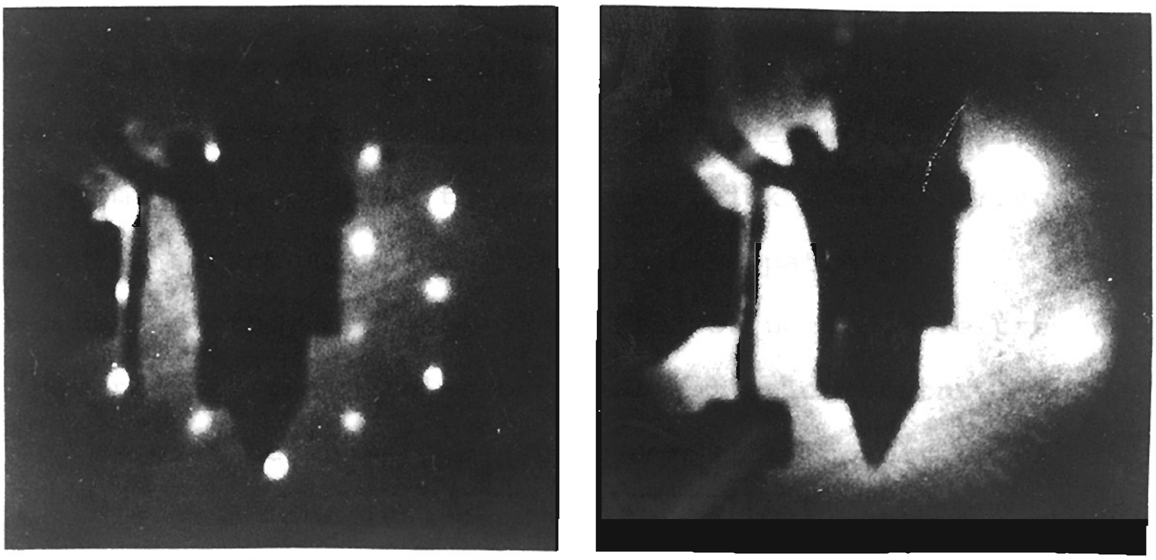

Fe/Si(111) 2x2
E = 71 eV

Fe(111) / Si(111)
E = 152 eV

Fig.11 Typical LEED patterns of iron film on Si(111); (a) clean Si(111)7x7 surface, (b) 1x1 Fe/Si(111), (c) 2x2 Fe/Si(111), (d) Fe(111) epitaxial film on Si(111).

after annealing at temperatures higher than 400°C.

(iv) For very thick films (about 36 ML=30 Å), LEED pattern of Fe(111) surface at low temperature disappeared after annealing at temperatures higher than 440°C.

(v) For all films, 7x7 superstructure began to appear again at 600°C.

On the basis of experimental results mentioned above the two-dimensional phase diagram shown in Fig.10 can be constructed. In Fig.11, photographs of the typical LEED patterns are shown.

From the AES and LEED study, the following conclusion can be reached.

(I) For films less than one atomic layer (1ML) thick, iron atoms remain on the surface up to 600°C.

(II) For films more than 1ML thick, the most of iron atoms remains on the surface after annealing at temperatures lower than 400°C and form an epitaxial film which shows 1x1 LEED pattern.

(III) For films more than 1ML thick, iron atoms infiltrate into the substrate after annealing at temperatures higher than 400°C, leaving iron atoms corresponding to about 1ML thick on the surface, and form a special structure which shows 2x2 LEED pattern.

In order to study a change of surface structure more precisely and to compare with the results of dynamical calculations, LEED I-V curves for several beams were measured under the condition of the incident angle of 5° for (00) beam and normal incidence for other beams. Measurements were performed for the films annealed both at about 350°C and at about 500°C, respectively, at the stages of various film thicknesses. As the Si(111) surface has a three-fold symmetry, it is enough to measure within one-third in circumference. In addition to (00) beam, 6 beams of (01), (10), (02), (20), (11) and $(2\bar{1})$ shown in Fig.12 schematically were measured for the films annealed at 350°C. 6 fundamental beams listed above and 9 extra beams of $(0\ \frac{1}{2})$, $(\frac{1}{2}\ 0)$, $(0\ \frac{3}{2})$, $(\frac{3}{2}\ 0)$, $(\frac{1}{2}\ \frac{1}{2})$, $(1\ \overline{\frac{1}{2}})$, $(\frac{1}{2}\ 1)$, $(1\ \frac{1}{2})$ and $(\frac{3}{2}\ \overline{\frac{1}{2}})$ were measured for the films annealed at 500°C. In Figs.13-15, experimental I-V curves for fundamental beams of (01) and (10) ((a)350°C annealed and (b)500°C annealed, respectively) and 3 extra beams of $(0\ \frac{1}{2})$, $(\frac{1}{2}\ 0)$ and $(\frac{1}{2}\ \frac{1}{2})$ at the stage of various film thicknesses are shown. In Fig.16 experimental I-V curves for (00) beam are also shown.

From these figures it can be considered as follows:

(i) By comparison of (01) beam and (10) beam, it is obvious that every film for various thicknesses has not six-fold but three-fold symmetry.

(ii) From the I-V curves of fundamental beams for the films annealed

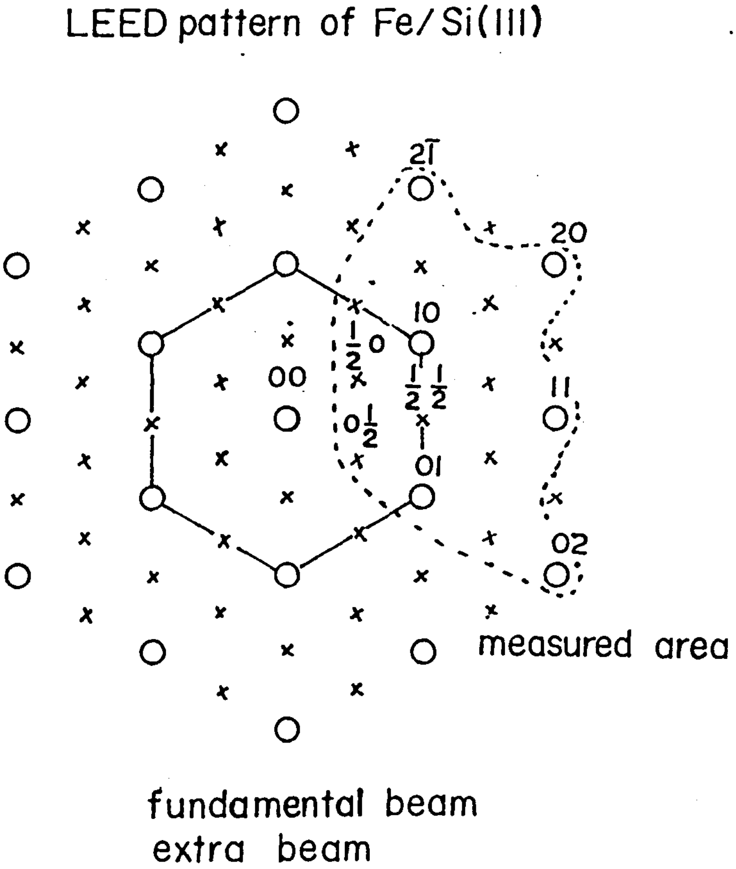

Fig.12 Schematic indication of LEED spots indices.

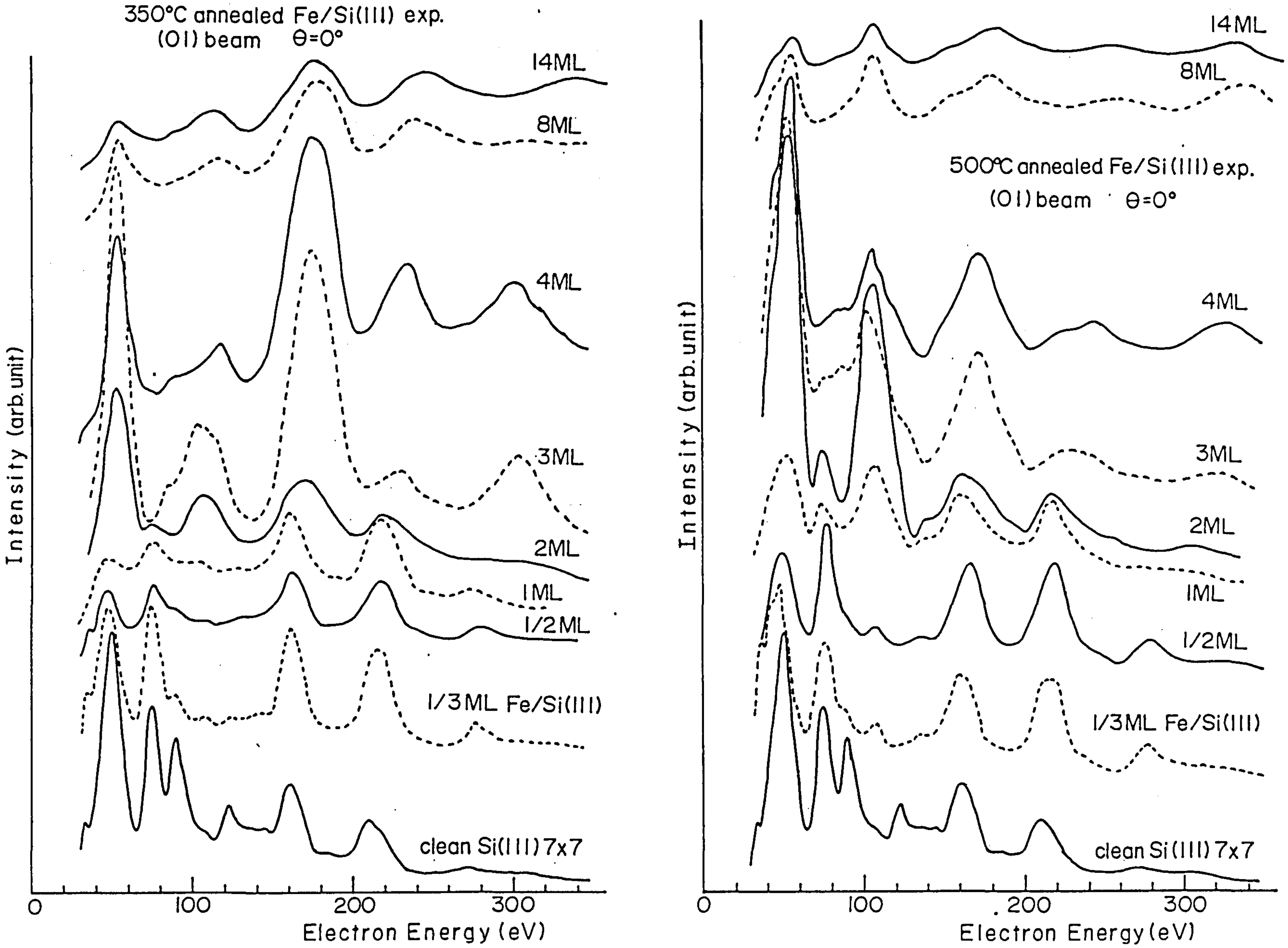

Fig.13 Experimental I-V curves of (01) beam for iron films of various thicknesses on Si(111), (a) for the films annealed at 350°C, (b) for the films annealed at 500°C, respectively, after the deposition at room temperature.

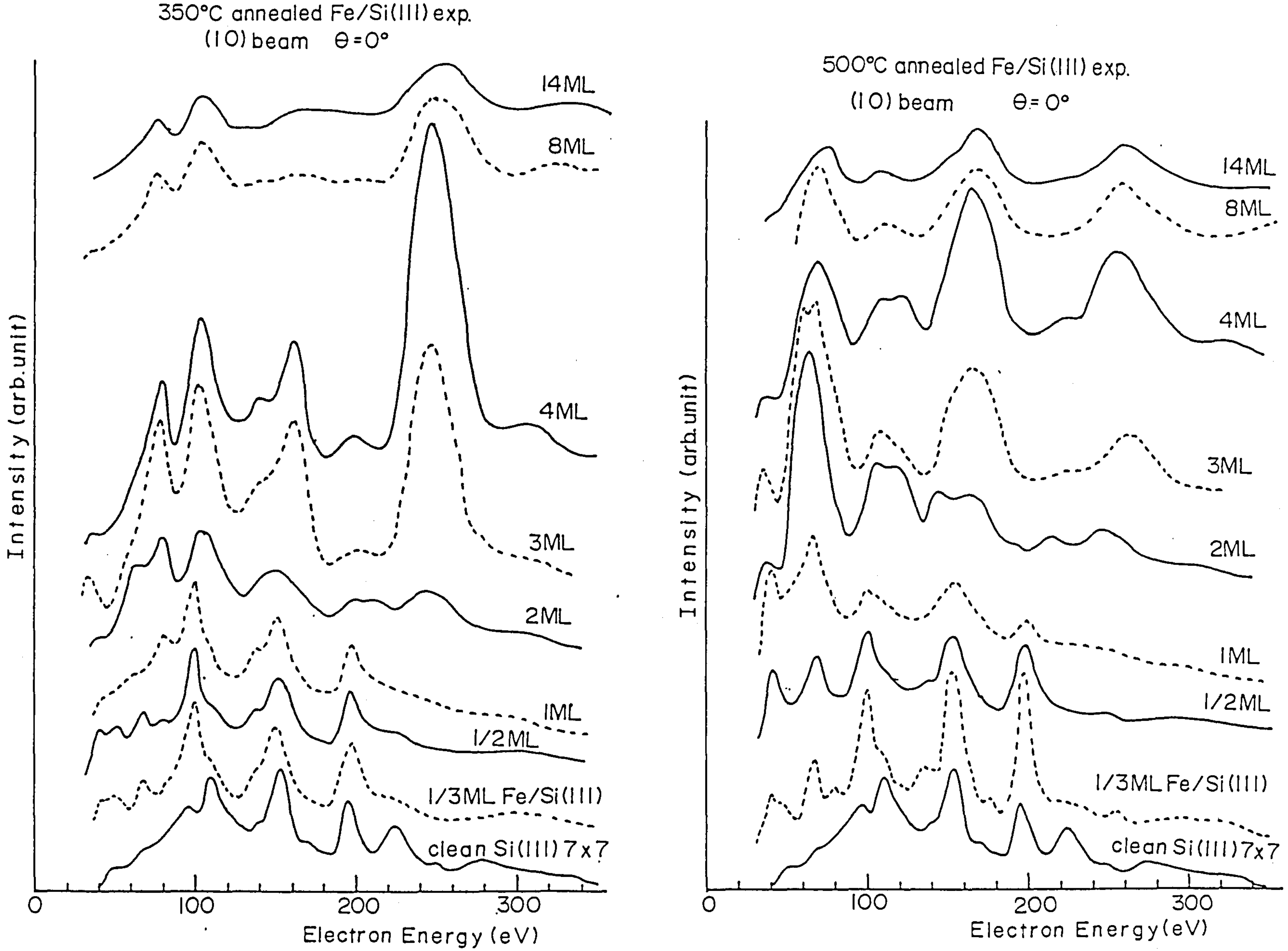

Fig.14 Experimental I-V curves of (10) beam for iron films of various thicknesses on Si(111), (a) for the films annealed at 350°C, (b) for the films annealed at 500°C, respectively, after the deposition at room temperature.

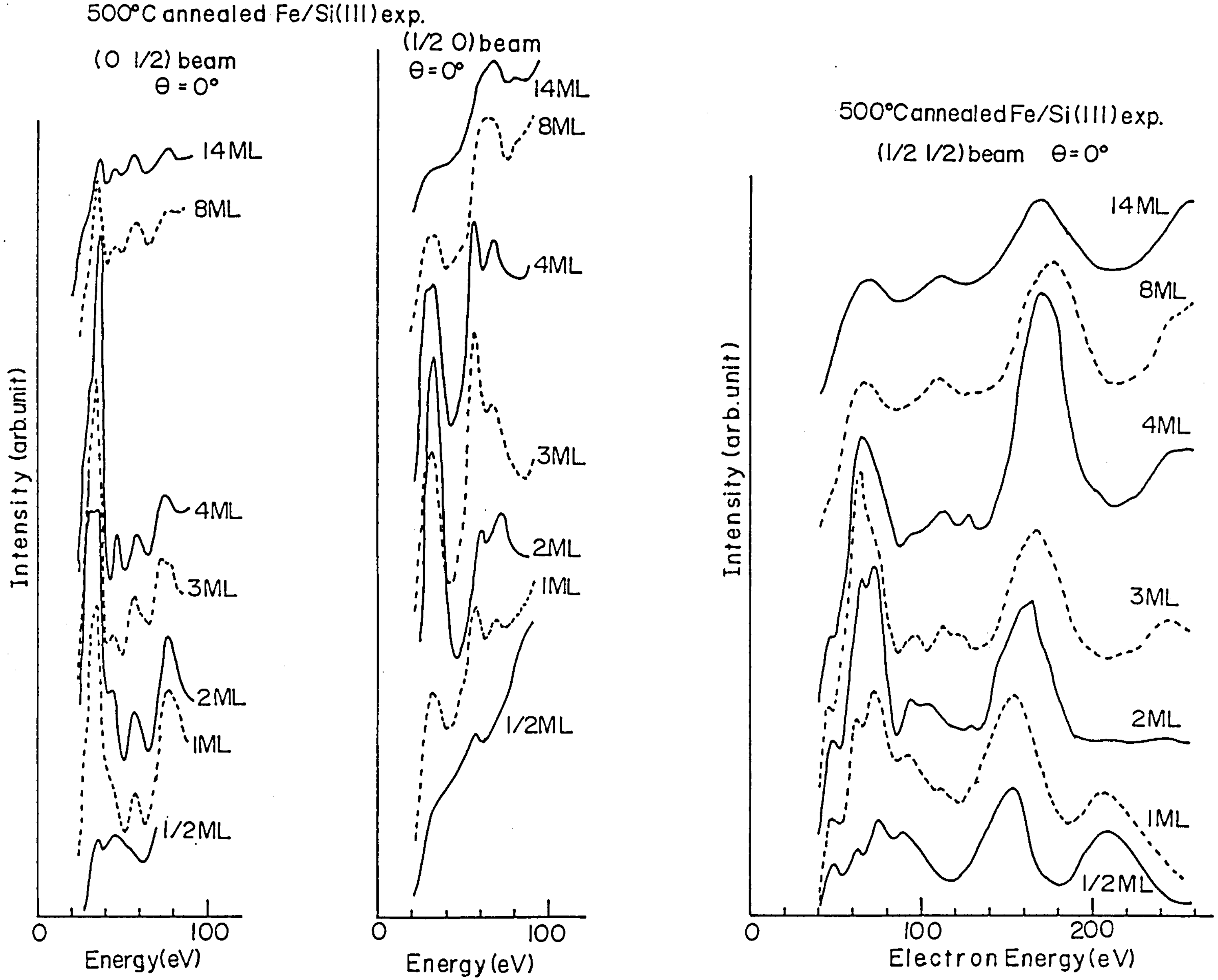

Fig.15 Experimental I-V curves of extra beams of $(0,\frac{1}{2})$, $(\frac{1}{2},0)$ and $(\frac{1}{2},\frac{1}{2})$ for iron films of various thicknesses on Si(111) annealed at 500 C after the deposition at room temperature.

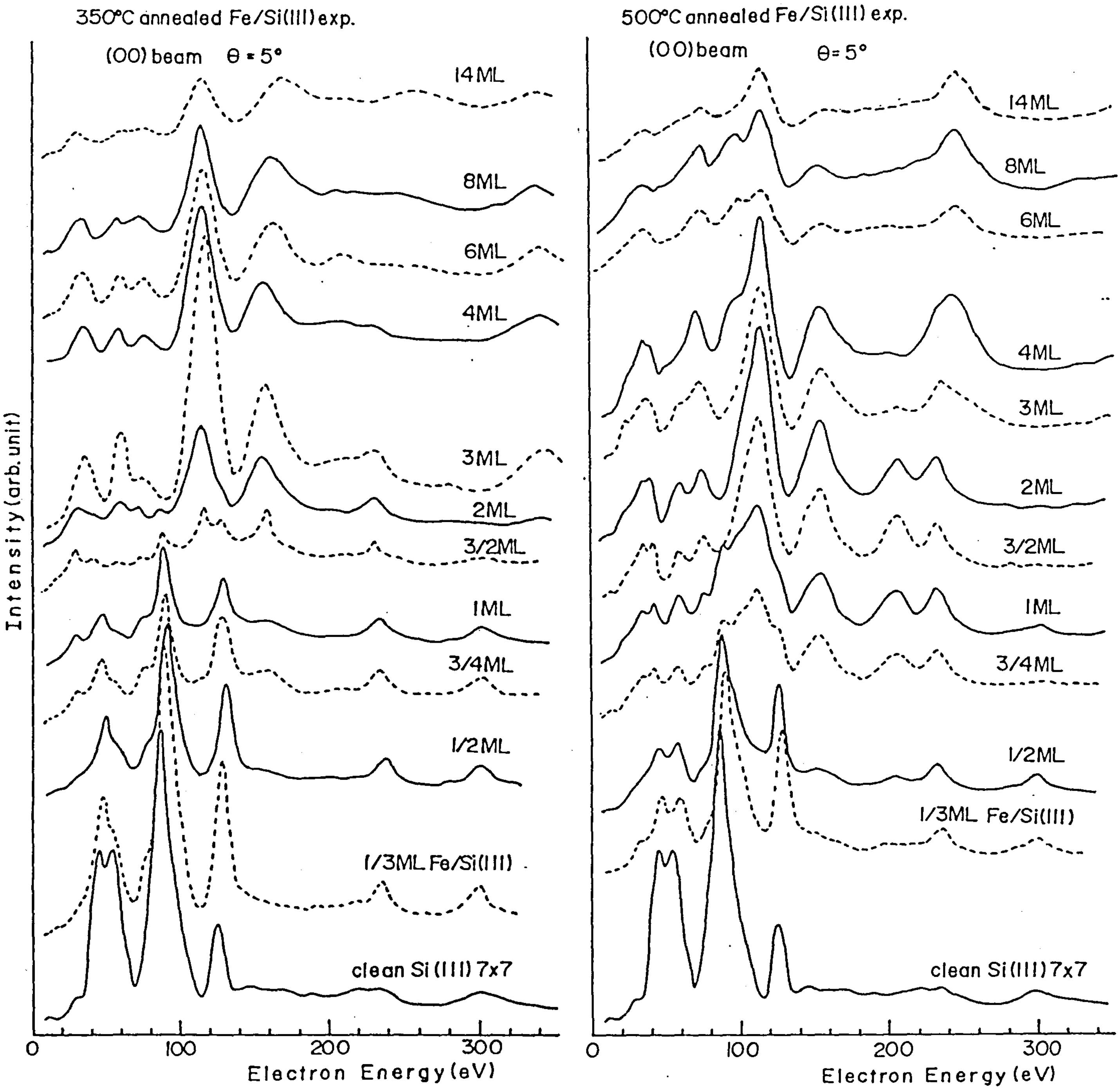

Fig.16 Experimental I-V curves of (00) beam for iron films of various thicknesses on Si(111) under the condition of $\theta=5^\circ$ and $\phi=0^\circ$, (a) for the films annealed at 350°C, (b) for the films annealed at 500°C, respectively, after the deposition at room temperature.

at 350°C, it seems in a rough estimation that there are two different stages of film growth for less than 1ML and more than 2ML. Moreover, strictly speaking, for the films more than 8ML, though the whole profiles do not change from those for the films less than 6ML, peak intensities has decreased and peak position has slightly shifted. These results correspond to the viewpoint indicated in the previous paper[25].

(iii) For the films less than 1ML, as the positions of peaks are rather similar to those of clean Si(111) 7x7 surface, it seems that the iron film is pseudomorphic and grows as if iron atoms behave just like Si atoms.

(iv) From the I-V curves of fundamental and extra beames for the films annealed at 500°C, it seems that there are clear differences between I-V curves for the films of $\frac{1}{2}$ML and those for the films more than $\frac{3}{4}$ML.

(v) For the films less than $\frac{1}{2}$ML annealed at 500°C, the I-V curves are similar to those for the films annealed at 350°C.

(vi) For the films more than $\frac{3}{4}$ML, it seems that the surface structures are fundamentally the same with on another, however, for thick films it seems that excess iron atoms remain on the surface or the crystalinity is slightly bad .

(vii) As the extra spots corresponding to 2x2 structure are strong at the stage of 2 or 3 ML, it seems that the structure which produces 2x2 LEED pattern is not peculiar to only the outermost surface layer but peculiar to that includes somewhat the inside.

These knowledges are helpful in construction of structure models.

3-1-3. ARUPS spectra

As the structure of iron films on Si(111) has changed owing to the heat treatment, it is expected that the electronic state should change too. The ARUPS spectra were measured for the films of various average thicknesses. Angle setting of the light beam and the detector is shown in Fig.17 schematically. The angle resolved measurement can be performed in various modes[7)] described in detail in Appendix E. In this study three different experimental geometries of the measurement were chosen, these are, (a) normal incidence of light ($\alpha=0^\circ$) and emission angle $\theta=30^\circ$, (b) $\alpha=0^\circ$, $\theta=60^\circ$ and (c) glancing incidence of light ($\alpha=60^\circ$), $\theta=30^\circ$. The plane on which the light beam and electron beam are included is parallel to $[1\bar{1}0]$ axis for all geometries, that is, $\phi=0^\circ$. All iron films were annealed for 10 minutes at about 350 °C after deposition and all showed 1x1 LEED pattern. Measured spectra are shown in Fig.18.

What is evident from the figure is the growth of Fe d-state at about 1eV of the binding energy, E_B. The width of the d-state even at the stage of 2.5Å thickness, however, is rather wide in com-

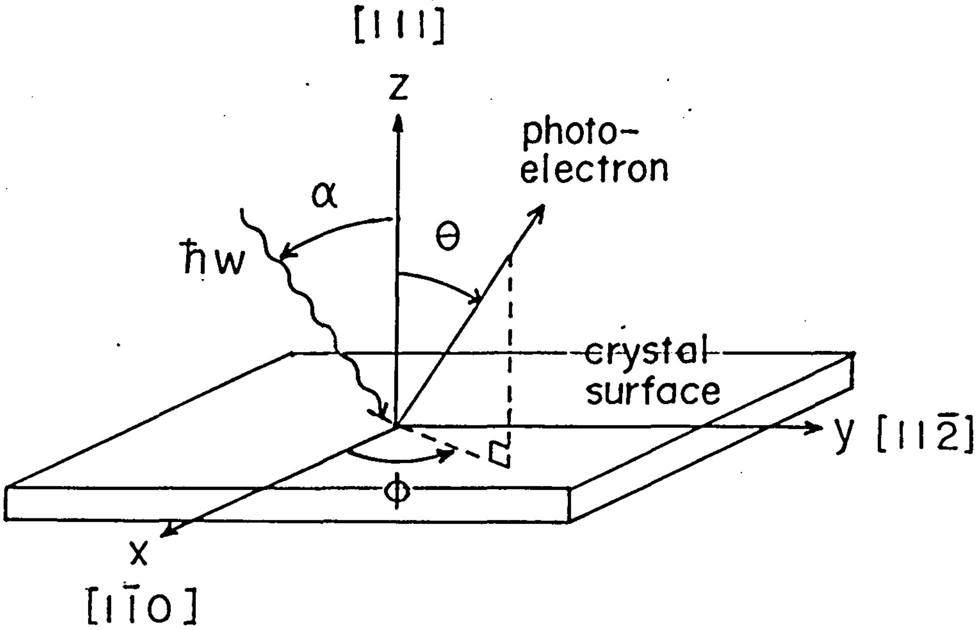

Fig.17 Angle setting of the light beam and the detector.

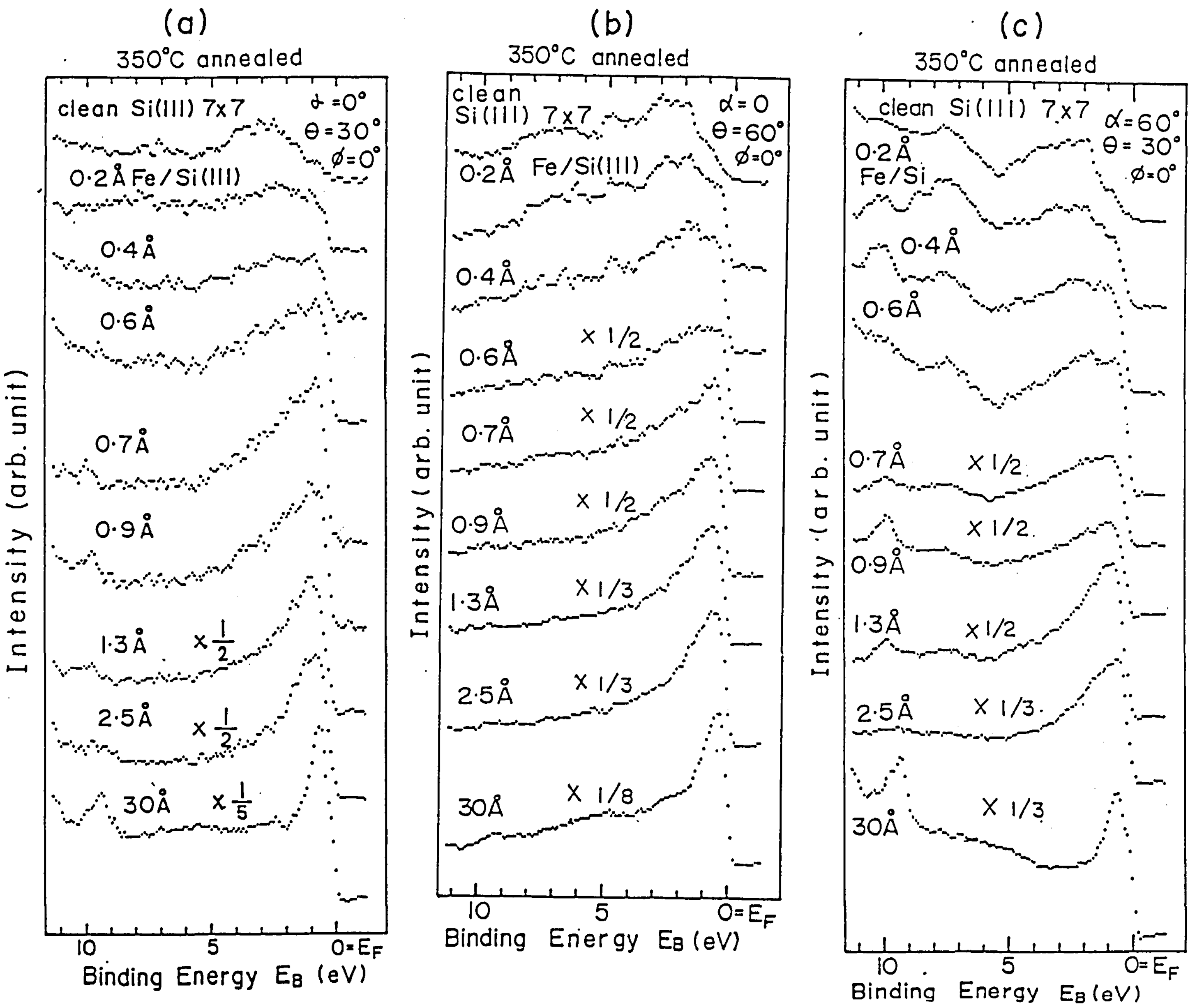

Fig.18 ARUPS spectra measured for the films of various average thicknesses which have been annealed at low teperature (350°C), (a) normal incidence of light ($\alpha=0°$) and emission angle:$\theta=30°$, (b) $\alpha=0°$ and $\theta=60°$, (c) glancing incidence of light ($\alpha=60°$) and $\theta=30°$.

parison with that of the thick film. The spectrum of the 30 Å-thick film is very similar to that obtained from the Fe(111) surface of a single crystal by Schulz et al.[26)]. Binns et al. indicated that an iron monolayer on Ag(001) was ferromagnetic because of the wide photoemission spectrum of the valence band (about 4.5eV) due to the exchange splitting[14)]. From this point of view, as the spectrum is not so wide, it is likely that the iron monolayer film on Si(111) is not ferromagnetic.

Although the intensities of the spectra corresponding to the same film thickness in Figs.18(a) and (b) are similar to each other, that in Fig.18(c) is considerably dissimilar to the corresponding spectra in (a) and (b) (Figures (a) and (b) are plotted in the same scale of the intensity, while (c) is compressed to one-fifth scale). Firstly, the absolute intensity in (c) is large. Secondly, although the relative intensity of d-band state for the film of 2.5Å thickness shown in Figs.18(a) and (b) is rather small in comparison with that for the thick film (30 Å), a similar magnitude of intensity is seen for the corresponding films in (c). These show that the case of glancing angle incidence of light is rather sensitive to the surface than the case of normal incidence. Although the surface area on which light beam irradiates increases twice for glancing incidence ($\alpha=60^\circ$) compared with that for normal incidence, it cannot be explained by this reason only.

The photo-ionization cross section is in proportion to the square of the transition matrix element with dipole approximation,

$$\frac{d\sigma}{d\Omega} = |\langle\psi_f|\vec{A}\cdot\vec{p}|\psi_i\rangle|^2, \tag{3.1}$$

where ψ_i and ψ_f represent the initial and final states, respectively,

$\vec{A}$ is the vector potential of incident photons, and $\vec{p}$ denotes the linear momentum operator. Therefore, it can be said that the photoionization cross section at the surface is very sensitive to the polarization vector of photons.

Next, the films were annealed again for 10 minutes at about 500°C. LEED pattern of the films with the average thickness more than 0.6 Å changed to 2x2 superstructure. ARUPS spectra measured under the same experimental geometry as in Fig.18 are shown in Fig.19. The corresponding spectra for the same film thickness and for the same experimental geometry are similar to one another. The precise difference should be discussed in sec.5-1.

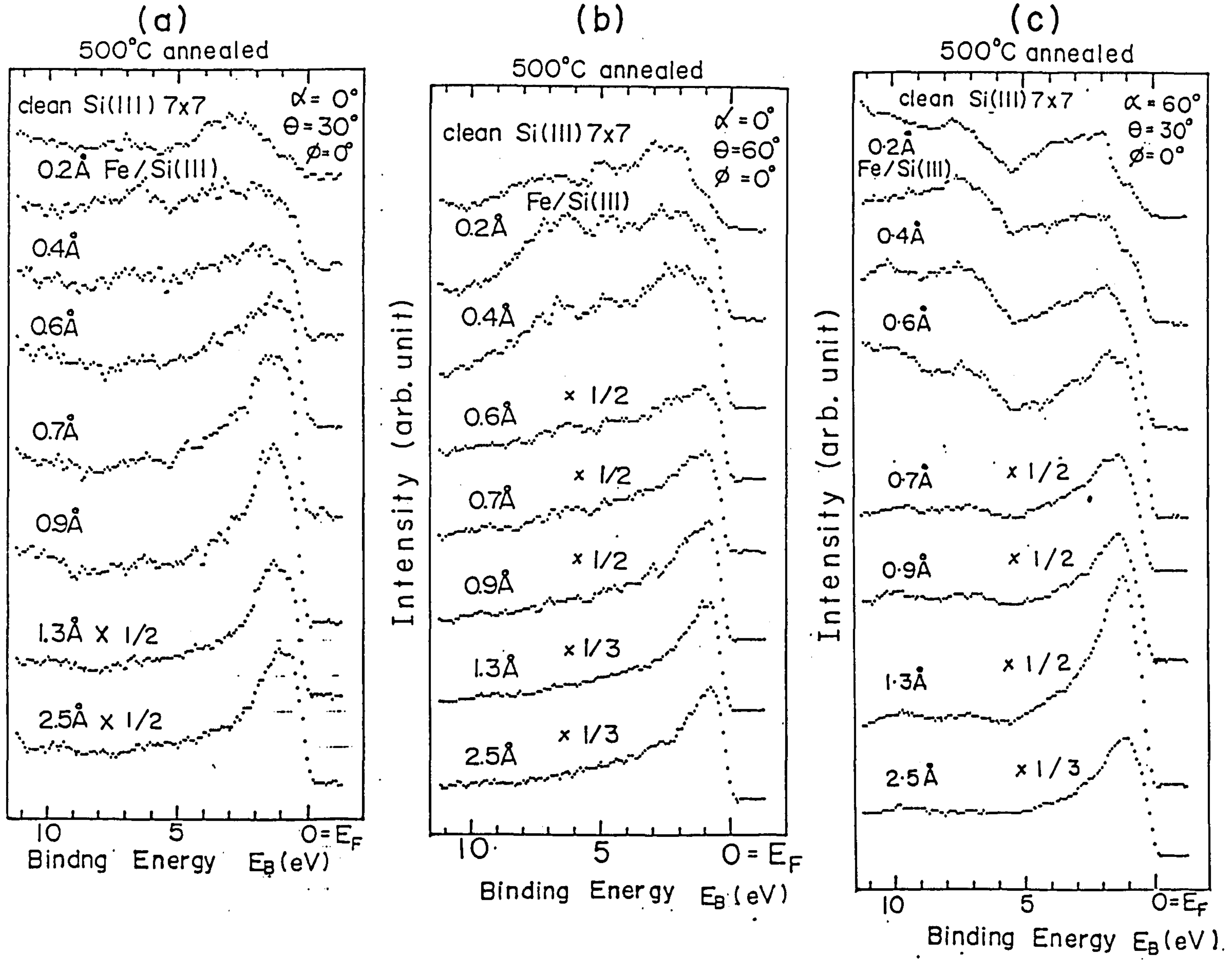

Fig.19 ARUPS spectra measured for the films of various average thicknesses which have been annealed at high temperature (500°C). Experimental geometries are the same as those in Fig.18.

3-2. Ultra-thin iron films on MgO(001) surface

3-2-1. Relation between Auger peak height and film thickness

The changing rates of the normalized Auger peak heights of Mg-LVV(26eV), O-KLL(501eV), Fe-MVV(42eV) and Fe-LMV(648eV) during iron film formation on MgO(001) surface at room temperature are shown in Fig.20. The sample was prepared by the following method. In air, the MgO crystal (Daiichi Kigenso Kagaku Co., Osaka) was cleaved to a size of 5mm x 5mm x 1mm and was mounted on a sample holder made

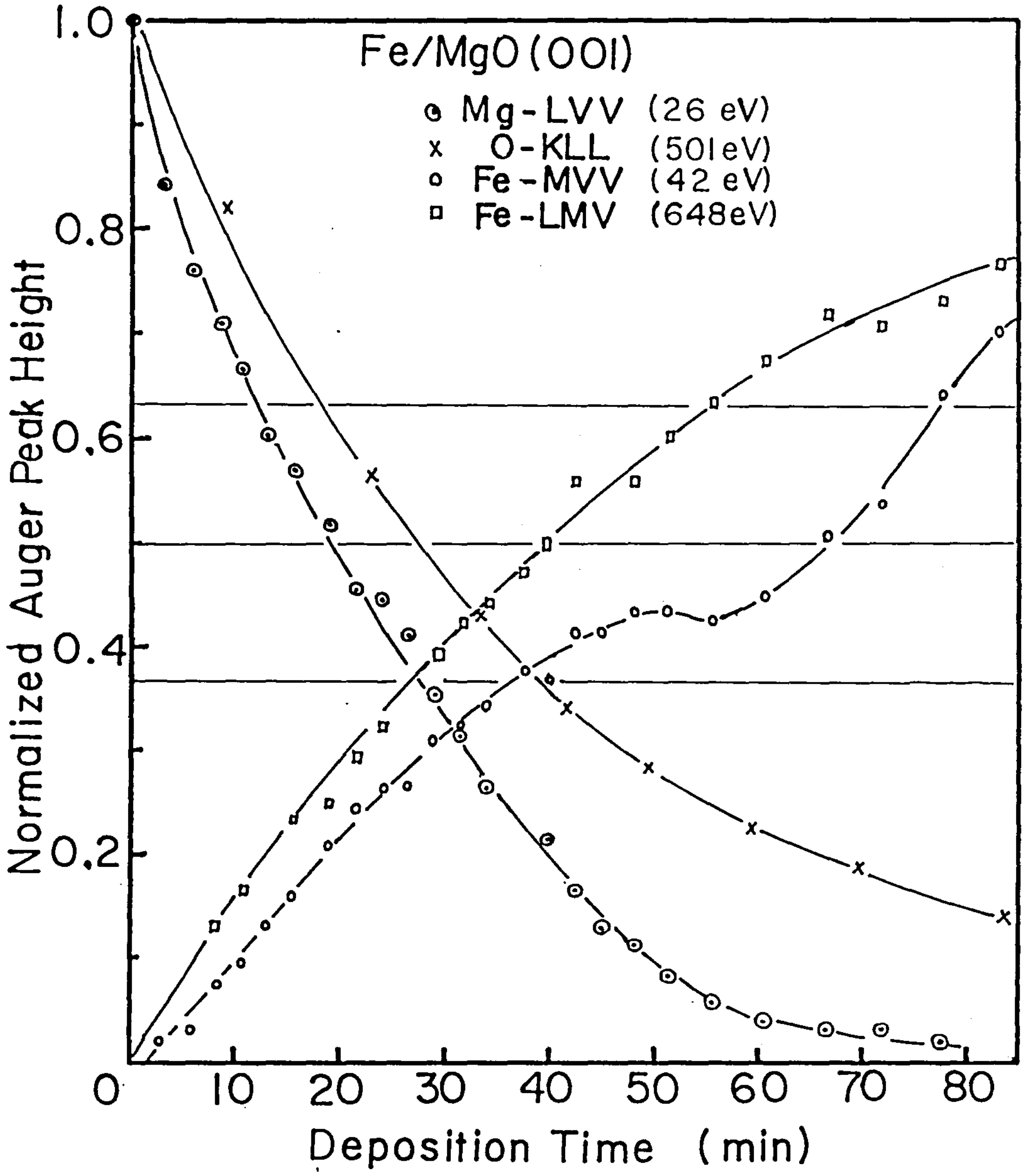

Fig.20 Normalized Auger amplitudes vs time of deposition for iron film on MgO(001) surface at room temperature. Deposition rate is about 0.2 Å/min. Since four curves separate with one another, according to the Palmberg's criterion, it is indicated that the iron film dominantly has grown in layer-by-layer growth mode.

of tantalum foil. After a conventional UHV evacuation process, a remarkable Auger signal corresponding to carbon was usually detected. Therefore, the specimen was heated up to 800°C in oxygen atmosphere at a pressure of 1.3×10^{-3}Pa until the carbon signal disappeared27). The purities of the MgO crystals used were not confirmed, but for another piece of the crystal provided from the same manufacturer, the principal impurities were Al_2O_3 50ppm, CaO 30ppm and Fe_2O_3 20ppm.

In Fig.20, four curves separate with one another in accordance with individual energy (i.e. escape length). Consequently, from the Palmberg's criterion mentioned in Appendix D iron film grew layer-by-layer on MgO(001) surface. However, inspite of repetitions of corresponding measurements several times, distinct break point could not be observed and therefore, it is difficult to apply the Jackson's criterion. From the value of deposition rate in this experiment (0.2 Å/min), individual escape length can be calculated. If these values are put on the curves in Fig.45, they are reasonable except Fe-MVV Auger peak. Fe-MVV Auger peak indicates an unusual behavior, namely, (i) increasing rate of normalized peak height is considerably slow, (ii) once at about 55min. (about 11 Å) increasing rate has halted. The suspected cause of this behavior should be discussed in section 5-2.

3-2-2. LEED I-V curves of clean MgO(001) surfaces

A few investigations for MgO(001) surfaces have been carried out by LEED. Legg et al.28) measured I-V curves for a vacuum cleaved MgO(001) surface and one of the authors, Kinniburgh, compared the experimental results with the theoretical curves obtained by dynamical calculations29,30). He concluded that relaxation of the surface top layer was very small, at most less than 3%. Berndt measured I-V curves for an air-cleaved MgO(001) surface down to the lower energy region[31].

On the other hand, Welton-Cook and Prutton indicated by a shell model calculation of the surface energy that the MgO(001) surface should not be relaxed but might be rumpled to a degree of 5%[32]. Experimentally, Murata et al. noticed the change of the MgO(001) surface from normal to rumpled structure after annealing at temperatures higher than 300°C in UHV[33,34]. Their ascertainment depends mainly on the analysis of Kikuchi pattern in reflected high energy electron diffraction (RHEED)[34,35]. Recently, Welton-Cook and Berndt identified a finite rumple of 2% by an R-factor analysis of LEED I-V curves for an air-cleaved surface[36].

Hence, how the experimental conditions of heat treatments affect the I-V curves was investigated. Measurements of I-V curves were carried out at room temperature in UHV (about 2×10^{-8}Pa) for three different MgO(001) surfaces. Surface I was prepared by the following method. In air, the MgO crystal was cleaved to a size of 5mm x 5mm x 3mm and was ditched along the (001) plane. This crystal was mounted on a special sample manipulator. Just before the measurement, the wedge was thrust into the ditch to cleave the crystal and this freshly exposed surface (surface I) was studied first. Then the crystal was heated at 300°C in 30min., and the surface after heating (surface II) was studied. The temperature was measured by a thermocouple which touched the sample holder. The pressure during the heating increased to about 2×10^{-7}Pa. Surface III was cleaved in air, and after a conventional UHV evacuation process it was heated up to 800°C in oxygen atmosphere of 10^{-3}Pa to remove carbon contamination.

The incident angle of the primary electron beam was selected to be perpendicular to the surface. To confirm this condition, at first, the I-V curves corresponding to the four symmetrical {10} beams were compared. An example of the four curves for surface III is given in Fig.21. Although the four curves are not precisely similar to each other because the uniformities of the fluorescent screen and the mesh grids are also not complete, the similarity of the four curves is considered to be sufficient for the following analysis.

All the three curves in Fig.22 are the experimental I-V curves of the (10) beam which were obtained in the studies of surfaces I, II and III. It is important that the three experimental curves seem to be very similar to each other. The low energy ends of these curves in Fig.22 are limited by the charging up phenomena. In Fig.23(a) and (b) the experimental curves of the (11) beam and (20) beam for the three different surfaces are indicated, respectively. It is shown again that three different surfaces give similar I-V curves. The low energy ends of the (11) and (20) curves are limited by the geometrical relation of which the diffraction spots arrive at the outer edge of the screen.

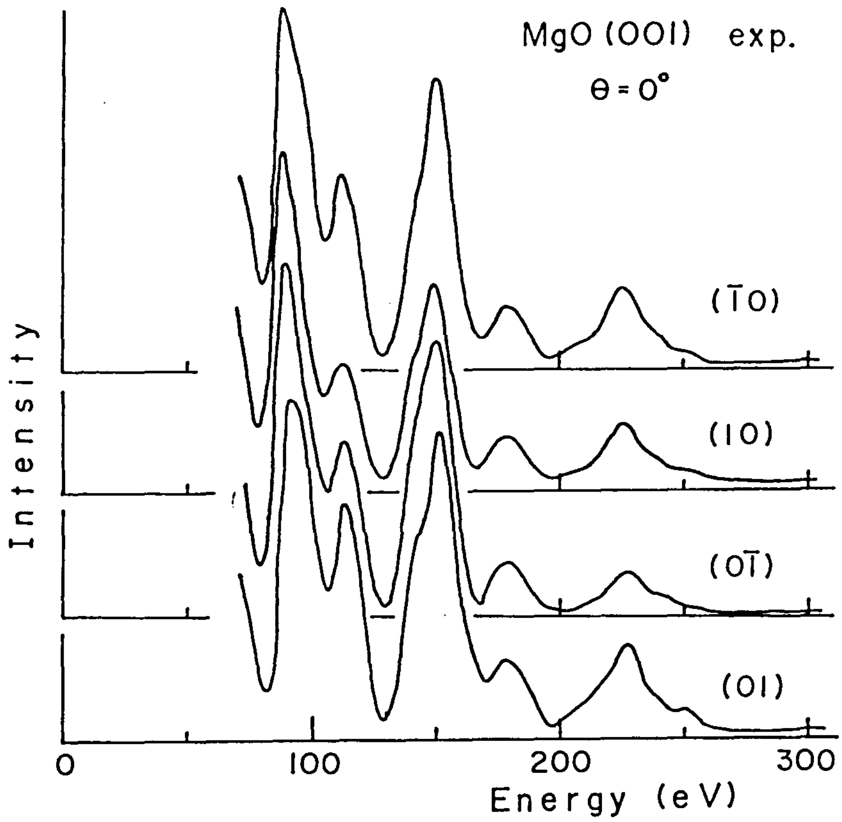

Fig.21 Four symmetrical I-V curves of 10 beam for the Mgo(001) surface III (air-cleaved and eliminated carbon contamination by heating up to 800°C in oxygen atmosphere of 10^{-3} Pa) for the confirmation of the condition of normal incidence. Although the four curves are not precisely similar, the similarity is considered to be sufficient for the present purpose.

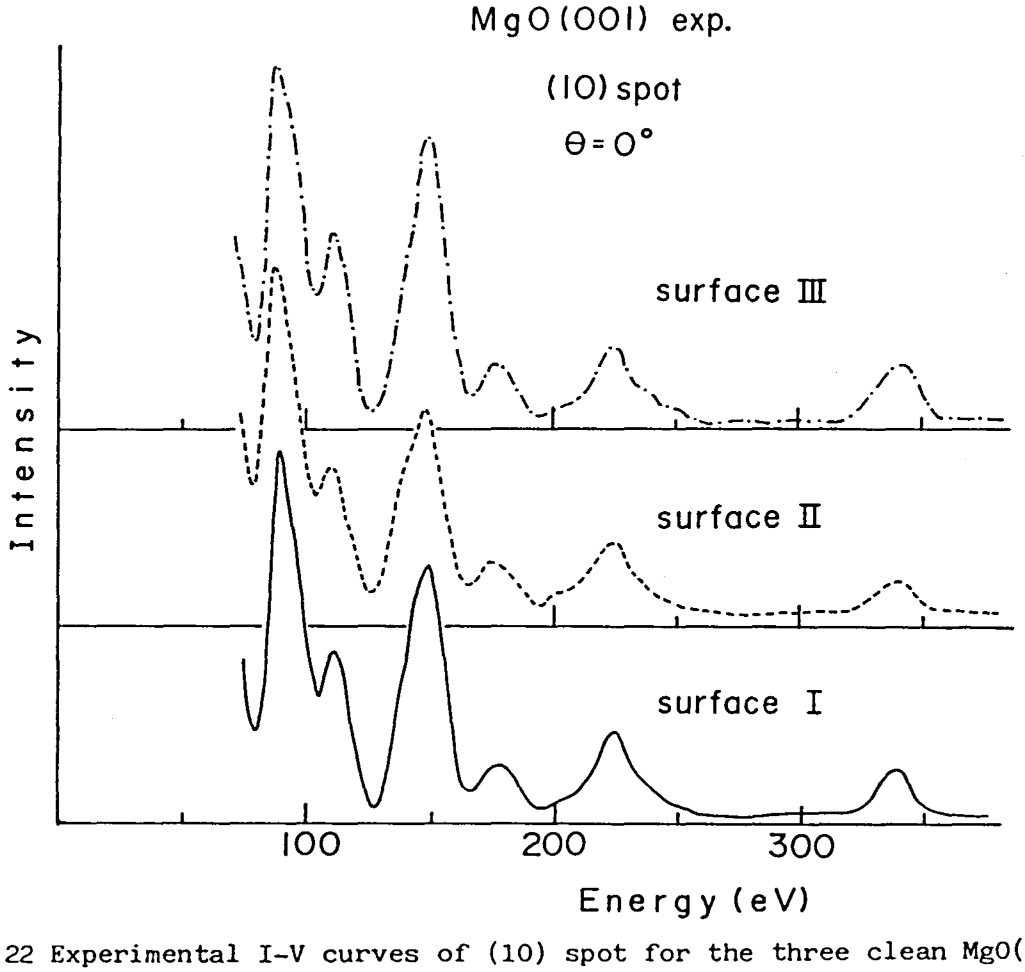

Fig.22 Experimental I-V curves of (10) spot for the three clean MgO(001) surfaces. Surface I is the vacuum-cleaved surface, surface II is the surface which has been heated up to 300°C after vacuum-cleavage, and surface III is the air-cleaved surface.

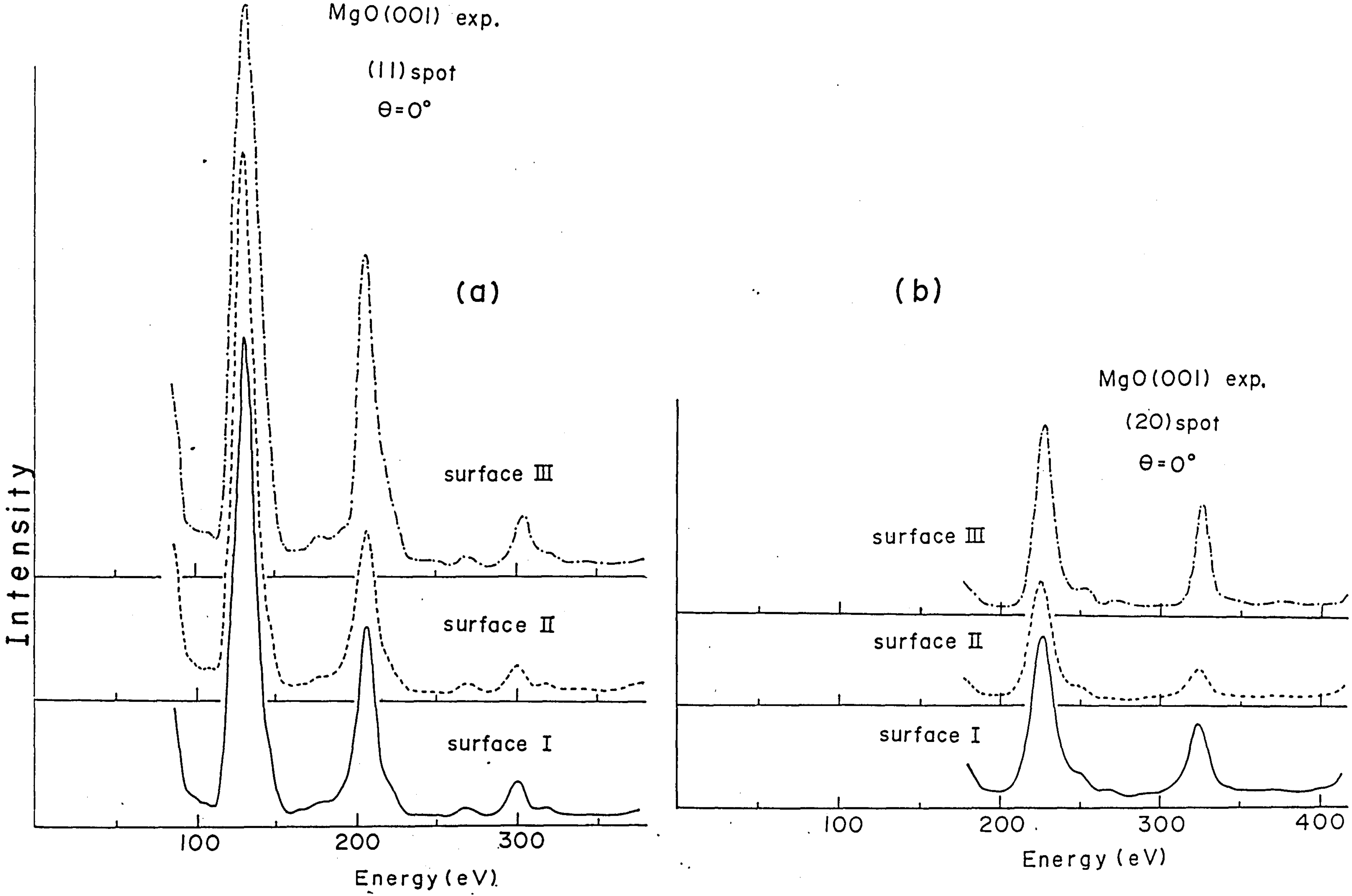

Fig.23 Experimental I-V curves of (a) (11) spot and (b) (20) spot for three clean MgO(001) surfaces. Three surfaces show similar I-V curves.

3-2-3. LEED I-V curves of iron films

During the formation of the iron film on MgO(001) surface at room temperature, 1x1 LEED pattern was observed for all films of various average thicknesses, and finally, the bulk-like Fe(001) surface has appeared. In order to study a change of the surface structure more precisely, LEED I-V curves for (00) and (11) beams were measured under the condition of incident angle $\theta=6^\circ$ at the stage of various film thicknesses. Typical LEED patterns for various film thicknesses are shown in Fig.24 and I-V curves are shown in Fig.25(a) and (b). The low energy ends of these curves are unobservable by the charging up phenomena. From these curves, the following results are considered:

(i) Because only 1x1 LEED pattern was observed, it seems that an iron film is pseudomorphic at early stages. For the film of 2Å average thickness (about 1ML) most of peaks corresponding to both (00) and (11) beams has shifted slightly to higher energy side. It is likely that these shifts represent a decrease of lattice spacing of topmost two planes.

(ii) Because the peak position did not change up to 7Å thickness (about 4ML), it seems that a pseudomorphic structure exists for this film thickness. Since the spot intensity decreased and the back ground intensity increased, however, a crystalinity becomes imperfect.

(iii) At about 10Å another structure (probably bulk-like bcc iron film) began to grow. For this specimen, unusual behavior of Fe-MVV Auger peak has been observed as was described in section 3-2-1.

These curves are discussed again by comparison with theoretical I-V curves in section 4-3.

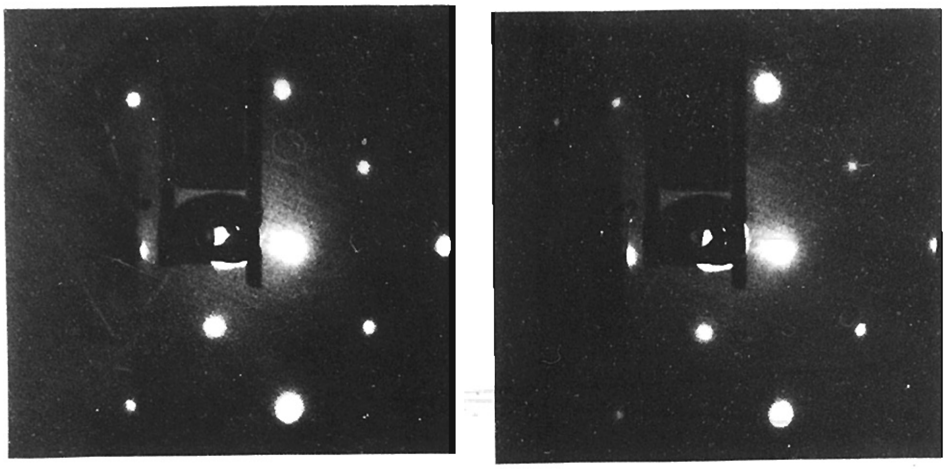

clean MgO (001) 138V   1Å Fe/MgO 135V

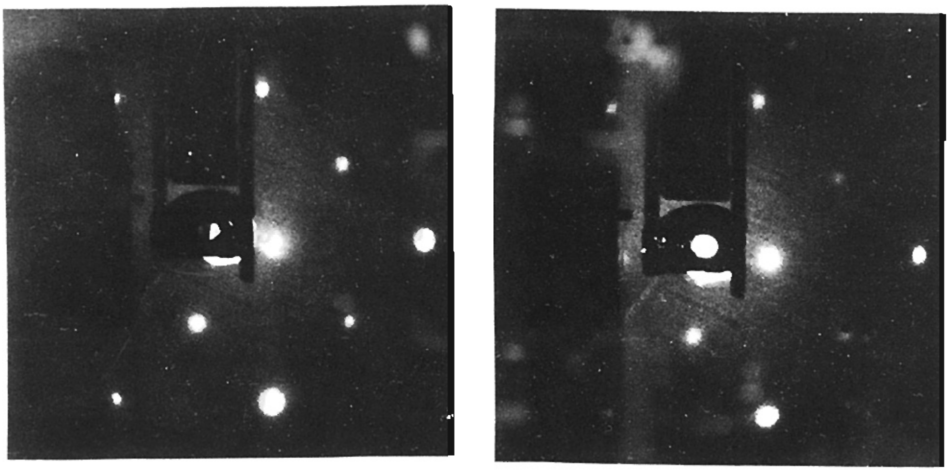

2Å 142V   6Å 142V

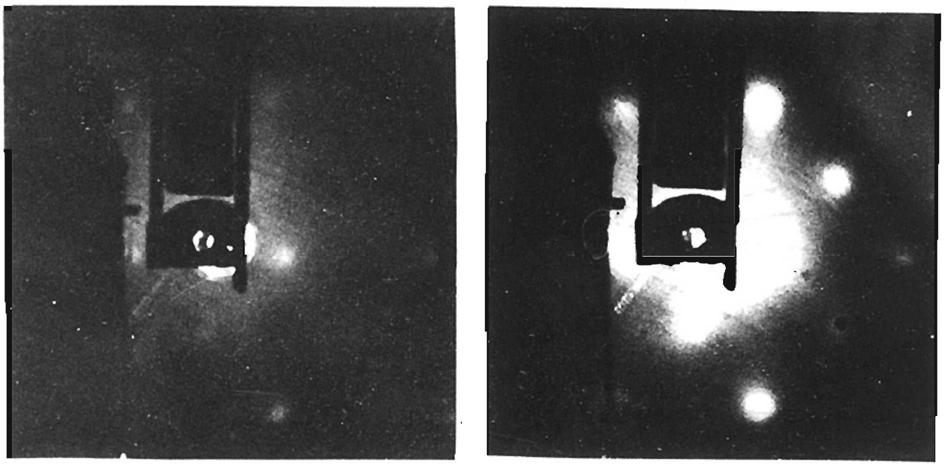

11Å 142V   23Å 180V

Fig.24 Typical LEED patterns of iron films of various thicknesses on MgO(001) surface.

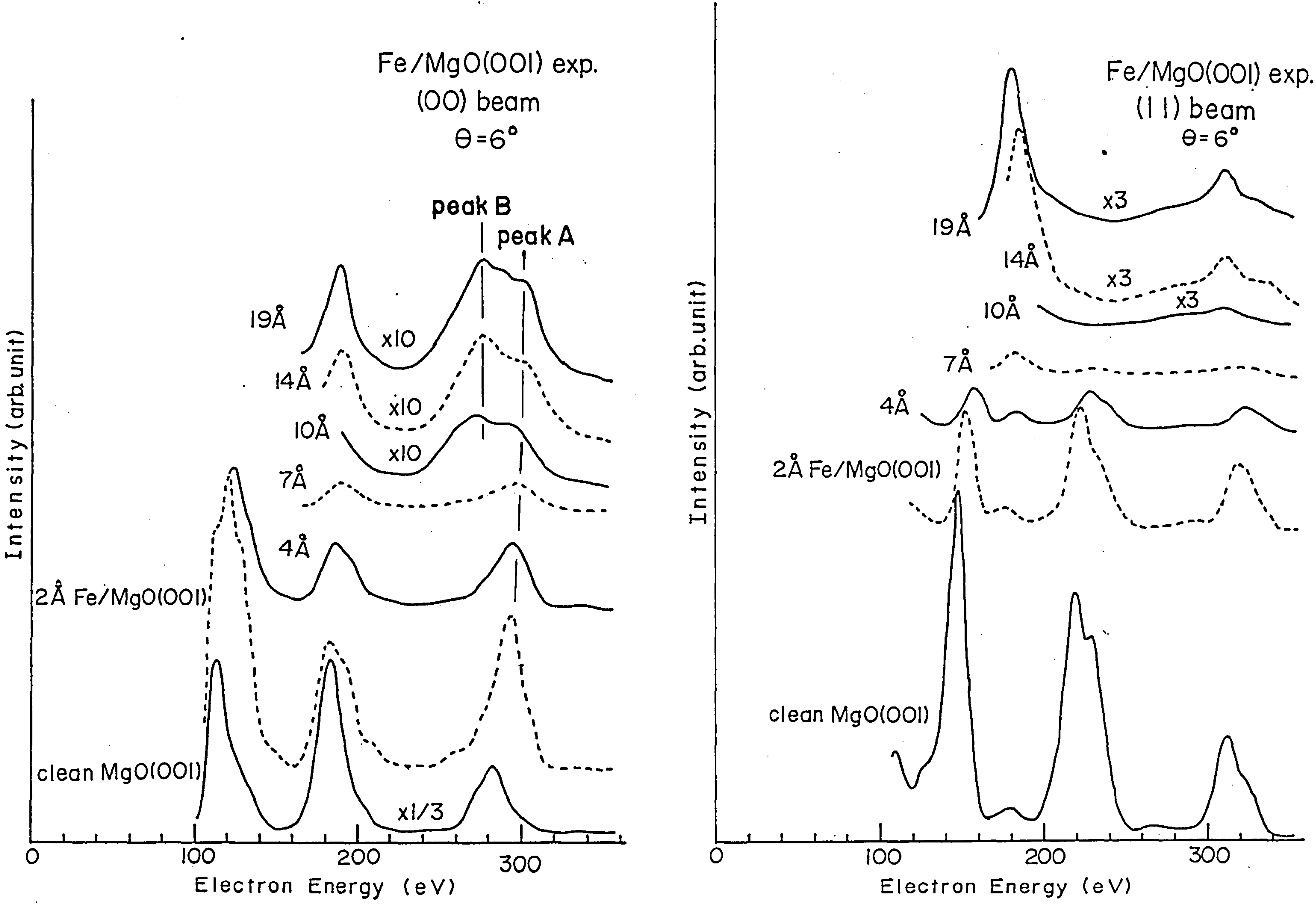

Fig.25 Experimental I-V curves of (00) and (11) beams for iron films of various thicknesses on MgO(001) surface. The low energy ends are unobservable by the charging up phenomena.

§4. Atomic structure analysis by comparison between experimental I-V curves and those of dynamical calculations

LEED is the most fundamental and the most frequently used technique for surface crystallography. In order to determine relative atomic positions, however, it is necessary to measure the spot intensity versus electron energy curves (I-V curves) and to compare those with the theoretical ones based on dynamical calculations. Many studies on the LEED theory, in which the multiple scattering process is considered, have been carried out. Pendry has published comprehensive studies on theories and a set of computer programs2), and Van Hove and Tong have added a few theoretical treatments and reformed a set of computer programs for the more extensive use3).

A general process of dynamical calculations is as follows: First, a set of phase shifts of species, δ_ℓ , which characterizes a scattering amplitude of an ion-core is calculated based on the "muffin-tin approximation". Second, a crystal is decomposed into piled up planes which are parallel to the surface and has an equivalent area of the two-dimensional unit cell, and a scattering amplidude by this single plane is calculated by taking an effect of multiple scattering exactly into account. Third, the diffracted beam intensities are calculated by considering an effect of multiple scattering among those parallel planes by an exact method or perturbation method. These processes are surveyed in Appendix F.

4-1. Clean MgO(001) surface

Several calculations have been carried out based on the theory and the computer program by Pendry.

The core state wave functions tabulated by Herman and Skillman[37)] were used to calculate the phase shifts. It is assumed that the MgO crystal is fully ionic, i.e., that the charge on the Mg and O ions are +2e and -2e, respectively, and that the Madelung potential is uniform within a muffin-tin sphere. The core state wave functions outside the muffin-tin spheres are neglected. Therefore, strictly speaking, the charge neutrality condition does not hold. The radii of the muffin-tin sphere for Mg and O ions have been asuumed to be 0.65 and 1.46 Å, respectively[38)]. Calculated phase shifts are indicated by solid curves in Fig.26.

Satoko et al.[39)] has mentioned that the charge of the Mg ions at the surface is +1.54e, which is smaller than +1.82e in the bulk, by the cluster calculations based on the DV-Xα method. Kinniburgh[29)] has calculated I-V curves for the clean MgO(001) surface with 6 kinds of phase shifts. These are for two cases of charges of atoms (both are neutral and with $Mg^{2+}O^{2-}$ charge), and for three cases of muffin-tin radii ($r_{Mg}=r_O$, $r_{Mg}=0.414r_O$ and $r_O=0.414r_{Mg}$).

Therefore, in order to confirm the effects of the charge and the muffin-tin radii, the phase shifts have been calculated for the cases of equal muffin-tin radii, $r_{Mg}=r_O$, with $Mg^{2+}O^{2-}$ and $Mg^{1.5+}O^{1.5-}$ charge and of the mentioned radii, $r_{Mg}=0.45r_O$, with $Mg^{1.5+}O^{1.5-}$ charge. As Kinniburgh has pointed out[29)], however, there is no important difference from those indicated by solid curves in Fig.26. There was a rather large difference whether the exchange potential was included (Hartree-Fock approximation) or not (Hartree approximation).

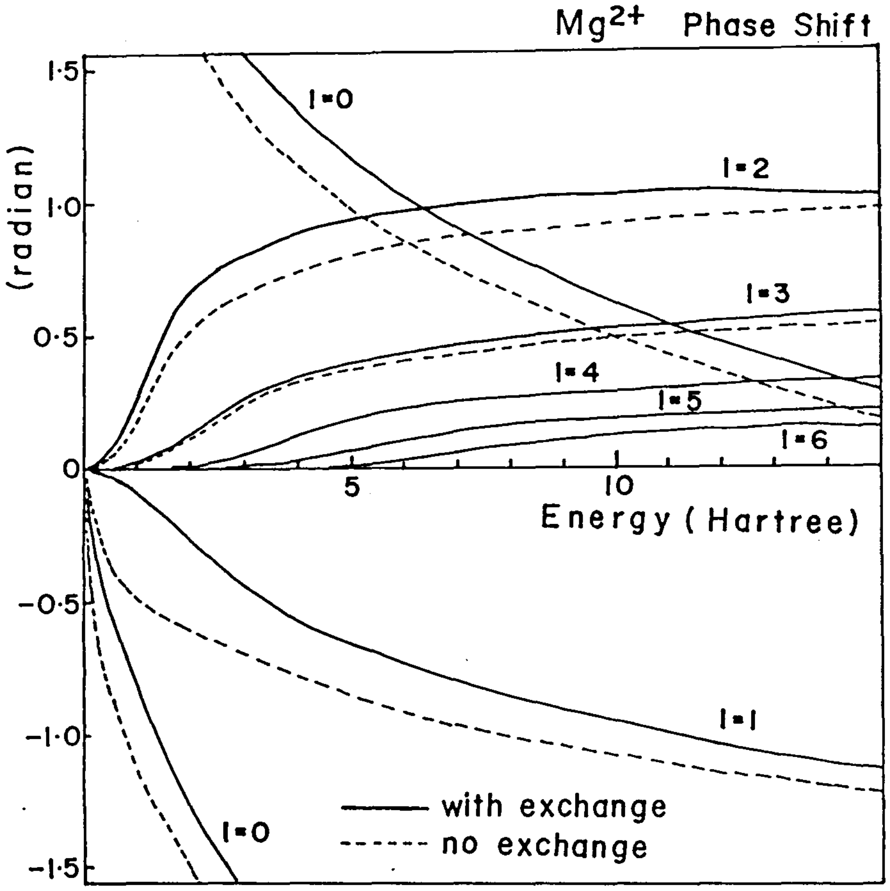

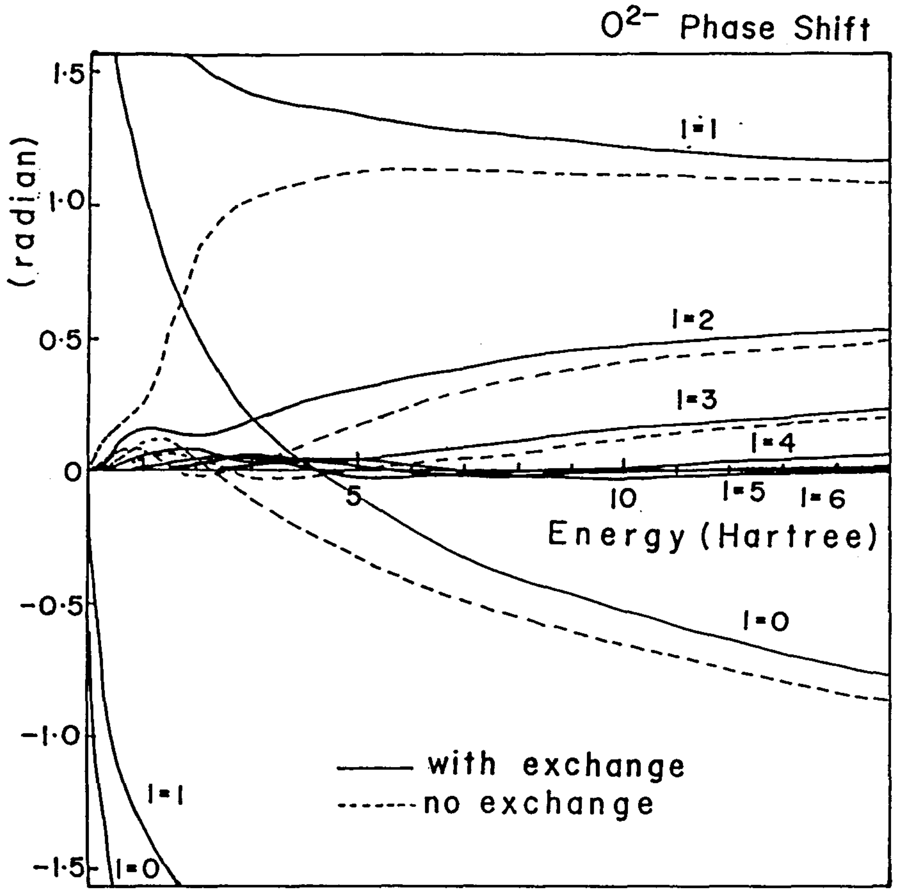

Fig.26 Calculated phase shifts for (a) Mg^{2+} and (b) O^{2-}; ——— Hatree-Fock approximation, - - - -Hartree approximation. The muffin-tin radii for Mg and O ions are 0.65 and 1.46 Å, respectively.

The results with Hartree approximation are also indicated in Fig.26 by broken curves.

For criterion of the electron beam decay in a crystal, the imaginary part of the inner potential, $V_{0i}(E)$, has to be estimated. First, the values of $V_{0i}(E_j)$ at several energies, E_j, were calculated from the experimental data on the electron escape length, $l(E_j)$$^{40)}$, which is usually considered that the dependence on material is small (Fig.45). That is, the value of wave vector for an electron in a crystal is presented by

$$k = \sqrt{2(E+V_{0r}) - 2iV_{0i}} \quad \text{(atomic unit)},$$

where V_{0r} is the real part of the inner potential, and if k is replaced by A+iB, the value $V_{0i} = -B\sqrt{B^2 + 2(E+V_{0r})}$ (<0) is derived. On the other hand, if the wave functions of electrons which propagate within a crystal is indicated by a plane wave $\exp(ikr)=\exp(iAr-Br)$, intensity decays with a distance as $\exp(-2Br)=\exp(-r/l(E))$.

Next, the values of $V_{0i}(E)$ was approximated by a hyperbolic curve in order to fit best to each $V_{0i}(E_j)$ as follows,

$$V_{0i}(E) = 180.0/E - 6.1 \text{ eV} \qquad (E \gtrsim 35.3\text{eV})$$

$$V_{0i}(E) = -1 \text{ eV} \qquad (E \lesssim 35.3\text{eV}) \; .$$

Although in very low energy region absolute value of V_{0i} is slightly larger than those used by other researchers, in the energy region of this study, two values are similar to each other.

The energy interval, ΔE, at every energy diffracted intensity is calculated, was chosen smaller than the absolute value of V_{0i}. At E=100eV, ΔE is 3.4eV. For increasing the energy value, ΔE increases, and beyond E=200eV, constant intervals of 5.4eV are used.

To calculate the diffracted beam intensities, the computer program by Pendry$^{2)}$ to estimate a diffraction matrix element of sigle layer, $M^{\pm}_{\vec{g}'\vec{g}}$, was partly modified to apply to the case in which plural atoms exist in a two-dimensional unit cell based on the theory indicated in Appendix F-3. The method of layer stacking is the RFS perturbation.

In order to ascertain that the curve calculated by a set of parameters has sufficient accuracy for the present purpose, several theoretical curves have been calculated for different or more improved parameters. These are shown in Appendix G-1. Finally, the following set of parameters, for convenience, has been chosen, namely, (i)the phase shifts obtained by Hartree-Fock approximation are used, (ii) 29 beams are included, (iii) 5 phase shifts are included, i.e., the

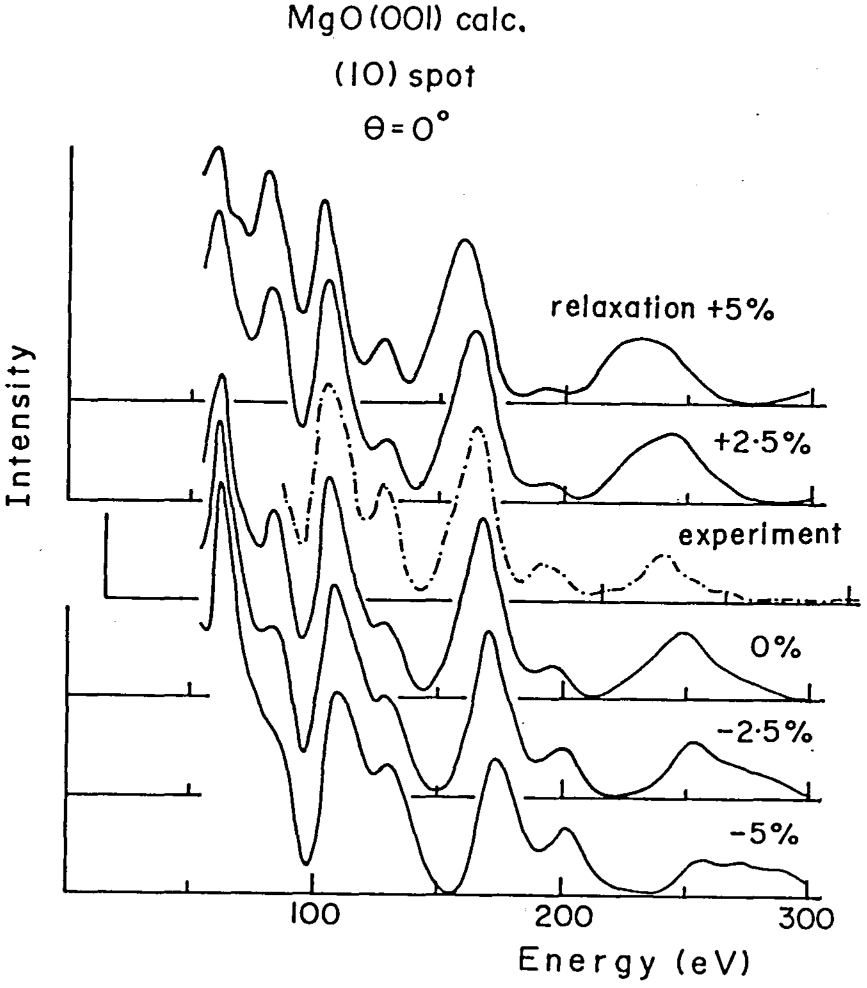

Fig.27 Calculated I-V curves of (10) spot (solid curve) for the comparison with the experimental curve (dash-dotted curve). The indices present the ratio of the relaxation to the normal lattice spacing, Δd/d, and the + and − signs represent expansion and contraction, respectively.

maximum number of the angular momentam, δ_{max}, is 4, (iv) temperature is zero (T=0K).

It has been calculated how the theoretical I-V curves are changed by the relaxation of the surface top layer. The theoretical curves for (10) spot are indicated in Fig.27 (solid curves) for the comparison with the experimental curve (dash-dotted curve). The indices in the figure represent the ratio of the relaxation to the normal lattice spacing (d=2.105Å), $\Delta d/d$, and the plus and minus signs of the value correspond to expansion and contraction, respectively. These results of the calculations show that when the spacing of the surface top layer reduces, the positions of the fundamental peak shift to the higher energy side. The amount of shift is in proportion to the peak energy, therefore, the intervals between the peaks increase.

The three experimental I-V curves for the (10) spot showm in Fig.22 are very similar to each other. This fact suggests that the three different surfaces have the same relaxation ratio. Therefore, in order to determine the relaxation ratio, following method is used. Each experimental I-V curve shown in Fig.22 has two principal peaks at the energy of 87 and 148 eV. The interval between them is 61 eV. Each theoretical curve in Fig.27 has also two large peaks near 100 and 160 eV. But the intervals in the calculation curve are correlated to the degree of the relaxation. Therefore, the calculated curve which has the same interval as that of the experimental curve is regarded as the best fit curve. From the top of the theoretical curves shown in Fig.27, the intervals of two principal peaks are 57eV, 59.5eV, 62eV, 63.5eV and 64.5eV, respectively. Then, the curves of which the relaxation ratio is zero or +2.5% are chosen. Though the energy at the two peak positions in the calculated curves are not the same as those in the experimental curves, the magnitude of this energy shift is equal to the real part of the inner potential, V_{0r}. The values of V_{0r} of the two chosen calculated curves are estimated to be about 15eV. This value seems to be reasonable. As it is shown in Fig.27, the fitting of the two chosen curves is sufficiently good with this value of V_{0r} except for a small peak at about 250eV. This small discrepancy of the peak position will be improved if more sophisticated parameters are used for the calculation (see Fig.51, curve b and c). The relative peak intensity will be in better agreement owing to the inclusion of the temperature effect.

Figs.28(a) and (b) show the results of similar examinations for (11) and (20) beams, respectively. In these figures, the experimental curves were shifted by the value of V_{0r}, 15eV, to the higher energy side. In these figures it is apparent that the peak position at about 150eV in (11) beam and that at about 240eV in (20) beam are in good agreement. A remarkable disagreement of the peak at about 230eV in (11) beam may be improved when many beams are included in the calculation (Fig.51, curve b).

Besides the relaxation, the rumpling structure should be considered. Murata et al.[33-35)] have indicated that the structure of an as-cleaved surface without rumpling changed irreversibly to a rumpled state by annealing at 300°C. In the rumpled surface, the outermost plane containing O ions locates a little (0.13Å) outside of the plane containing Mg ions. They have also pointed out that no essential difference is found between vacuum-cleaved and air-cleaved surfaces.

Okamoto and Terakura have estimated the change in LEED I-V curves induced by surface rumpling[41)]. They have calculated the I-V curves

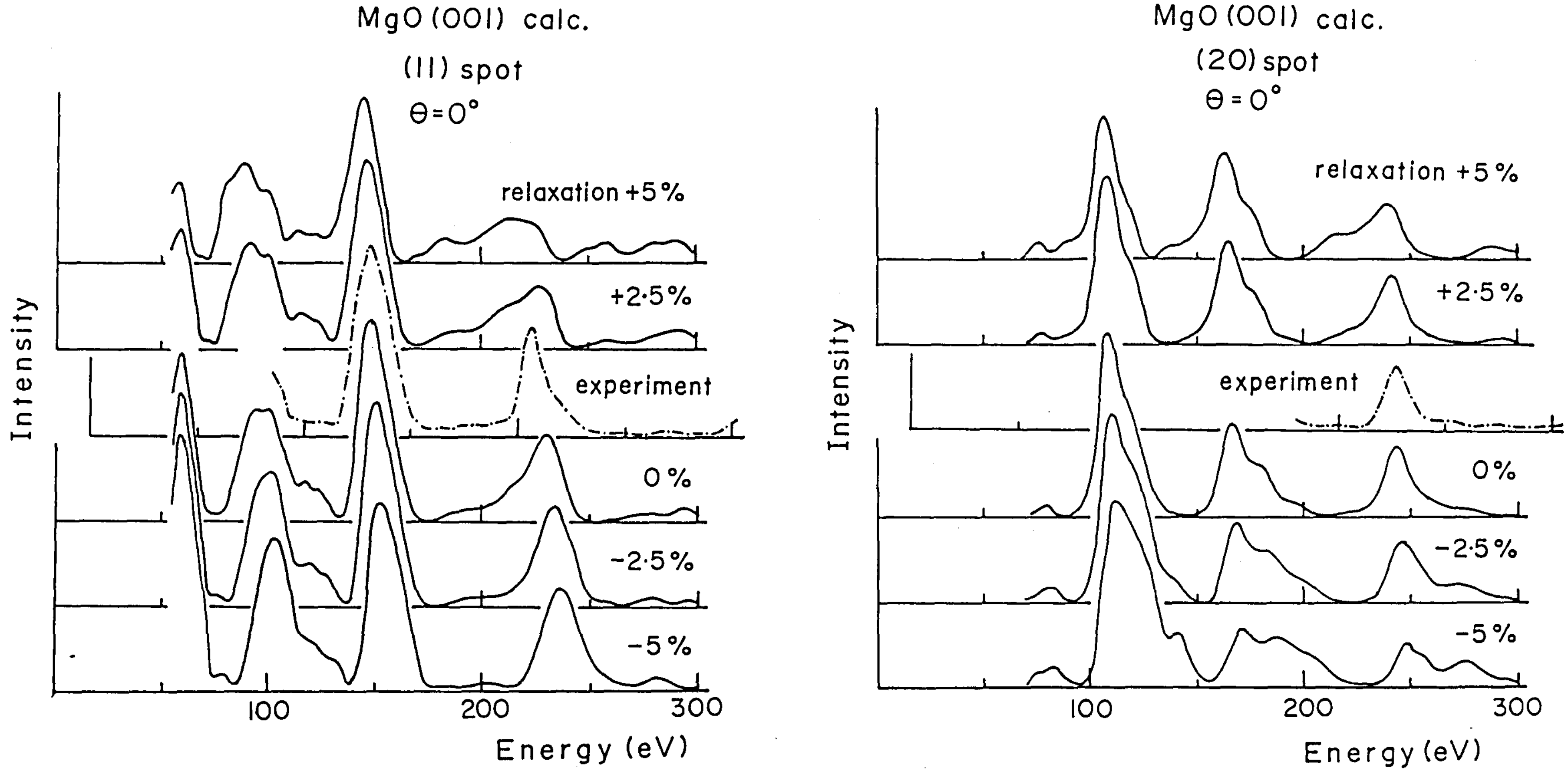

Fig.28 Calculated I-V curves of (a) (11) spot and (b) (20) spot with the deferent degree of the relaxation (solid curve) for the comparison with the experimental curve (dash-dotted curve).

for different degrees of rumpling, but without relaxation, i.e., the middle point between the O ion and Mg ion planes did not shift. As is shown in Fig.29, in the case of (11) beam as a typical example, a small peak at about 120eV between two large peaks should disappear when the rumpling parameter exceeds over about 5%. The + sign indicates that O ions are located outside of Mg ions. The small peak appeared also at 105eV in the experimental curve in Fig.23(a). Howev-

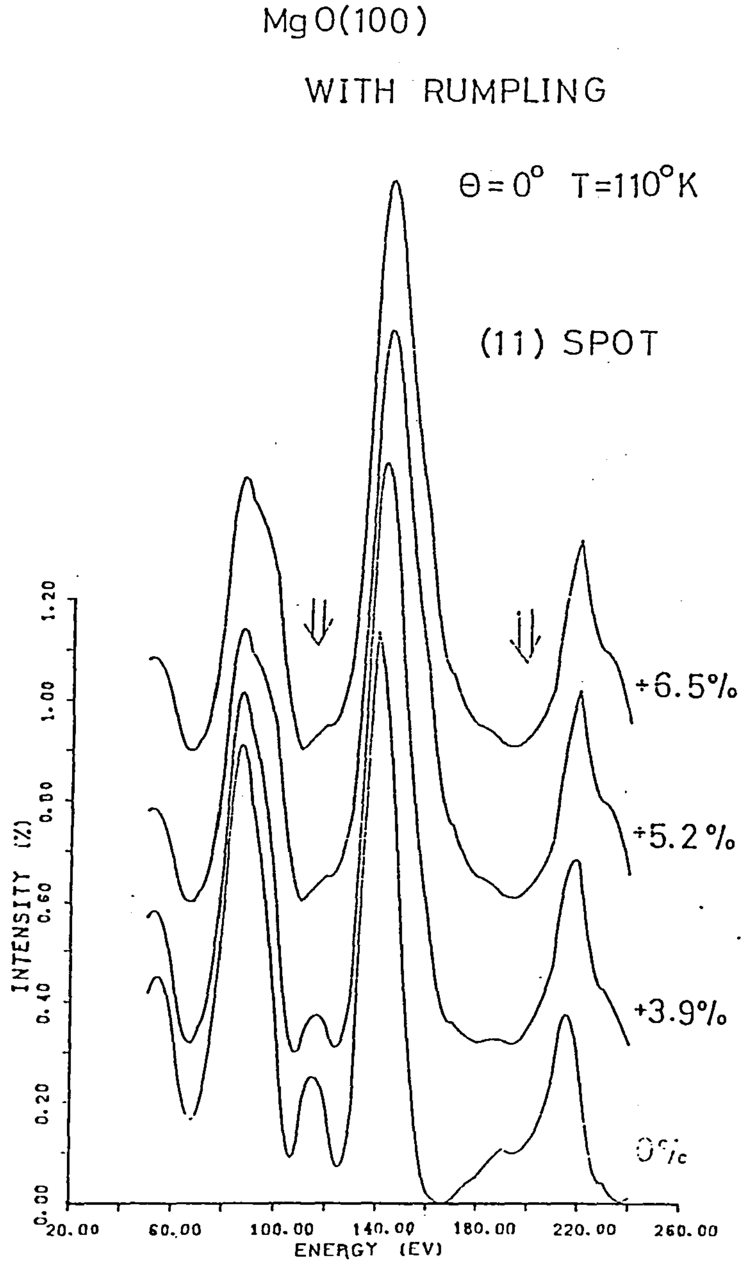

Fig.29 Calculated I-V curves of (11) spot with various degrees of the surface rumpling, by W.Okamoto (ref.41). The + sign indicates that the plane containing O ions is located outside of the plane containing Mg ions.

er, the peak is very small, and the difference among three curves can not be recognized. Therefore, from this point it seems that these three surfaces have been rumpled. On the other hand, although the slope at about 180eV in the theoretical curves in Fig.29 has an opposite gradient between a rumpled surface and a normal surface, corresponding part at about 165eV in the experimental curves in Fig.23(a) has a same gradient which is similar to that of a normal surface one another. From these considerations, the change of the degree of the surface rumpling due to heat treatments cannot be distinguished. It is difficult to determine whether it has been rumpled or not.

Recently, Causa et al. indicate that no relaxation is found and the rumpling is very small (less than 1 %) by an ab initio Hatree-Fock calculations$^{42)}$.

4-2. Ultra-thin iron films on MgO(001) surface

As mentioned in section 3-2-3, it seems that an iron film deposited on MgO(001) surface is pseudomorphic at early stages, and for the film of 2Å average thickness (about 1ML) most of peaks both of (00) and (11) beams has shifted to the higher energy side. It is likely that these shifts can be explained by a decrease of the lattice spacing between topmost two planes. In this section, first, experimental I-V curves at this stages are compared with those obtained by dynamical calculations.

To calculate the phase shifts, electron configuration of iron atom is assumed to be as 6 3d-state electrons and 2 conduction electrons. Muffin-tin radius is one-half of the nearest neighbour distance

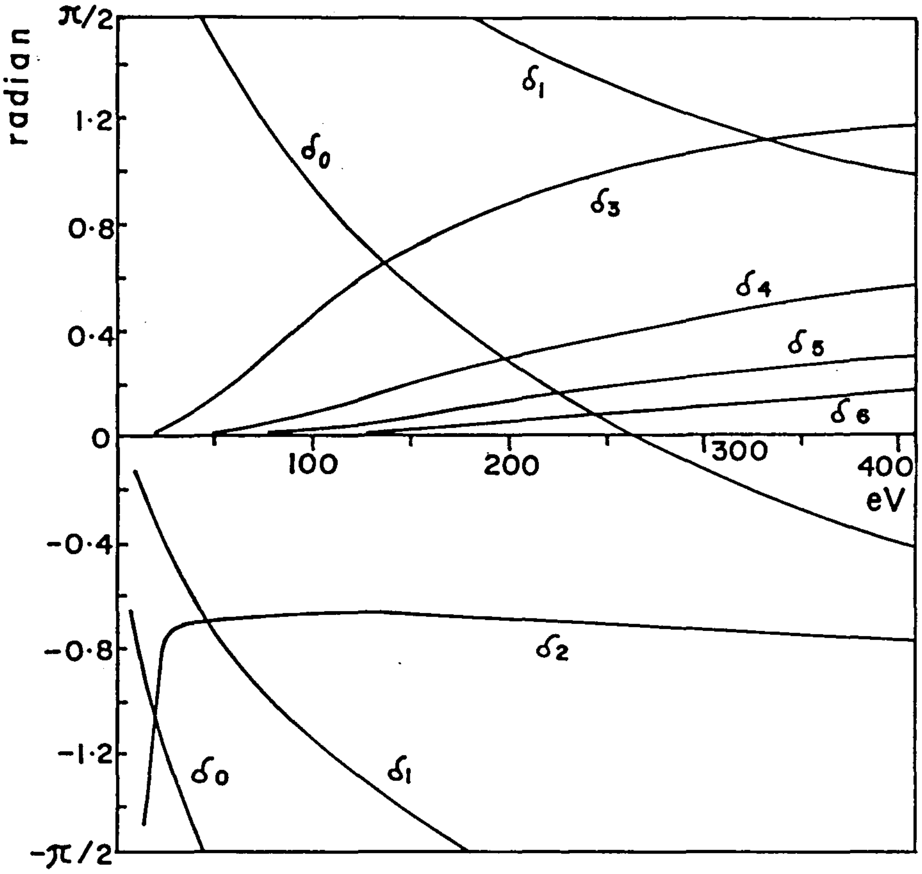

Fig.30 Calculated phase shifts for iron atom as the function of energy. Electron configulation is assumed to be as 6 3d-state electrons and 2 conduction electrons. Muffin-tin radius is 1.24 Å which corresponds to one-half of the nearest neighbour distance for bcc iron crystal.

for bcc iron crystal. Calculated phase shifts are shown in Fig.30. To calculate diffracted beam intensities, the computer program of RFS perturbation for layer stacking by Pendry was partly reformed for the sake of application to the adsorbate system.

Three adsorbed sites, that is, just above oxygen ion, bridge site between oxygen ions and just above magnesium ion, are considered. In Fig.31, calculated I-V curves of (00) beam for various spacings ($d_\perp$) between an iron layer and a topmost MgO(001) layer for three adsorbed sites are shown together with the experimental I-V curve of 2Å film thickness. The energy value of calculated I-V curves is shifted by the inner potential of V_{0r}=15eV. From these figures, a possibility that the adsorbed site locates just above the Mg ion is excluded. Though the agreement is not sufficiently excellent to conclude quantitatively, three possible positions of iron atom, just above O ion at 2.0Å height and bridge site between O ions at 2.0Å or 1.3 Å height, are expected.

Next, the experimental I-V curve of (11) beam is compared with the calculated I-V curves for the possible structures and are shown in Fig.32. From this figure, the site just above the oxygen ion at 2.0Å height is most probable. This structure seems to be plausible if we consider that iron atoms are apt to react on oxygen atom. The distance between oxygen and iron atoms is close to the corresponding values of 2.14Å in FeO crystal (NaCl type) and 2.10Å (Fe I) in Fe_3O_4 crystal (spinel)$^{43)}$. The disappearance of the fine profile which is probably based on dynamical effect in experimental I-V curves seems to be caused by the lack of crystal perfection.

Second, in order to confirm the accuracy of the calculation, the calculated I-V curve for (00) beam for bulk Fe(001) surface is

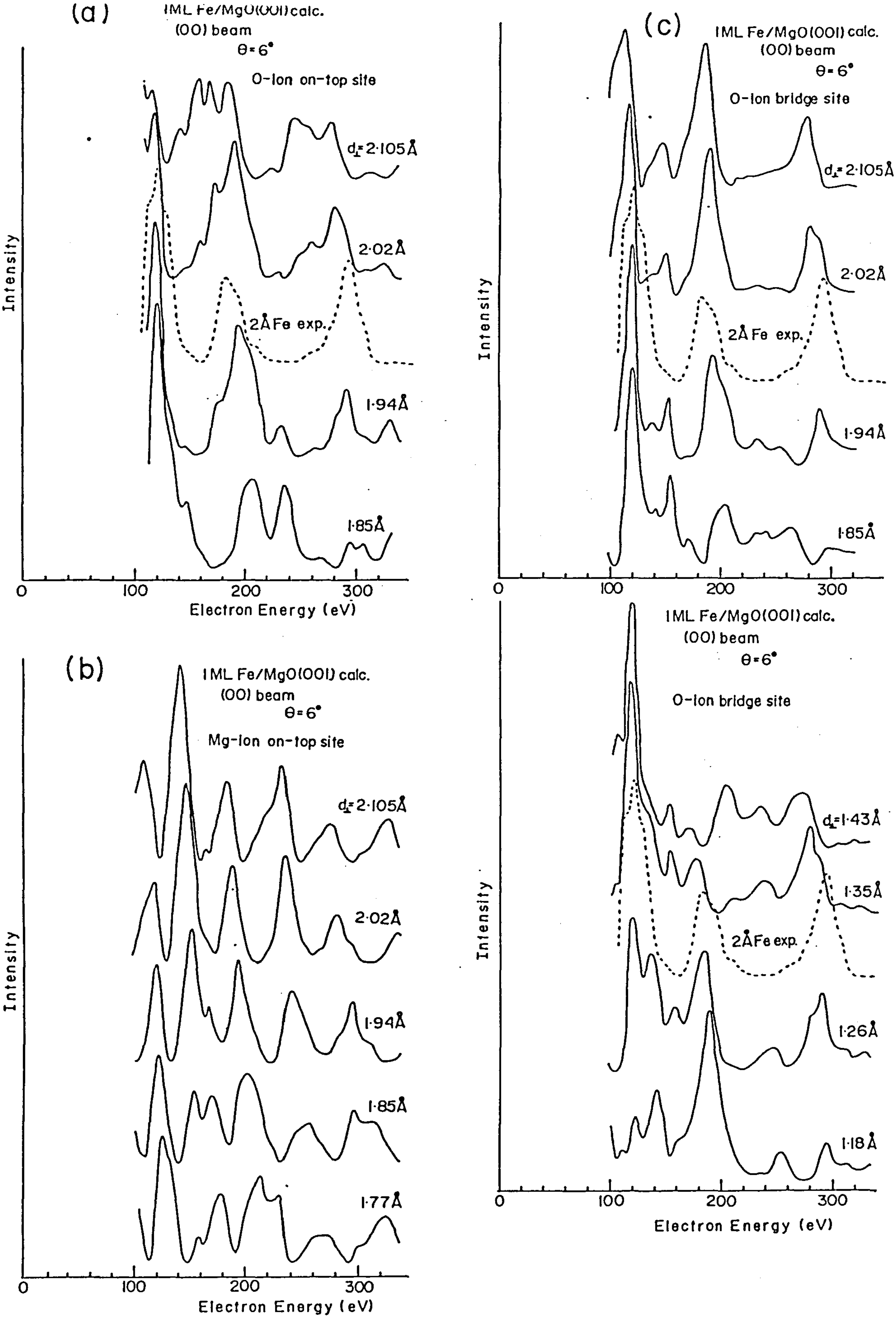

Fig.31 Calculated I-V curves of (00) beam for the monolayer pseudomorphic iron film on MgO(001) surface with the different degree of the relaxation (solid curve) for the comparison with the experimental curve of 2Å average thickness (broken curve). Three probable sit-sites of iron atoms are shown, (a) on-top site of the O ion, (b) on-top site of the Mg ion and (c) bridge site of the O ions. d⊥ represents a spacing between the iron layer and the topmost layer of MgO(001) surface.

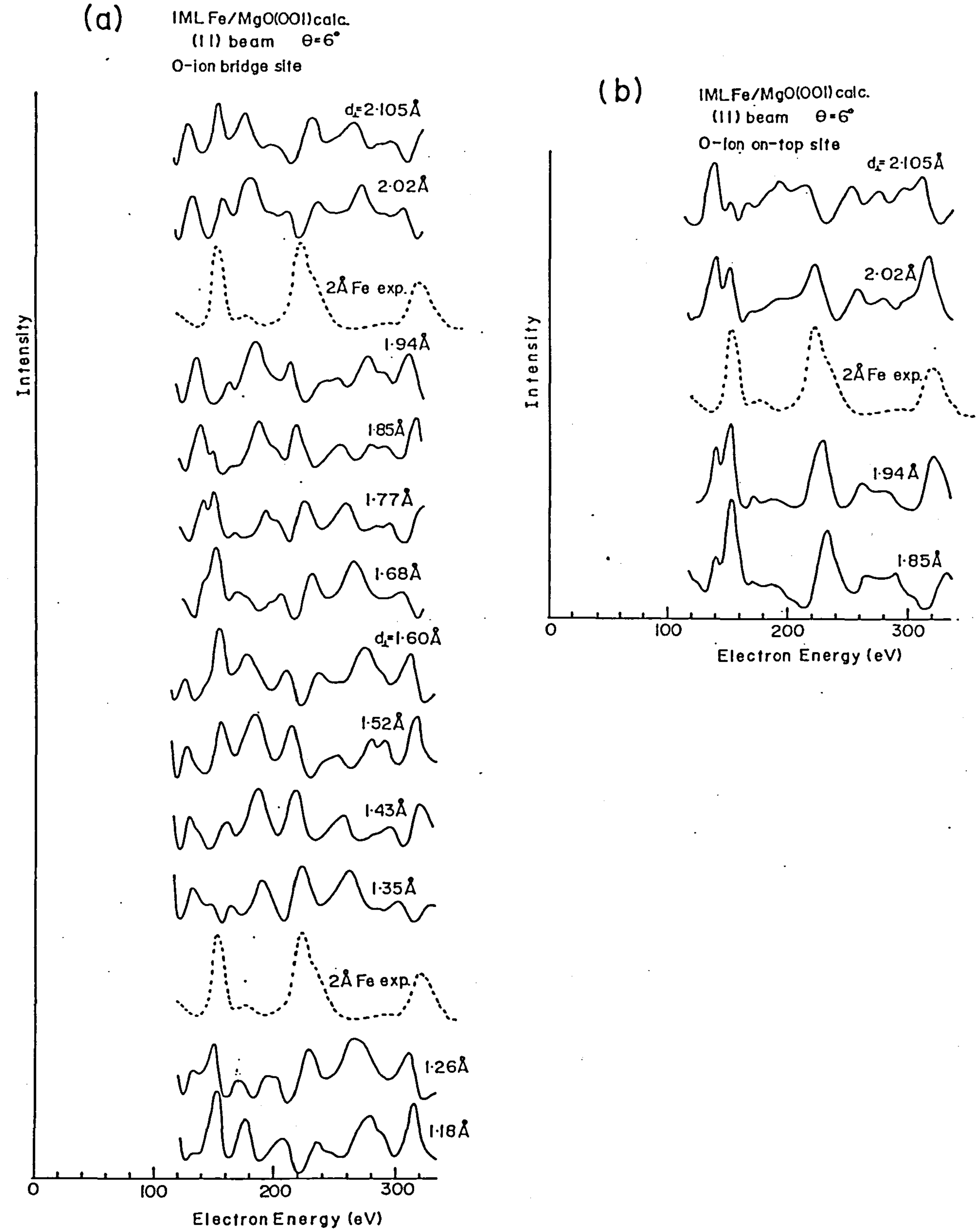

Fig.32 Calculated I-V curves of (11) beam for the monolayer iron film on MgO(001) surface (solid curve) for the comparison with the experimental curve (broken curve), (a) bridge site of the O ions and (b) on-top site of the O ion.

compared with that obtained for the clean Fe(001) surface by Nakanishi and Horiguchi[44)]. The results are shown in Fig.33. Two I-V curves are very similar with each other in respect of peak positions except an insignificant difference of the peak shape at about 100eV. Relative intesity can be improved by taking a temperature effect into consideration. This calculation takes in 5 phase shifts ($\ell_{max}=4$) and 13 beams, and lattice sum in eq.(A.15) was carried out over about 500 lattice sites. Although the layer stacking calculation was performed with

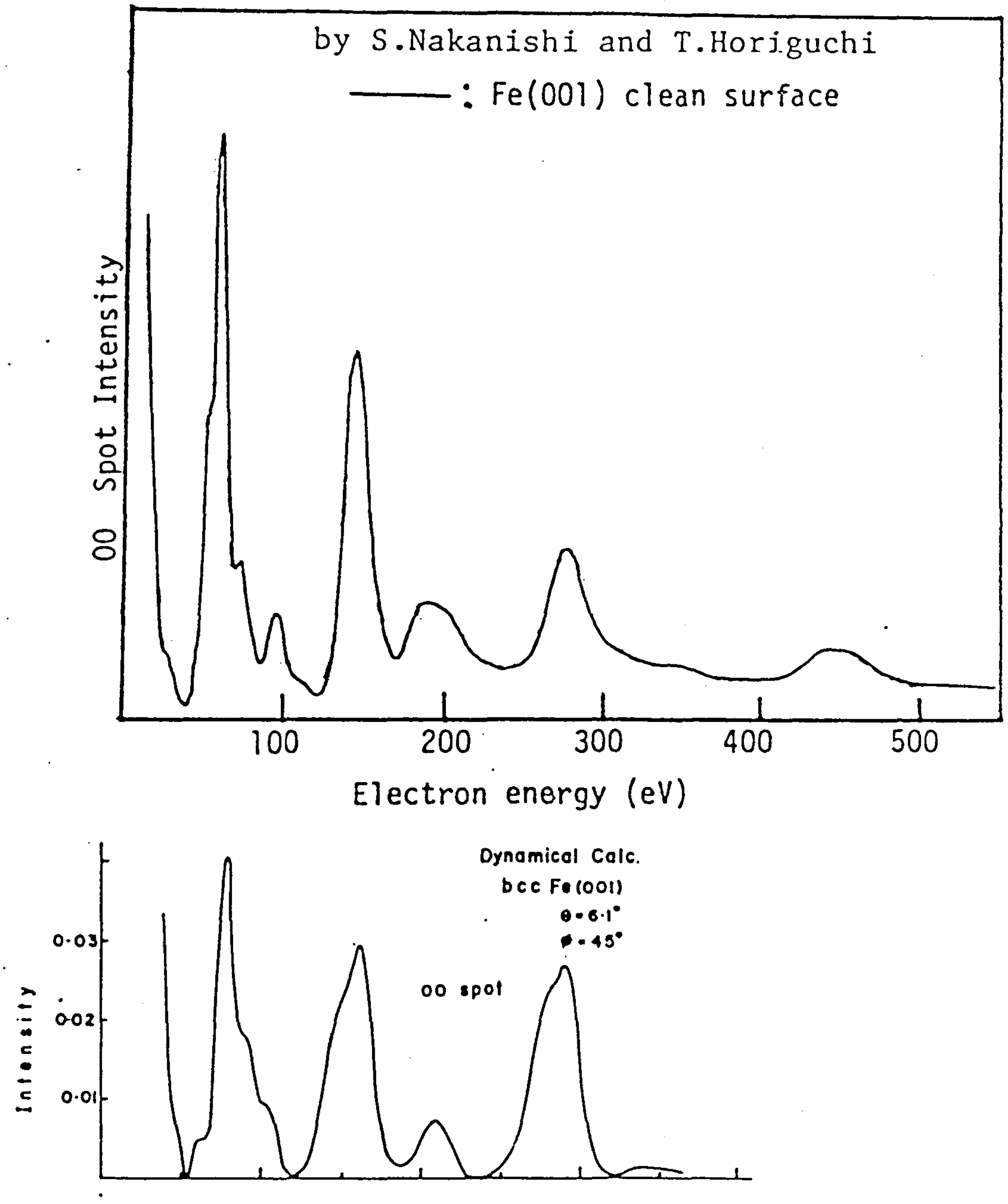

Fig.33 Experimental[43)] and calculated I-V curves of (00) beam for Fe(001) surface.

the RFS perturbation method, it is obvious that the results is sufficient in comparison with that obtained by the Layer Doubling method in Appendix G-2.

Third, experimental I-V curves of thick iron films are compared with theoretical ones. Comparing the I-V curves for (00) beam for the film with average thickness of more than 10 Å with those for the film with less than 10 Å thickness in Fig.25, it is obvious that in addition to the peak at about 295eV (peak A) a new peak appears at about 270eV (peak B) for the thick films. If the inner potential (about 15eV) is taken into account, the energy of this new peak is close to that at 290eV in the calculated I-V curves for bcc Fe(001) surface in Fig.33. Then it is considered that a growth of bcc iron film has begun at average film thickness of 10 Å.

Two-dimensional lattice constant of a square lattice for MgO(001) surface is larger by 4% than that for Fe(001) surface. Therefore, if iron film grew in pseudomorph, it is expected that the lattice within a plane parallel to the surface has spread and the lattice spacing perpendicular to the surface has shortened. Two cases are considered concerning the spacing. One is the case of which the nearest neighbour distance between iron atoms is equal to that of bulk bcc iron crystal (2.48Å), and in that case the lattice constant perpendicular to the surface should become c=2.62Å (namely, for bcc iron crystal c=2.86Å). Although I-V curves were calculated for this structure, the peak positions did not coincide.

Another is the case of which the value is estimated from the elastic constant[38)], and in that case the lattice constant perpendicular to the surface is 2.75Å. Calculated I-V curves for this body-centered tetragonal (bct) iron (001) surface are indicated in Fig.34.

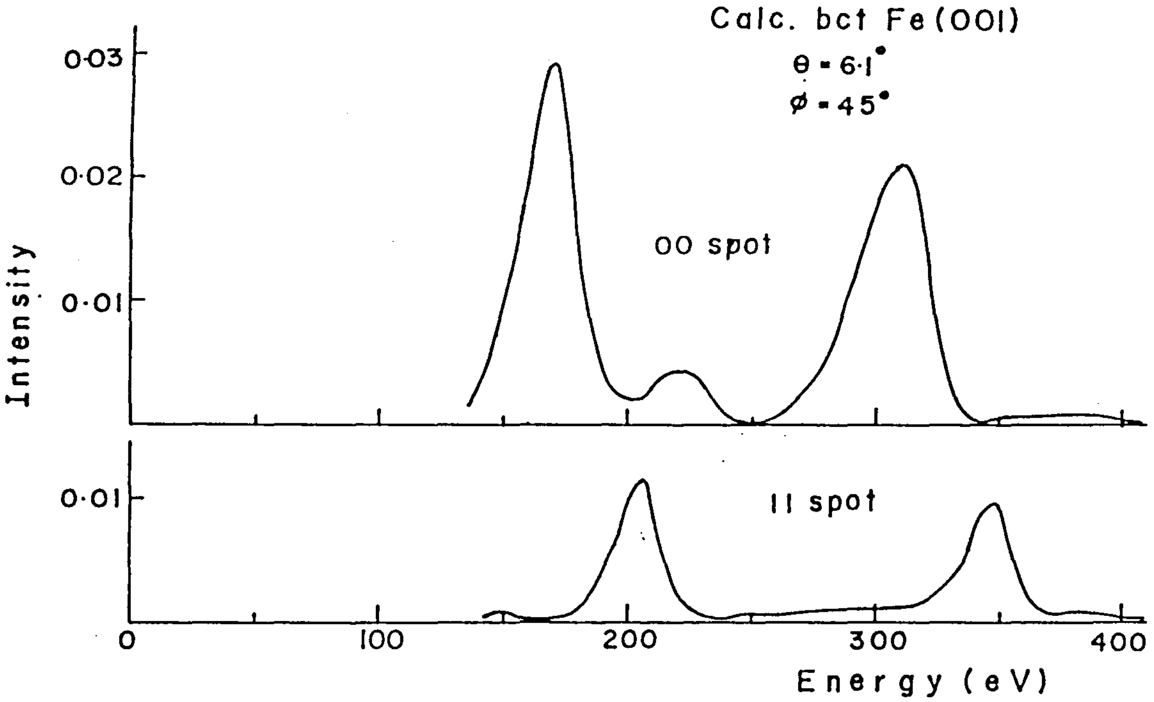

Fig.34 Calculated I-V curves of (00) and (11) beams for body-centered tetragonal Fe(001) surface.

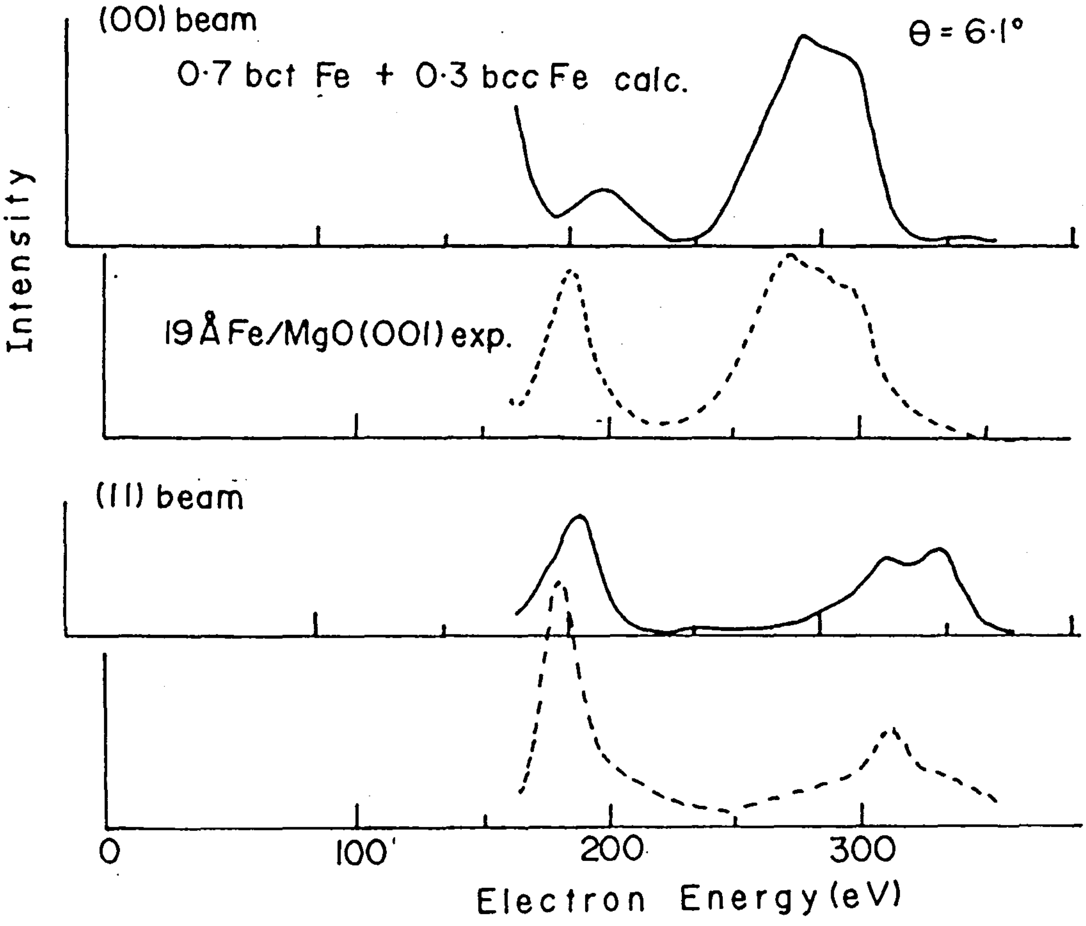

Fig.35 Calculated I-V curves added in the ratio of 0.7 bct Fe (Fig.34) to 0.3 bcc Fe (Fig.33 or Fig.52) for the comparison with the experimental I-V curves for the iron film of 19 Å thickness on MgO(001) surface shown in Fig.25.

The energy of the peak at about 310eV in the curve of (00) beam is consistent to that at 295eV (peak A) in the experimental I-V curves. It is considered that the iron film with thickness less than 10 Å has a bct structure. For the (11) beam, an analogous consideration can be applied. According to this model, in iron film more than 10 Å average thickness, domains of bct Fe(001) structure and of bcc Fe(001) structure coexist. For trial, I-V curves for bct Fe(001) surface has been added to those for bcc Fe(001) surface in the ratio of 0.7 bct to 0.3 bcc. The results are shown in Fig.35 in comparison with those for iron film on MgO(001) surface of 19Å average thickness. Although the agreement of these curves is not sufficient, the experimental results seem to be explained by this model as a first approximation. As these calculations have been carrid out under the condition of T=0 K, relative peak intensities will be improved by taking a temperature effect into account.

§5. Electronic structure of iron films

5-1. Iron films on Si(111) surface

In section 3-1-3, ARUPS spectra for iron films with various thicknesses annealed at both low temperature (350°C) and high temperature (500°C), are shown. In order to compare two corresponding spectra of the same film thickness more precisely, the difference spectra are displayed in Fig.36(a) which are obtained by subtracting the spectra shown in Fig.18(a) from those in Fig.19(a). It is indicated in the figure that the intensity at E_B=0.8eV has decreased and that the intensity at E_B=2eV has increased. In other words, a part of the electronic state of the adsorbate has shifted to the higher binding energy side. This phenomenon is notable for the films more than 0.6Å thick, that is, for the films which have had phase transition from 1x1 to 2x2 superstructure. It is therefore believed that this is caused by a change of the sit-site of adsorbed iron atoms. Further, it seems that the intensity at E_B=6.8eV has again increased for the very thin films less than 0.4Å thickness. It cannot yet be determined, however, whether this is caused by a change of electronic state or by the impurity atoms adsorbed on the surface.

In Fig.36(b) and (c), corresponding difference spectra for the other experimental conditions are shown together. Figures (a) and (b) are plotted in the same scale of the intensity, while (c) is contracted to 1/5 scale. Firstly, the dip at E_B=0.8eV in the spectra seems to increase nearly in proportion to the amount deposited. However, the peak intensity at E_B=2eV peculiar to the 2x2 structure does not show such a tendency. The height of this peak decreases again for the films more than 1ML (~0.8Å) thick. It is likely that for films more than 1ML thick, the sit-site in the case of the 2x2 struc-

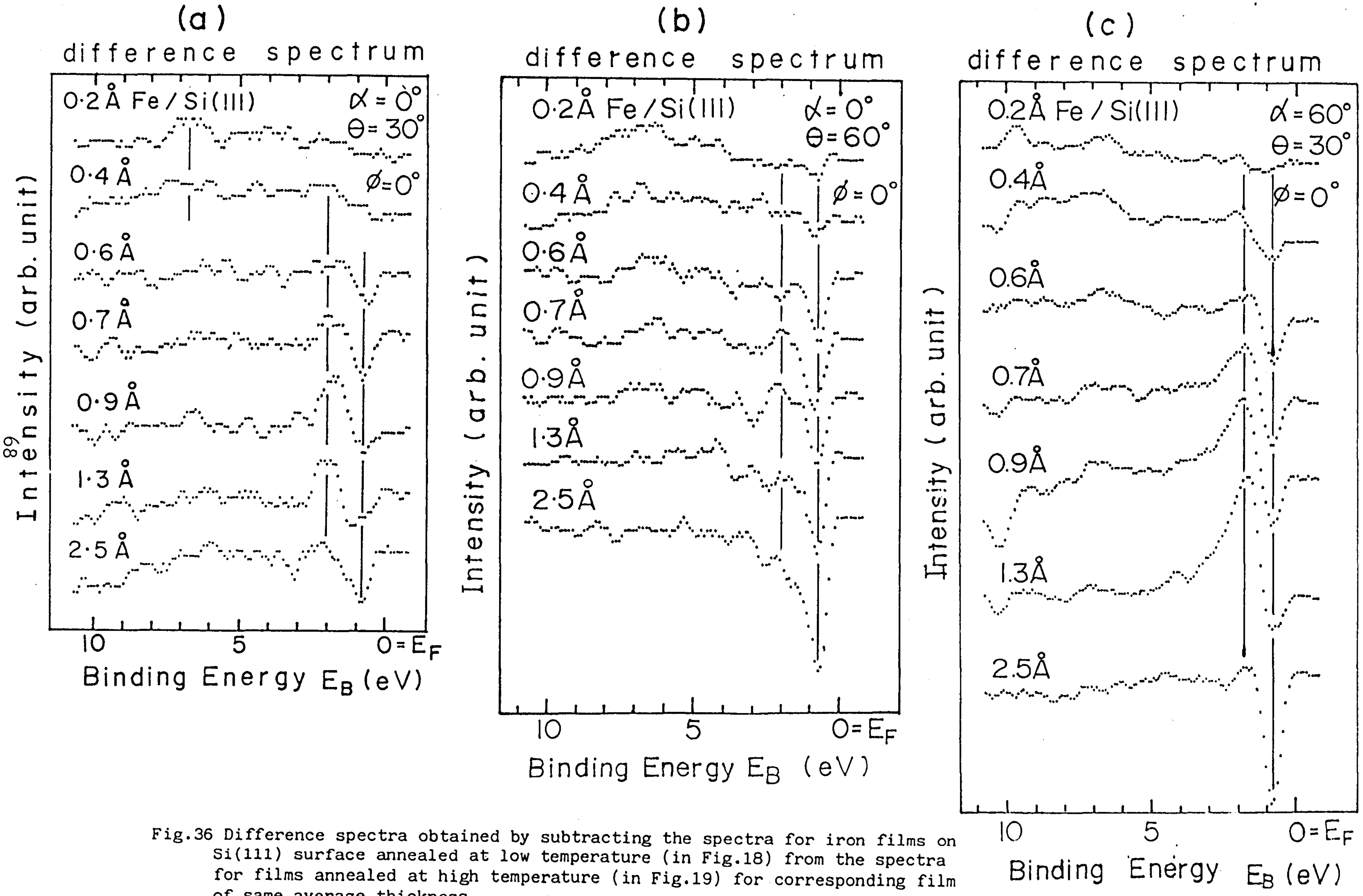

Fig.36 Difference spectra obtained by subtracting the spectra for iron films on Si(111) surface annealed at low temperature (in Fig.18) from the spectra for films annealed at high temperature (in Fig.19) for corresponding film of same average thickness.

ture was already occupied by excess iron atoms. On the other hand, because, as mentioned in section 3-1-1, iron atoms on the surface decrease in number after annealing at high temperatures, the dip at E_B=0.8eV continues to decrease for films more than 1ML thick.

Secondly, when the spectra in Fig.36(b) are compared with those in Fig.36(a), the peaks peculiar to the 2x2 structure are relatively small to the dips. That is, these peaks are sensitive to the direction of emission. If the final state in eq.(3.1) can be approximated by a plane wave, eq.(3.1) can be replaced by

$$\frac{d\sigma}{d\Omega} \propto \cos^2(\vec{A},\vec{k}_f)\ |\psi_i(\vec{k}_f)|^2 \qquad (5.1)$$

where $\vec{k}_f$ is the wave vector of an outgoing plane wave and $\psi_i(\vec{k}_f)$ is the Fourier transform of initial state[45]. In the case of atomic-like orbitals, the angular distribution of wave functions in real space and that in Fourer space are identical. According to this equation the angular distribution of electron emission directly reflects the orbital symmetry and orientation of the initial state. In this study, because unpolarized light is used, $\cos^2(\vec{A},\vec{k}_f)$ must be averaged over a direction angle of $\vec{A}$. In the case of normal incidence, as $\vec{A}$ is within a plane parallel to the surface, when the emission angle (θ) becomes large, the contribution from this term becomes large. Although the dips at E_B=0.8eV have such a tendency, the peak peculiar to the 2x2 structure shows an opposite behaviour. Then, these two states seem to have different angular distributions.

Thirdly, when the spectra in Fig.36(c) are compared with those in Fig.36(a), the peak heights peculiar to the 2x2 structure are relatively large in comparison with the magnitudes of dips. This shows that this peak is very sensitive to the incident angle of light.

Since the emission angle is the same for both cases ($\theta=30^\circ$), the contribution of the factor $\cos^2(\vec{A},\vec{k}_f)$ in eq.(5.1) should be considered.

In order to investigate angular and polarization dependence of emission more precisely, many energy distribution curves depending on the polar angle of emission (θ), the azimuthal angle of emission (ϕ) and the polar angle of incident light (α) were measured. An example of difference spectra of polar angle dependence for about 1ML thick film is shown in Fig.37. These spectra are also obtained by subtracting the spectra for the films annealed at low temperature from the spectra for the films annealed at high temperature. In this figure, besides the dip at E_B=0.8eV and the peak at E_B=2eV, another peak appears at E_B=3eV. Moreover, though the peak height at E_B=2eV increases with the emission angle up to about $\theta=30^\circ$, the peak height at E_B=3eV seems scarcely to change. That is, two peaks of electronic state both peculiar to the 2x2 structure have a different angular symmetry each other.

However, it is pointed out that the plane wave approximation of the final state is not very realistic in general and at least the effect of scattering of the outgoing wave by the surroundings should be taken into account[8,46]. This theory is briefly considered in Appendix H. In the real adsorbate system, as the initial state is not so localized, more complicated superposition of outgoing waves must be considered. In either case, at the present time it can not be indicated that these peaks or dips mentioned above correspond to what kind of electronic states, and further experiments and theoretical consideration based on a realistic structure model are required.

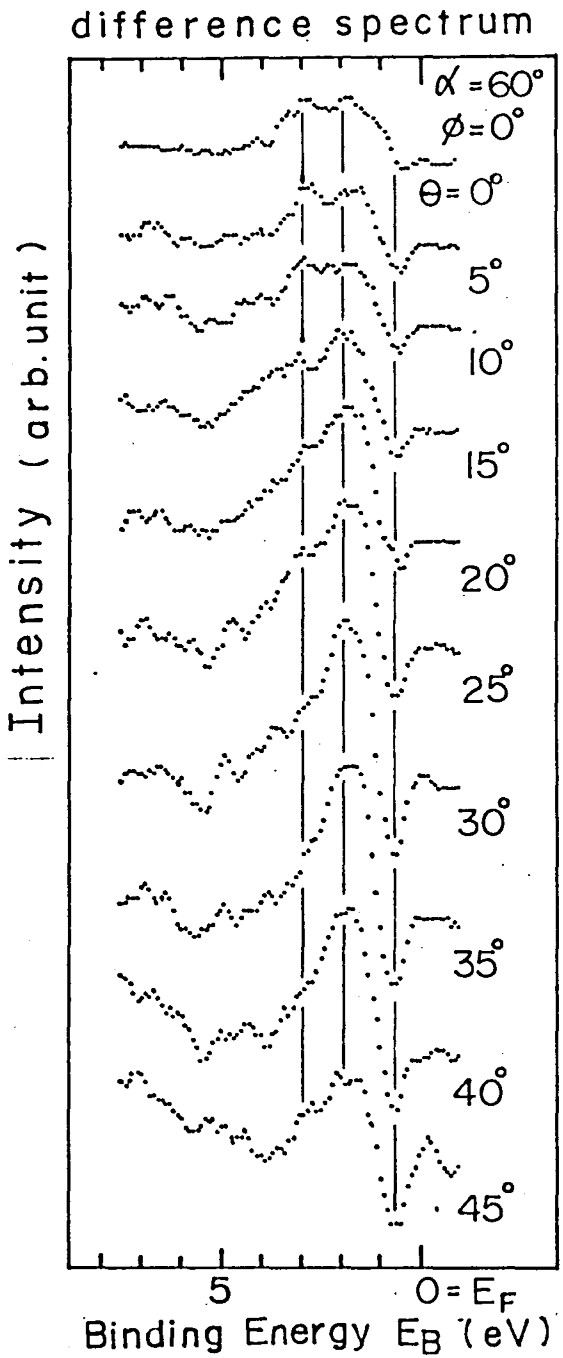

Fig.37 Difference spectra for the iron film of about 1ML thickness on Si(111) surface for various polar angles of emission in the case of glancing incidence of light.

5-2. Iron films on MgO(001) surface

In sections 3-2 and 4-2, it is indicated that iron films deposited on MgO(001) surface grow layer-by-layer and form an Fe(001) epitaxial film at room temperature. It seems that the iron film is pseudomorphic in early stage and begins to change from bct to bcc structure at the stage of about 10 Å average film thickness. At the same time, Fe-MVV Auger peak height (peak-to-peak amplitude in dN(E)/dE curve) indicates a curious behaviour (see Fig.20).

It is considered that this behaviour on the changing rate of Auger peak height is caused by the following reasons: (i) The sticking coefficient of coming flying atoms changed, (ii) the film growth mode changed, or (iii) an electronic state which is concerned for the MVV Auger transition changed. Of these, in the case of suspected causes (i) and (ii), other Auger signal also must show the same abnormal behaviour. Then, the suspected cause (iii) seems to be most probable.

As mentioned in Appendix A, due to the restriction of the signal-to-noise ratio, usually, the peak-to-peak amplitude in the derivative of the energy distribution curve (dN(E)/dE curve) is recognized as an Auger peak height. It is reasonable as far as the peak shape in the energy distribution curve (N(E) curve) is analogous, that is, the peak width does not change. In the case that the peak shape changes, however, the peak-to-peak amplitude does not show the intensity of the Auger peak correctly and an integrated intensity of the Auger peak in N(E) curve must be estimated. In this case, as the crystal structure of an iron film seems to change, it is not surprising that the electronic state has changed.

Therefore, the integrated intensity of Fe-MVV Auger peak has been estimated. Since it is difficult to measure directly the peak intensity in N(E) curve due to the restriction of S/N ratio, it has been obtained by integrating the dN(E)/dE curve. The principle of this procedure is shown in Fig.38. Because the Fe-MVV Auger peak exists at the position where the slope of the back ground due to the true secondary is very steep, this back gruound has been subtracted from a raw dN(E)/dE curve approximately at first. For the approxi-

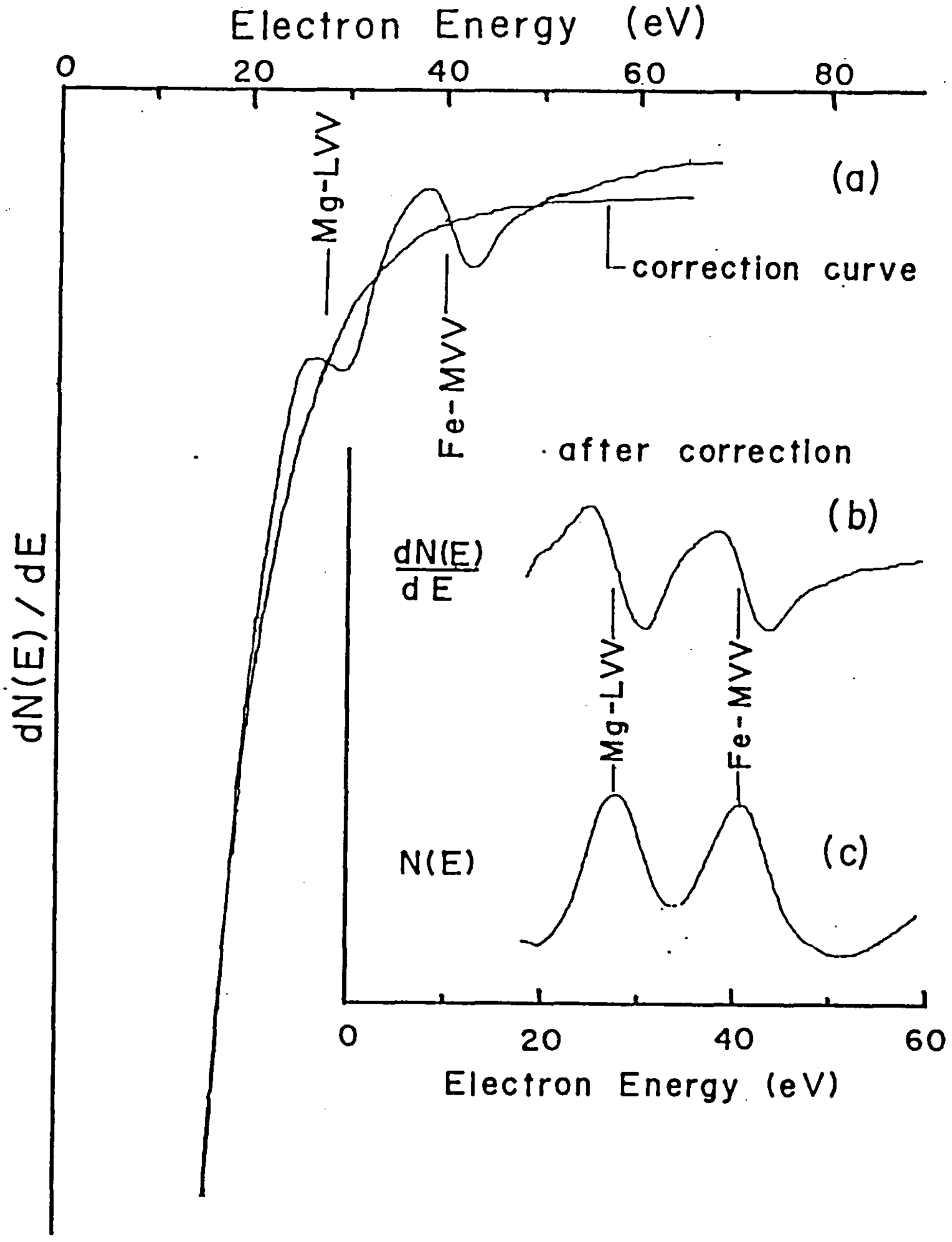

Fig.38 The principle of searching for N(E) curve by means of integration of the dN(E)/dE curve after the subtraction of the background. (a) An approximate curve ("correction curve") is adjusted to coincide with the back ground of the experimental dN(E)/dE curve, (b) The "correction curve" is subtracted from the experimental curve, and finally, (c) the dN(E)/dE curve is integrated.

mate curve of the back gruond, the characteristic curve of current vs. voltage in correct order of the silicon diode has been used[47]. An example of this curve is indicated in the figure as the "correction curve". In order to coincide with the experimental curve, this curve is adjusted by four potentiometers with a specially designed circuit for this purpose, where the position of up and down, the position of right and left and the curvature of this curve can be adjusted.

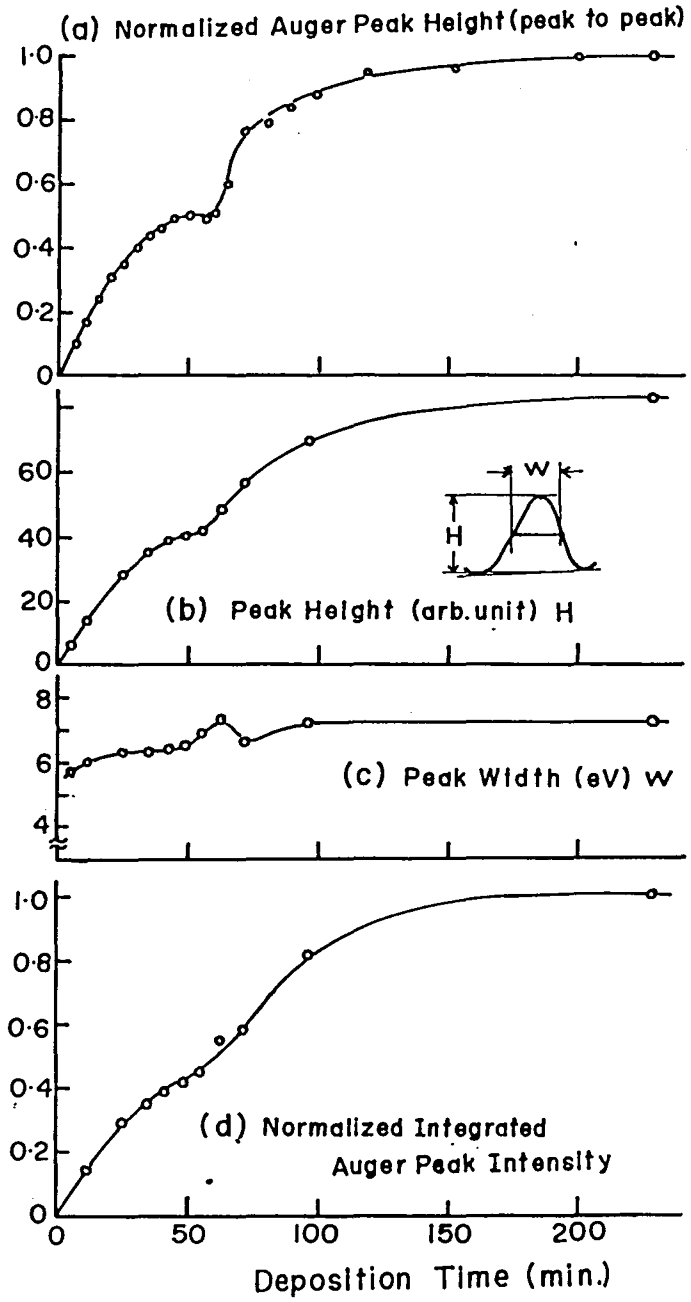

Fig.39 Change of the Fe-MVV Auger signal: (a) peak-to-peak amplitude in the dN(E)/dE curve, and (b) peak height, (c) peak width, (d) integrated intensity in the N(E) curve.

In Fig.38(b), the dN(E)/dE curve after the subtraction appears on almost flat back ground. Finally, this curve is integrated by means of an integration circuit and the result is shown in Fig.38(c).

At the various stages of the average film thickness, this procedure has been carried out and the peak widths of Fe-MVV Auger peak in N(E) curve are estimated. Results are shown in Fig.39. From the top, (a) peak-to-peak amplitude in dN(E)/dE curve, (b) peak height in N(E) curve, (c) peak width in N(E) curve, and (d) an integrated intensity in N(E) curve calculated manually are shown, respectively. At the stage of unusual behaviour in curve (a), the peak width becomes wide in curve (c). Consequently, though the curve (d) is not thoroughly smooth, a curious behaviour is rather moderated.

Next, it is considered that why the width of Fe-MVV Auger peak has changed. Because the valence-band electronic state is very sensitive to the atomic structure, i.e., to the nearest neighbour distance, it is reasonable to consider the simultaneous change of the electronic

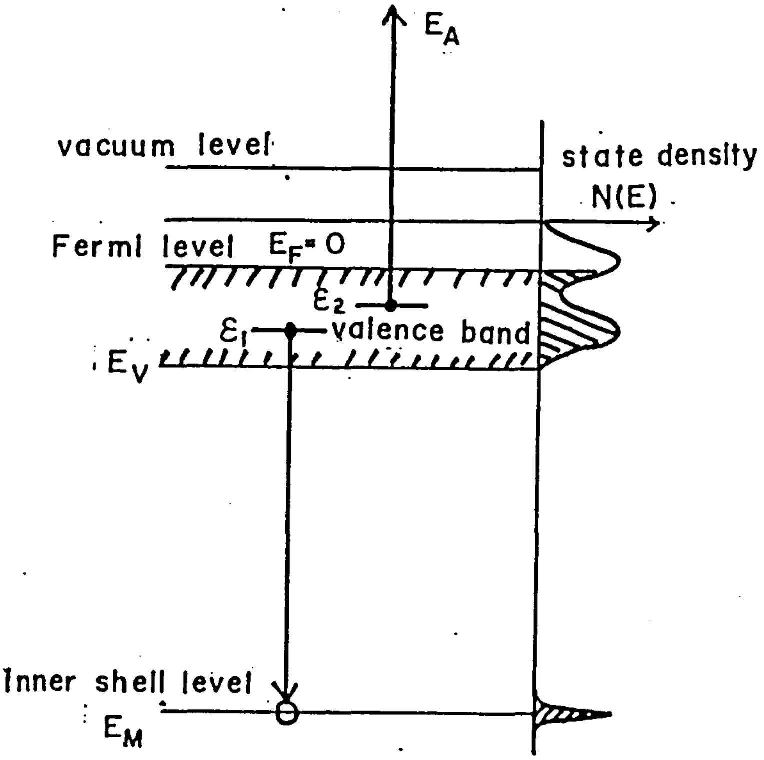

Fig.40 Schematic diagram of the MVV Auger transition.

state when the structure of the film has changed. In section 4-2, it is suggested that the structure has begun to change from the body-centered tetragonal to the body-centered cubic structure. According to this model, the nearest neighbour atomic distance changes from 2.51 Å to 2.48 Å.

On the other hand, as is shown in Fig.40, the valence-band electronic state concerns twice in Fe-MVV Auger transition. Then, the energy distribution curve of this Auger peak reflects self-convolution of the density of states.

Heine has indicated that the d-band width at the Γ point shrinks in proportion to the inverse fifth power of the lattice constant48). Following this concept, as the nearest neighbour atomic distance in bct phase is larger than that in bcc phase by 1.2 %, the band width becomes narrower by about 6 %. Then, simply speaking, the Auger peak width in the energy distribution curve in bct phase is narrower than that in bcc phase by about 12 %. In Fig.39(c), at the stage of 11 Å film thickness the peak width has changed from 6.3 eV to 7.2 eV. This change may correspond to the value of the rough estimation mentioned above. In this respect, because photoemission spectrum can be regarded as one-electron process, ARUPS measurements are in preparation now.

§6. Summary

A compound apparatus for angle resolved ultraviolet photoelectron spectroscopy (ARUPS) and low energy electron diffraction (LEED) - Auger electron spectroscopy (AES) has been constructed. A 127° type coaxial cylindrical analyzer on a turn table and a discharge type UV source are installed in a lower stage. The electrodes of LEED optics and an evaporation source are installed in another upper stage. A long-stroke sample manipulator transfers the sample between these stages.

A simple semi-automatic system of LEED spot-tracing has been developed. Principal idea is as follows; the spot-photometer is driven manually, then the electron energy is changed automatically so that the spot moves to the position where it is measured by the photometer.

Making use of these equipments, MgO(001) clean surfaces and deposited iron films on Si(111) and MgO(001) surfaces have been investigated. MgO(001) clean surfaces prepared by three different heat treatments show similar I-V curves one another, and the theoretical curves with no relaxation or with smallest one (2.5% expansion) obtained by dynamical calculations fitted best with the experimental curves. Further, the change of the degree of the surface rumpling due to heat treatments cannot be recognized. However, it is difficult to determine whether it has been rumpled or not.

Iron film deposited on Si(111)7x7 surface grows layer-by-layer and forms an bcc Fe(111) epitaxial film at room temperature. According to LEED I-V curves at various stage of average film thickness, it seems that an iron film is pseudomorphic at early stage. However, owing to annealing at temperatures higher than 400°C, iron atoms infiltrate into the Si substrate and the structure of films with more than 1/2 monolayer (ML) thickness has changed from 1x1 to 2x2 superstructure. At the same time, a shift of iron d-band electronic state to higher binding energy side has been observed by ARUPS. It has been also found that the peak intensity peculiar to 2x2 structure is sensitive to the angle of incident light as well as to the direction of emission. Further experiments of the angular distribution of emission and theoretical consideration based on a realistic structure model are required.

Iron film deposited on MgO(001) surface grows layer-by-layer and forms a bcc Fe(001) epitaxial film at room temperature. According to the comparison of LEED I-V curves, at the stage of 1 ML an iron film is pseudomorphic and iron atom sits just above an oxygen ion. Iron films begin to change from body-centered tetragonal to body-centered cubic structure at about 10 Å average thickness and at the same time a widening of valence-band electronic state has been observed by AES. In order to get more precise knowledge, ARUPS measurements are in preparation now.

Acknowledgement

The author wishes to express his sicere thank to Prof. T.Kanaji of the Kobe University for his constant help and encouragement through the every stage of this investigation. Several ideas of the design of the experimental apparatus have been resulted from the discussion with him. The author is greatly indebted to Prof. N.Kunitomi of the Osaka University for his helpful discussions and encouragement. The author is very grateful to Prof. F.Fujimoto of the University of Tokyo, Dr. Y.Nakai of the Osaka University and Dr. M.Kaburagi of the Kobe University for their helpful discussions.

The author would like to thank Prof. Y.Murata of the University of Tokyo for his supplying with a beneficial information concerning the UV source and to thank Dr. K.Terakura and Mr. W.Okamoto of the University of Tokyo for the offer of theoretical I-V curves on rumpled MgO(001) surface and to thank Dr. A.Yagishita of the National Laboratory for High Energy Physics for supplying with his design for the 127° type coaxial cylindrical analyzer. The author is pleased to acknowledge their cooperations of Messrs. H.Nakatsuka, Y.Taki, J.Sakamoto, K.Nai and T.Ogawa on each part of this study.

Appendix A. A conventional LEED-AES syetem

A conventional 4-mesh LEED-AES system is shown in Fig.41. Concentric four grids and a collector with a sample situated at their center of curveture are indicated in the figure. In both (L/A) modes the sample and the grid nearest to the sample are grounded to give a field-free region between the grid and the sample in order to ensure that secondary electrons produced at the center of curveture of the optics should travel in radial paths towards the first grid.

In the LEED mode, next grids, $M_{2,3}$, are grounded too, and the fourth grid, M_4, has a suitable negative potential to prevent electrons which have lost the energy from passing through the grid. This improves the S/N ratio of the brightness of the fluorescent screen. To the fluorescent screen, high voltage (about 3kV) is supplied and the scattering pattern is observed through a viewing port. Electron energy can be varied by changing a negative potential supplied to an electron gun.

In the AES mode, the two grids, $M_{2,3}$, have the retarding potential to prevent electrons which have an energy less than that corresponding to this potential from passing through the grids. Two grids are used in order to sharply define the radial retarding field, and this is a necessary requirement for high resolution. In order to obtain an energy distribution curve, these grids are supplied with the ac modulation voltage superimposed on the dc retarding potential. The fourth grid, M_4, is held at ground potential as an ac shield to reduce the capacitive coupling to the collector. The collector is biased a few hundred volts positive. This bias voltage ensures that most of the secondary electrons produced at the collector are returned to the collector.

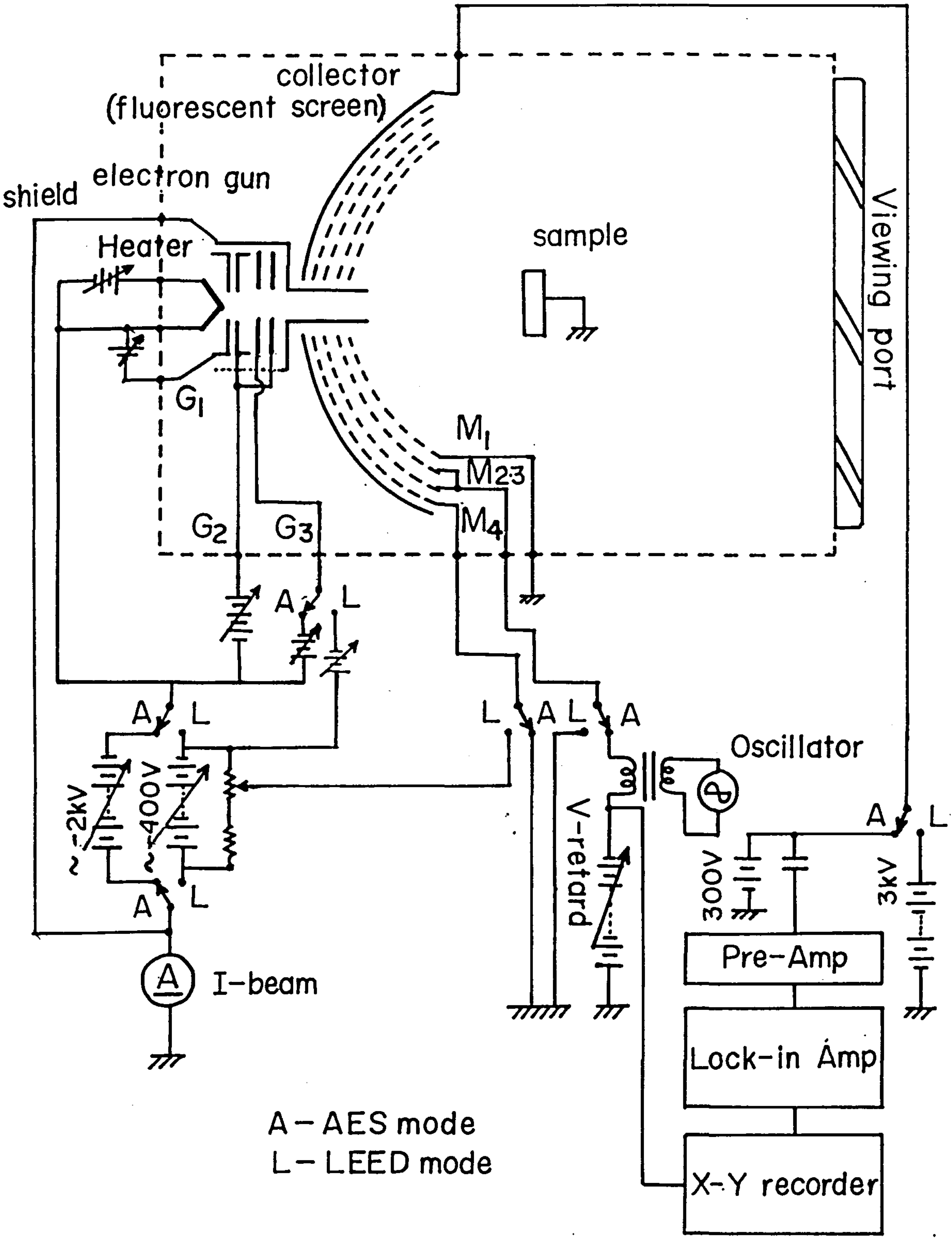

Fig.41 Composition of a conventional LEED-AES system.

If now the sample is excited by electrons of energy, eV_0, and the current to the collector, I(V), is recorded as a function of the retarding voltage, V, (that is, corresponds to kinetic energy, E,) sweeped from ground to $-V_0$, Fig,42(a) is obtained. To obtain an energy distribution curve, it is necessary to differentiate this curve with respect to the retarding voltage, that is, to determine dI(V)/dV curve as a function of V. This is effectively accomplished by tuning the detector to the frequency of the modulation (Fig.42(b)).

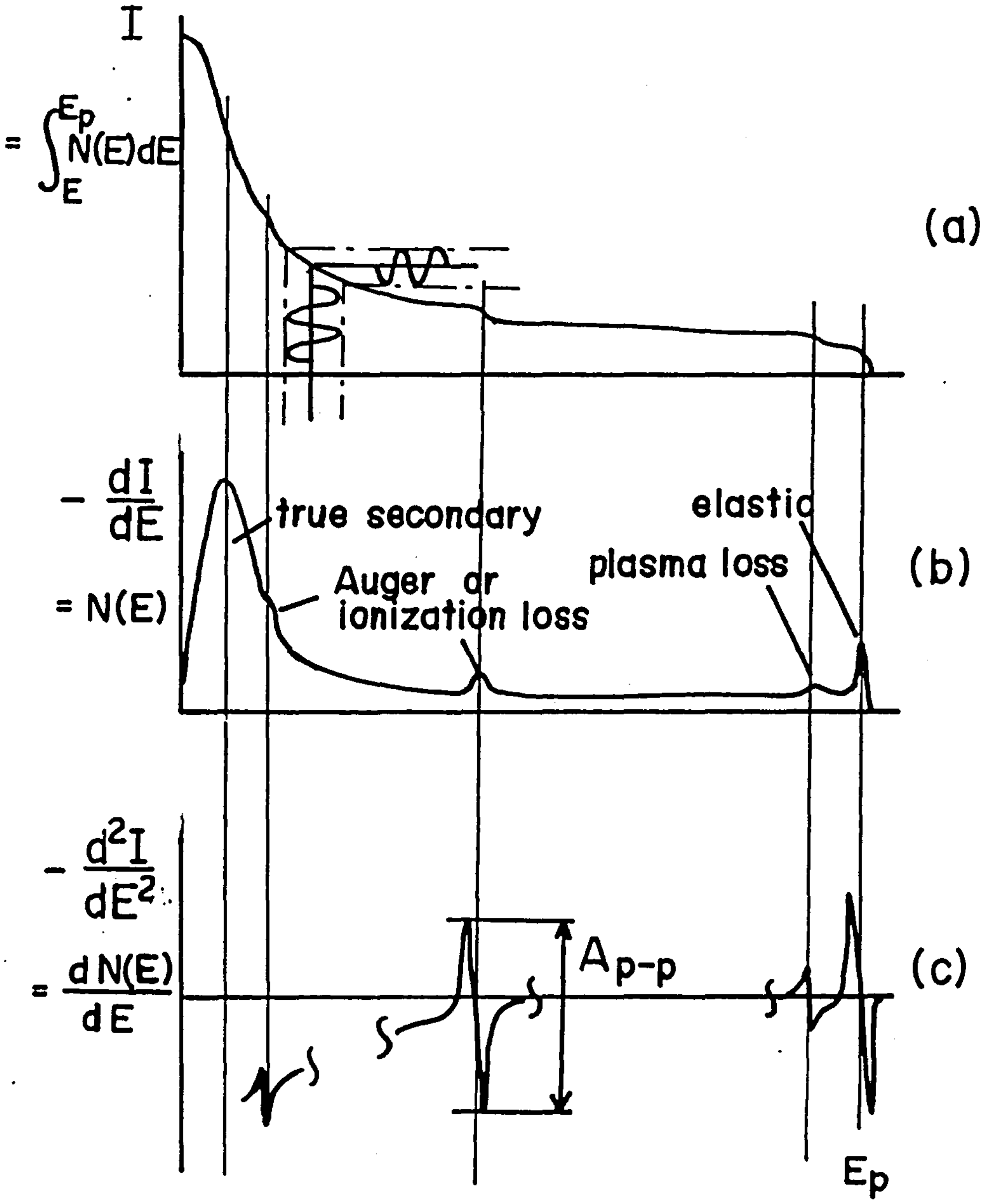

Fig.42 Principles of energy analysis by the retading method.

In order to obtain the derivative of the energy distribution curve, i.e. $d^2I(V)/dV^2$, the detector is tuned to the second harmonic of the modulation frequency (Fig.42(C)). To do these, the lock-in-amplifier principle of synchronous phase sensitive detection is invaluable. Usually, the peak-to-peak amplitude ,A_{p-p}, in Fig.42(c) is recognized as an Auger peak height.

Appendix B. Principle of focal properties of input lens and the determination of best operation

The principles of focal properties are shown in Fig.43[17)]. Figure.43(A) shows an example which uses three electrodes. The letters of E, E_1+E and E_0 indicated in Fig.43(A)(a) correspond to the kinetic energies when an electron penetrates each electrode. Namely, E is the incident energy. The loop in Fig.43(A)(b) indicates the focal locus, and indices on the focal locus indicate the magnification ratio (amplitude ratio of image to object). If we can generate a

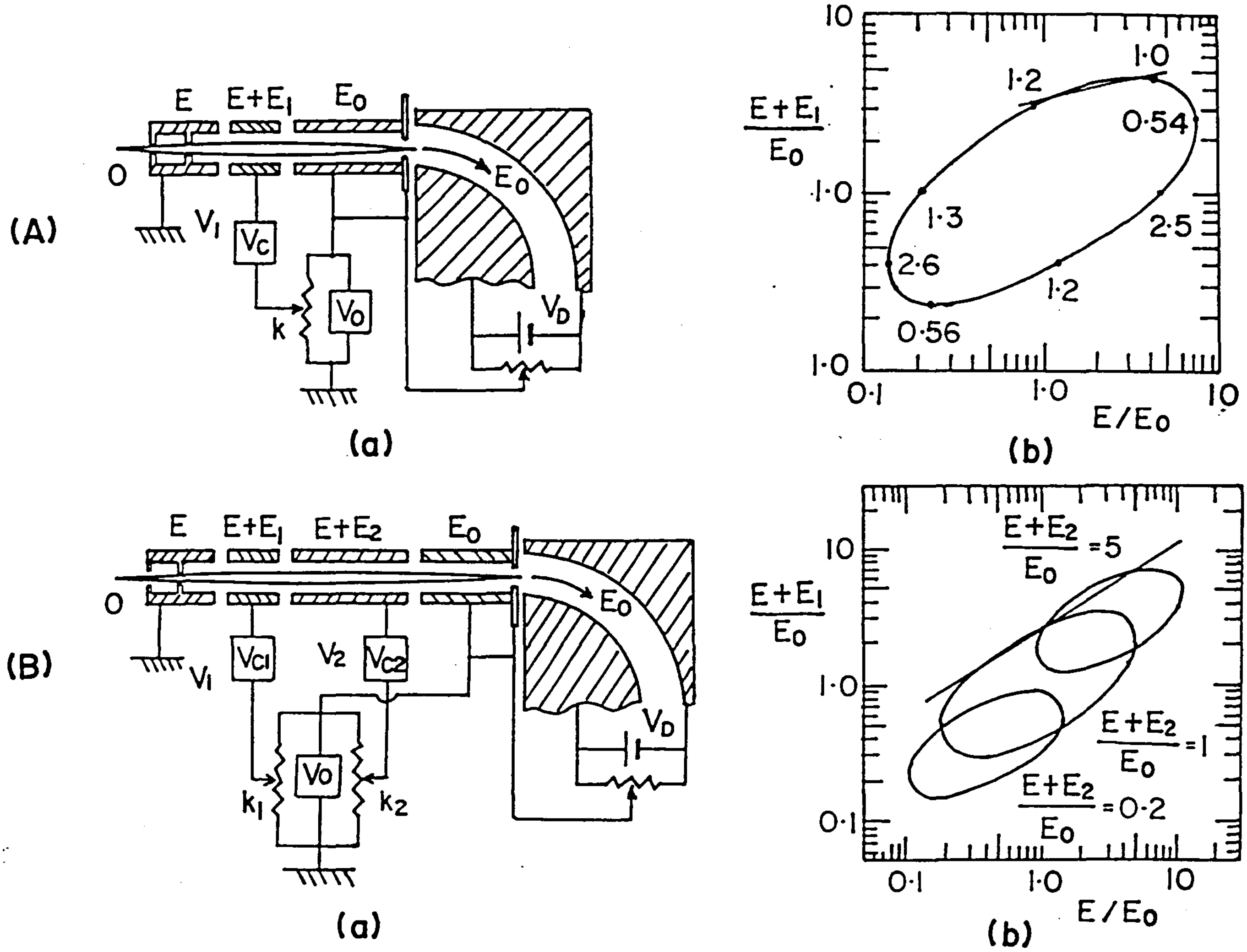

Fig.43 Schematic diagram of focal properties with input lens system[17)], (A) a lens composed of three electrodes, (B) a lens composed of four electrodes, and (a) electric circuit to remove the aberration effect, (b) focal locus.

voltage, $V_1=E_1/e$, which changes along the focal locus with a suitable power supply, the position of an image is always on the slit of incidence. It is desirable that it changes along upper half part of the focal locus because the change of magnification is small.

In Fig.43(A)(a), an electric circuit is indicated and when a retarding voltage, V_0, changes, a potential of the middle electrode keeps the condition of $V_1= kV_0+V_c$ automatically. If we adjust the ratio of the potentiometer, k, and a suitable voltage, V_c, we can sweep along the upper half curve in Fig.43(A)(b) approximately.

In Fig.43(B), an example of four-electrode lens syetem which is an improved one to spread the region which can be approximated is shown. The potentials of the two middle electrodes are changed to keep the conditions of $V_1=K_1V_0+V_{c1}$ and $V_2=k_2V_0+V_{c2}$, respectively.

The input lens system shown in Fig.3 is a four-element lens. L_1, L_2 and L_3 are the elements of it. L_4 and L_5 form a deflector, however, in this study L_4, L_5 and L_6 are connected at the same potential and treated as the fourth element of input lens. Therefore, the electrons are once focused at the point A in Fig.3. Further, two electrodes (L_6 and L_7) compose a retarding lens, and finally electrons are focused at the slit of incidence. The potential difference between L_6 and L_7, "$V_{6,7}$" in Fig.3, is 20V. If $V_{6,7}$ is changed, the object position of the retarding lens (position A) changes, and it can give a zoom action.

In order to obtain the best operation of the input lens system experimentally, an electron gun has been put at the "Ist stage" in Fig.1 and a very weak electron beam has been injected into the lens directly. In order to produce a focal locus resemble to the loop in Fig.43(A)(b), the measurements have been repeated many times by changing several parameters. An example shown in Fig.44(a) indicates a variation of the counting rate when the potential of the electrode, L_2, is changed under the constant potentials of other electrodes. The electron energy passing through the deflector, E_0, is 5eV. The transverse axis corresponds to a longitudinal traverse in Fig.43(A)-(b), and two peaks in Fig.44(a) correspond to the points where those traverse the focal locus. The larger peak in the left hand side and the small peak in the right hand side in Fig.44(a) are correspond to the focal points in the upper part and the lower part in Fig.43(A)-(b), respectively.

By changing the incident energy, E, similar measurements have been repeated to obtain the focal locus and an example of such experiments is shown in Fig.44(b). $E+E_2$ and $E+E_3$ indicate the energies passing through the electrodes, L_2 and L_3, respectively. Although

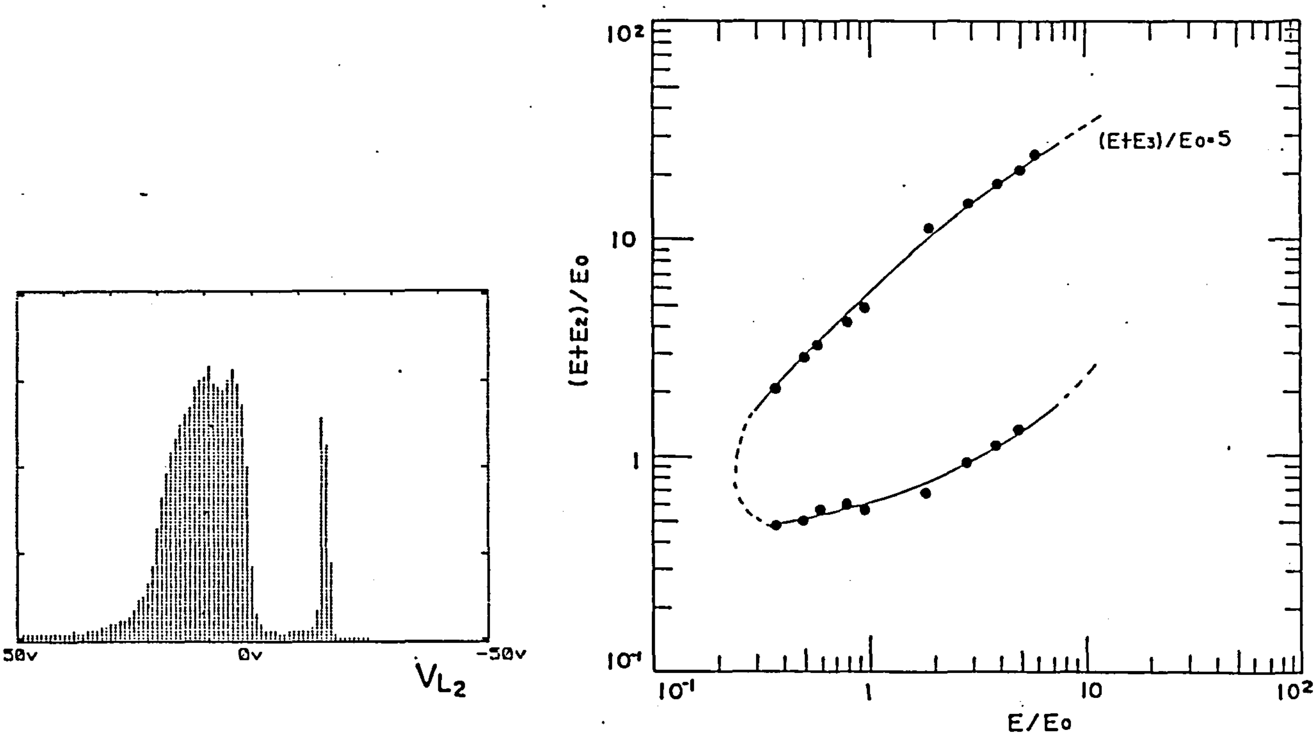

(a)

(b)

Fig.44 (a) An example of variation of countig rate when the potential of the electrode, L_2, is changed, (b) An example of experimental focal line obtained by changing an incident energy.

the focal line does not draw a full loop, this curve shows a character similar to Fig.43(A)(b).

Further, by changing the parameter, $(E+E_3)/E_0$, similar measurements have been repeated to obtain a focal locus as much as straight in the energy range for UPS under the condition in which K_2 and k_3 are not larger than unity. Finally, a following good combination has been found,

$K_2 = 0.20$, $V_{20} = 12.65$ V,
$k_3 = 1.0$, $V_{30} = -1.85$ V.

In this case, the parameter, k_3, is unity. This means that the electric circuit becomes similar with that in Fig.43(A)(a) rather than that in Fig.43(B)(a), that is, this input lens system operates like as three-electrode lens. Because the energy range of the photoelectrons is narrow, the combination mentioned above gives a sufficient performance.

Appendix C. Corrections of geometrical assumptions for LEED spot-tracing

When the geometrical assumptions indicated in section 2-2 are not realized, eq.(2.4) is not satisfied exactly. If a sample is not set at the center of the sphere which is concentric with the segmental sphere of the fluorescent screen, and the shift in the direction parallel to incident electron beam axis is indicated as Δy, eq.(2.4) is modified as,

$$E = \frac{1}{2m} \left(1 + 2\frac{\Delta y}{r_0}\right) \left(\frac{r_0 h}{d_{hk}}\right)^2 \frac{1}{x_{hk}^2} \ . \qquad \text{(A.1)}$$

Since the deviation of electron energy depends not on x_{hk} but on the value of A_{hk}, this is corrected by the adjustments of VR_1' and VR_2 in Fig.5.

If the normal incidence of primary electrons is not satisfied, eq.(2.4) is modified as,

$$E = \frac{1}{2m} \left(\frac{r_0 h}{d_{hk}}\right)^2 \frac{1}{x_{hk}^2 \left(1 + \frac{x_{hk}^2}{4r_0^2} + \frac{x_{hk} \cdot x_0}{r_0^2}\right)} \qquad \text{(A.2)}$$

where x_0 is the distance of (00) spot from the center of a fluorescent screen, and the x_{hk} is the distance of (hk) spot from the (00) spot on the "plane" of projection. This effect can be regarded as a second-order effect and practically neglected up to the value of θ about 10^c. In fact, in our experimental arrangement the center of the spot has been observed always nearly at the center of the aperture of the photometer over the whole range of electron energy.

Finally, although the neglection of the inner potential, V_{0r}, is not correct, this effect corresponds to a shift of electron energy by an amount, V_{0r}, and can be corrected due to a suitable voltage biased.

Appendix D. Discrimination methods of film growth mode based on AES

Two discrimination methods of film growth mode based on AES have been proposed. These are the Palmberg's criterion[23)] and the Jackson's criterion[24)]. The Palmberg's criterion is considered as follows. Each electron produced in a solid has an individual escape length corresponding to its energy shown in Fig.45[40)]. Therefore, if a film grows in layer-by-layer mode, normalized Auger peak height (normalized by the Auger peak height before deposition for the signal of the substrate material and normalized by the Auger peak height after sufficiently thick deposition for the signal of the deposited material) changes corresponding to each escape length with the film thickness as are shown in Fig.46(a)[49)]. However, if a film grows in Volmer-Weber mode and an island is in fully 3-dimensional state,

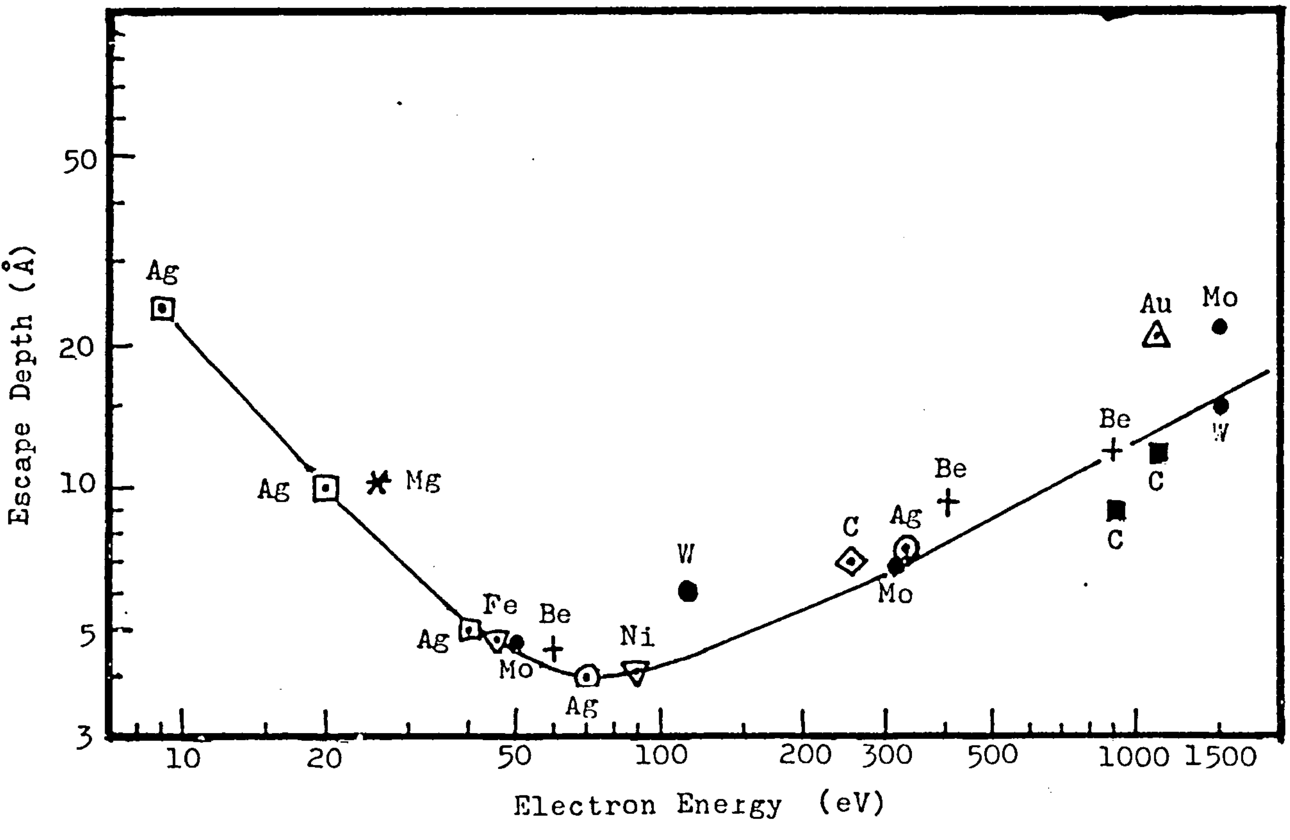

Fig.45 Relation between the electron escape length and its energy[40)].

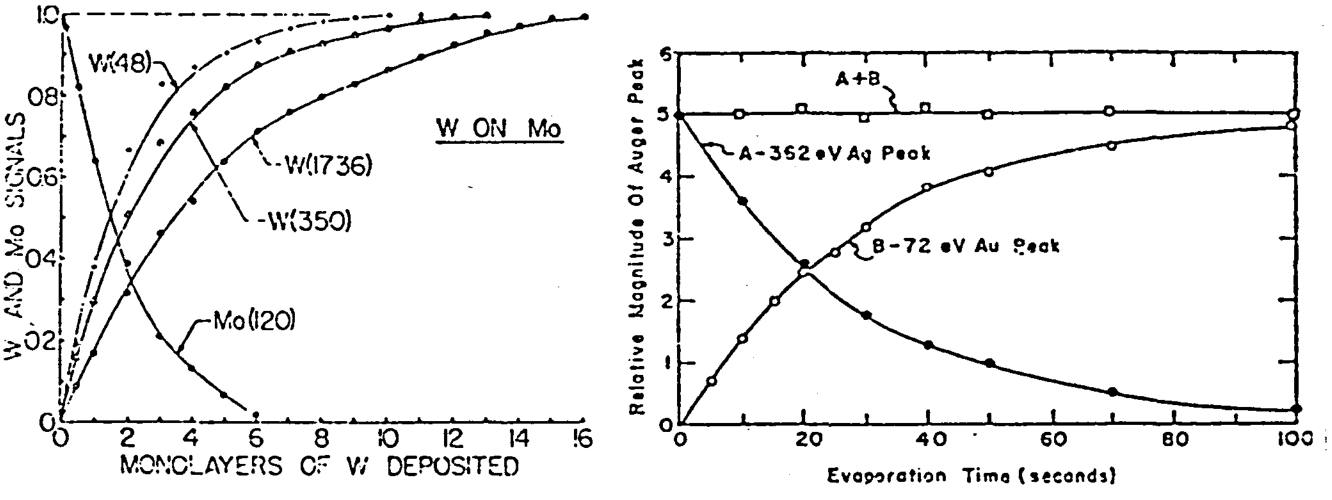

(a) (b)

Fig.46 Typical examples of the change of normalized Auger peak height during the film formation, (a) Frank-van der Merwe growth mode (ref.49) and (b) Volmer-Weber growth mode (ref.23).

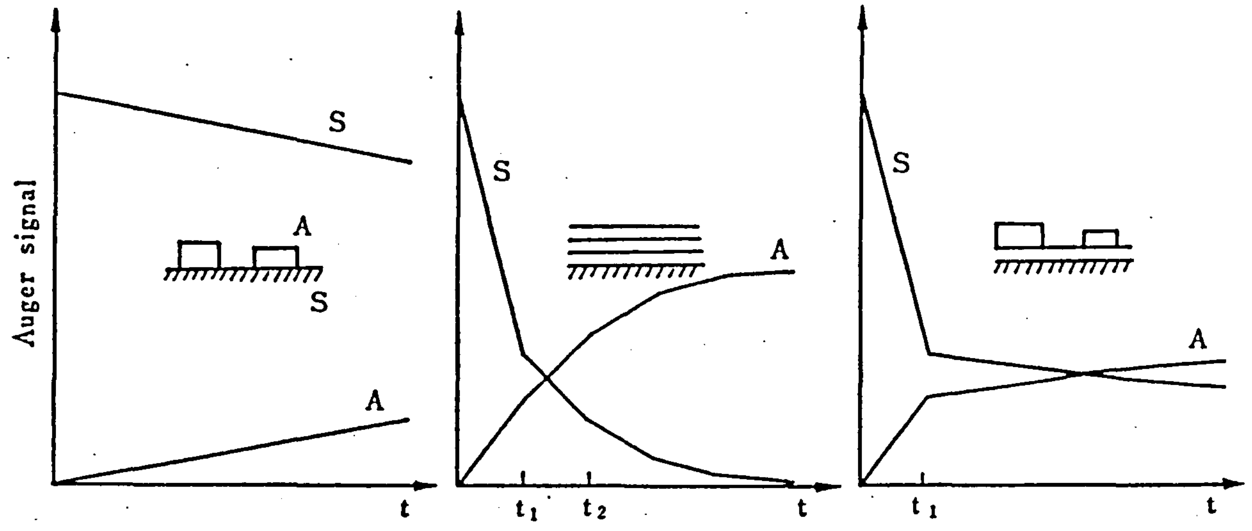

(a) Volmer-Weber (b) Frank-van der Merwe (c) Stranski-Krastanov

Fig.47 Variations of the Auger signals for the substrate S and the adsorbate A during the film growth by different mechanism (ref.50), t_1 is the time for the completion of the first monolayer.

normalized Auger peak height changes in accordance not with the escape length but with the area covered by the deposited material. Therefore, the sum of two normalized Auger peak heights is always unity approximately as is shown in Fig.46(b)23).

On the other hand, according to the Jackson's criterion, if a film grows in layer-by-layer mode, Auger peak height increases on a straight line with the film thickness up to the completion of first monolayer. Moreover, although the Auger signal increases on a straight line during the growth of second layer, the slope of this straight line is not equal to the first one but slightly gentle, because the Auger electron produced in the first layer of deposited material is absorbed by the second layer. Namely, the break point should appear at t_1 shown in Fig.47(b)50) schematically. How to change the Auger signals in other growth modes are shown in the figure.

Appendix E. Various modes of ARUPS

The angle resolved measurements of photoelectrons can be performed in various modes[7)]. One is to measure the angular distribution of emission as a function of the detector angle, namely, polar angle (θ) or azimuthal angle (ϕ) in Fig.17, under the condition that the incident polar angle (α) and the energy of the light are fixed. The change of energy position of the peak in the spectrum curves corresponding to different detector angle gives the two-dimensional dispersion relation in connection with $\vec{k}_{/\!/}$ (the component of the wave vector parallel to the surface). $|\vec{k}_{/\!/}|$ can be estimated from the following relation,

$$|\vec{k}_{/\!/}| = \hbar^{-1}\sqrt{2mE_k}\ \sin\theta \ , \tag{A.3}$$

where E_k is the kinetic energy of the photoelectron.

In the second mode, the incident angle (α) is varied, but θ and ϕ are fixed. The results with this mode are useful for the "symmetry analysis". The third mode is to fix both angles of incident light and the detector and to rotate the sample crystal around its normal. This mode is useful for the "symmetry analysis" too.

Recently, the light generated from the synchrotron radiation (SR) is sometimes used. In such a case, the wave length of the incident light can be changed continuously and the dispersion relations in connection with $\vec{k}_{\perp}$ (the component of the wave vector normal to the surface) are obtained. $|\vec{k}_{\perp}|$ can be estimated from the following relation for $\theta = 0^\circ$,

$$|\vec{k}_{\perp}| = \hbar^{-1}\sqrt{2m(E_k - V_{0r})} \ , \tag{A.4}$$

where V_{0r} is the inner potential. Further, because the light from the SR is polarized, measurements for the different polarization of the incident light are powerful for the "symmetry analysis".

Appendix F. LEED theory

In Table I representative theoretical treatments of LEED are shown. Among these theories, most frequently used procedure for dynamical caluculations mainly based on Pendry2) is surveyed below.

Table I. Representative theoretical treatments of LEED

L-space representation	k-space representation
T-matrix method (exact) Beeby(1968)51)	Bloch-wave method McRae(1968)53)
	Planar scattering Kambe(1967)55)
	Layer-KKR method Jepsen, Marcus & Jona(1971)54)
Reverse-scattring-Perturbation (RSP) method Zimmer & Holland(1975)52)	Renormalized-Forward-Scattring (RFS) perturbation method Pendry(1971)56)
	Layer-Doubling method Van Hove & Pendry(1975)57)

combined-space method
Tong & Van Hove(1977)58)

F-1. Calculation of phase shifts

In order to estimate the ion-core scattering of an imcident electron on a crystal, so-called the "muffin-tin approximation" is assumed, that is, the largest non-overlapping spheres (radius;R) drawn about each nucleus are considered and the potential inside is spherically symmetric and the potential outside is constant. The total spherical wave scattered from an ion-core is,

$$\phi^{(s)}(\vec{r}) = \sum_{\ell} i^{\ell+1}\sin(\delta_\ell)\exp(i\delta_\ell)(2\ell+1)P_\ell(\cos(\theta^{(s)}))h_\ell^{(1)}(\kappa r), \quad (A.5)$$

where, ℓ is the angular momentum, $\theta^{(s)}$ is the scattering angle, $\kappa=\sqrt{2E}$ is the amplitude of the wave vector in atomic unit, P_ℓ is the Legendre polynomial and $h_\ell^{(1)}$ is the spherical Hankel function of first kind. Therefore, a set of phase shifts, δ_ℓ, which characterizes a scattering amplitude of an ion-core must be calculated.

One-electron Schrödinger equation governing the motion of an incident electron is expressed with the Hartree-Fock approximation,

$$[-\tfrac{1}{2}\nabla_0^2 - \frac{z}{|\vec{r}_0|} + v_s(\vec{r}_0) - \sum_j \int \sum_{s_j} \frac{|\psi_j(\vec{r}_j,s_j)|^2}{|\vec{r}_0-\vec{r}_j|} d^3\vec{r}_j]\ \phi(\vec{r}_0,s_0)$$

$$-\sum_j [\int \sum_{s_j} \frac{\psi_j^*(\vec{r}_j,s_j)\phi(\vec{r}_j,s_j)}{|\vec{r}_0 - \vec{r}_j|} d^3\vec{r}_j]\ \psi_j(\vec{r}_0,s_0) = E\ \phi(\vec{r}_0,s_0), \quad (A.6)$$

where $\phi(\vec{r}_0,s_0)$ is the wave function of the incident electron and $\psi_j(\vec{r}_j,s_j)$ is the wave function of the core electrons. s_0 and s_j are spins of the incident and the core electrons, respectively. The first term in the bracket of the left-hand side is the kinetic energy, the second term is the Coulomb potential affected from a nucleus and z is the nuclear charge, the third term is the potential due to the screening charge and the fourth term is the electron correlation. The second term of the left-hand side arises out of considerations of antisymmetry under exchange of particles. For convenience, atomic units in which,

$$h^2 = m_e = e^2 = 1$$

are used. Therefore, the units of energy are Hartrees, 1H=27.2eV, and the Bohr radius is the unit of length, 1B.r.=0.5292A. Equation (A.6) is added with the correction term from the conduction electrons (optical potential; $V_0=V_{0r}+iV_{0i}$) and is solved by numerical integration which starts at the center of a nucleus and proceeds out to the boundary of the muffin-tin sphere.

On the other hand, the wave function outside the muffin-tin sphere has the form,

$$\phi_\ell(r) = \beta_\ell\{\exp(2i\delta_\ell)h_\ell^{(1)}(\kappa r) + h_\ell^{(2)}(\kappa r)\} \qquad (A.7)$$

where, β_ℓ is the amplitide of an incoming wave and $h_\ell^{(2)}$ is the spherical Hankel function of second kind. The first term is an outgoing wave and the second term is an incoming wave. Since the ion-core potential conserves the current when the electron moves away from the center, $h_\ell^{(1)}$ must have the same amplitude as the incident wave, but may differ in phase.

Finally, at the boundary of the muffin-tin sphere (r=R), the wave function solved eq.(A.6) inside the muffin-tin sphere is connected with the function in eq.(A.7) outside the sphere and a set of phase shifts is determined.

F-2. Kinematical theory

The crystal is divided into layers of ion-cores parallel to the surface. The layer can be divided into two-dimensional unit cells parallel to the surface. Because the ion-cores are arranged in a periodic structure within the layer, the scattered waves, $\phi^{(s)}$, from all ion-cores are added to give a set of diffracted beams. Descriptions of the wave field in terms of spherical waves or in terms of beams diffracted from the layer, are equivalent and may be used which is more convenient.

For convenience, it is considered that a layer is composed of single plane and there is single atom in a unit cell. The scattering matrix element among the incident plane wave, $\exp(i\vec{k}_0\vec{r})$, and the scattered plane wave, $\exp(i\vec{k}_{\vec{g}}\vec{r})$, for a single plane based on kinematical theory, is,

$$M(\vec{k}_{\vec{g}},\vec{k}_0) = \frac{8\pi^2 i}{|\vec{k}_0|A\ k_{\vec{g}z}} \sum_{\ell m} (-1)^m\ Y_{\ell -m}(\Omega(\vec{k}_0)) \times Y_{\ell m}(\Omega(\vec{k}_{\vec{g}}))\ \sin\delta_\ell\ \exp(i\delta_\ell) \qquad (A.8)$$

where $\vec{g}$ is a two-dimensional reciprocal vector, $\vec{k}_0$ and $\vec{k}_{\vec{g}}$ are the wave vectors of incident and diffracted wave, respectively. z is the direction of surface normal, A is the area of the unit cell and $Y_{\ell m}$ is the spherical function. Intensity of the diffracted beam is proportional to the square of a sum of the amplitude from successive layers,

$$I \propto \left|\frac{M(\vec{k}_{\vec{g}},\vec{k}_0)}{1 - \exp(i(\vec{k}_{\vec{g}}-\vec{k}_0)\cdot\vec{c})}\right|^2 \qquad (A.9)$$

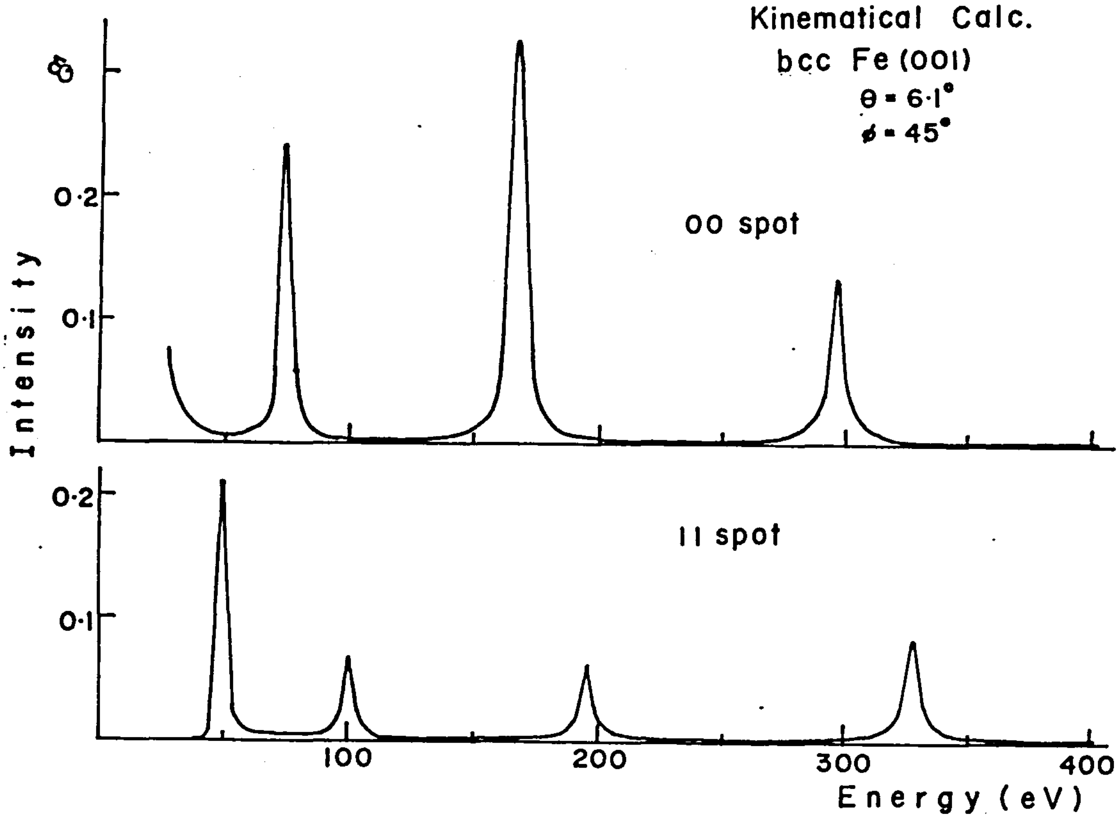

Fig.48 An example of intensity vs. energy spectrum for Fe(001) surface calculated in the kinematical theory.

where $\vec{c}$ is the vector which represents the displacement of equivalent successive layers. An example of I-V curve for Fe(001) surface is shown in Fig.48 for the sake of comparison with that of the dynamical calculation.

F-3. Dynamical calculation of diffraction matrices for single layer

For convenience, it is considered that a layer is composed of single plane. The total amplitude, $A_{\ell mk}$, of the incident wave on the k-th atom in the unit cell at the origin of the coordinates ($\vec{r}_{0k}$) is represented by a sum of the amplitude of incident electron, $A_{\ell mk}^{(0)}$, and the total amplitude of the wave coming up to the atom after scattering by other atoms, $A_{\ell mk}^{(s)}$,

$$A_{\ell mk} = A_{\ell mk}^{(0)} + A_{\ell mk}^{(s)} . \tag{A.10}$$

$A_{\ell mk}^{(s)}$ itself depends on $A_{\ell mk}$,

$$A_{\ell mk}^{(s)} = \sum_{\ell' m' k'} A_{\ell' m' k'} X_{\ell' m' k', \ell mk} , \tag{A.11}$$

then,

$$A_{\ell mk} = \sum_{\ell' m' k'} A_{\ell' m' k'}^{(0)} (1-X)_{\ell' m' k', \ell mk}^{-1} , \tag{A.12}$$

where,

$$X_{\ell mk, \ell' m' k'} = \sum_{\ell''+m''=\text{even}} C^{\ell}(\ell'' m'', \ell' m') \; F_{\ell'' m''}(kk') \; \exp(i\delta_{\ell}(k)) \sin\delta_{\ell}(k) , \tag{A.13}$$

$$C^{\ell}(\ell'' m'', \ell' m') = 4\pi(-1)^{\frac{1}{2}(\ell-\ell''-\ell')} (-1)^{m''+m'} \; Y_{\ell''-m''}(\tfrac{1}{2}\pi, 0) \; B^{\ell}(\ell'' m'', \ell' m') , \tag{A.14}$$

$$\begin{aligned} F_{\ell'' m''}(kk') = {\sum_j}' \, i h_{\ell''}^{(1)} \; (\kappa |\vec{R}_{0k'} - \vec{R}_{jk}|) \; \exp[-i m'' \phi(\vec{R}_{jk} - \vec{R}_{0k'})] \\ \times \; (-1)^{m''} \exp(i \vec{k}_0 \vec{R}_j) , \end{aligned} \tag{A.15}$$

$$B^{\ell}(\ell'' m'', \ell' m') = \int Y_{\ell m}(\Omega) \; Y_{\ell'' m''}(\Omega) \; Y_{\ell' -m'}(\Omega) \; d\Omega , \tag{A.16}$$

where $\sum_{j}'$ is the summantion over the two-dimensional lattice site excluding itself (j=0). Consequently, the scattering matrix element between the waves, namely, one is a plane wave impinging on sigle atomic layer, $\exp(i\vec{k}^{\pm}_{\vec{g}}\vec{r})$, and the other is a scattered plane wave, $\exp(i\vec{k}^{\pm}_{\vec{g}'}\vec{r})$, is,

$$M^{\pm\pm}_{\vec{g}'\vec{g}} = \frac{8\pi^2 i}{|k^{\pm}_{\vec{g}}|A\, k^{\pm}_{\vec{g}'z}} \sum_{\substack{\ell'm'k' \\ \ell mk}} \exp(i\vec{k}^{\pm}_{\vec{g}}\vec{r}_k - i\vec{k}^{\pm}_{\vec{g}}\vec{r}_{k'})$$

$$\times\ [i^{\ell}(-1)^m\, Y_{\ell-m}(\Omega(\vec{k}^{\pm}_{\vec{g}}))]\ (1-X)^{-1}_{\ell mk,\ell'm'k'}[i^{-\ell'}\, Y_{\ell m}(\Omega(\vec{k}^{\pm}_{\vec{g}'}))]$$

$$\times\ \exp(i\delta_{\ell'}(k'))\ \sin(\delta_{\ell'}(k')) \qquad \text{(A.17)}$$

Due to the energy and momentum conservation, $\vec{k}^{\pm}_{\vec{g}}$ has the relation with the wave vector of incident electron, $\vec{k}_0$ ($|\vec{k}_0| = \sqrt{2(E-V_0)}$), and $\vec{g}$ as follows,

$$\vec{k}^{\pm}_{\vec{g}/\!/} = \vec{k}_{0/\!/} + \vec{g}, \qquad \vec{k}^{\pm}_{\vec{g}z} = \pm\left[2(E-V_0) - \left|\vec{k}^{\pm}_{\vec{g}/\!/}\right|^2\right]^{1/2} \qquad \text{(A.18)}$$

where $\vec{k}^{+}_{\vec{g}}$ is the wave going inward of a crystal and $\vec{k}^{-}_{\vec{g}}$ is the wave going outward.

F-4. Stacking of successive layers

Once the individual layer diffraction matrices are known, the total diffraction can be calculated by a stacking of such layers. Relatively time saving and most frequently used method is either the Renormalized Forward Scattering (RFS) perturbation method$^{56)}$ or the Layer Doubling method$^{57)}$.

The RFS perturbation method applicable when the forward scattering is relatively dominant is the useful and very rapid method. Figure.49(a) shows a principle of this perturbation method. An incident electron penetrates into a crystal up to decay sufficiently. The lowest order perturbation for diffracted beam intensity contains all paths that have been reflected only once, but transmitted any number of layers. The second order contains only triple-reflection paths, and so on. This procedure is repeated for higher order until the total reflected amplitude converges. If the diffraction matrices mentioned above are rewrited as follows,

$$M^{++}=t^{++}, \quad M^{--}=t^{--}, \quad M^{-+}=r^{-+}, \quad M^{+-}=r^{+-}, \qquad (A.19)$$

the plane wave amplitude, $a_{(i)\vec{g}}$, in the i-th interlayer spacing is

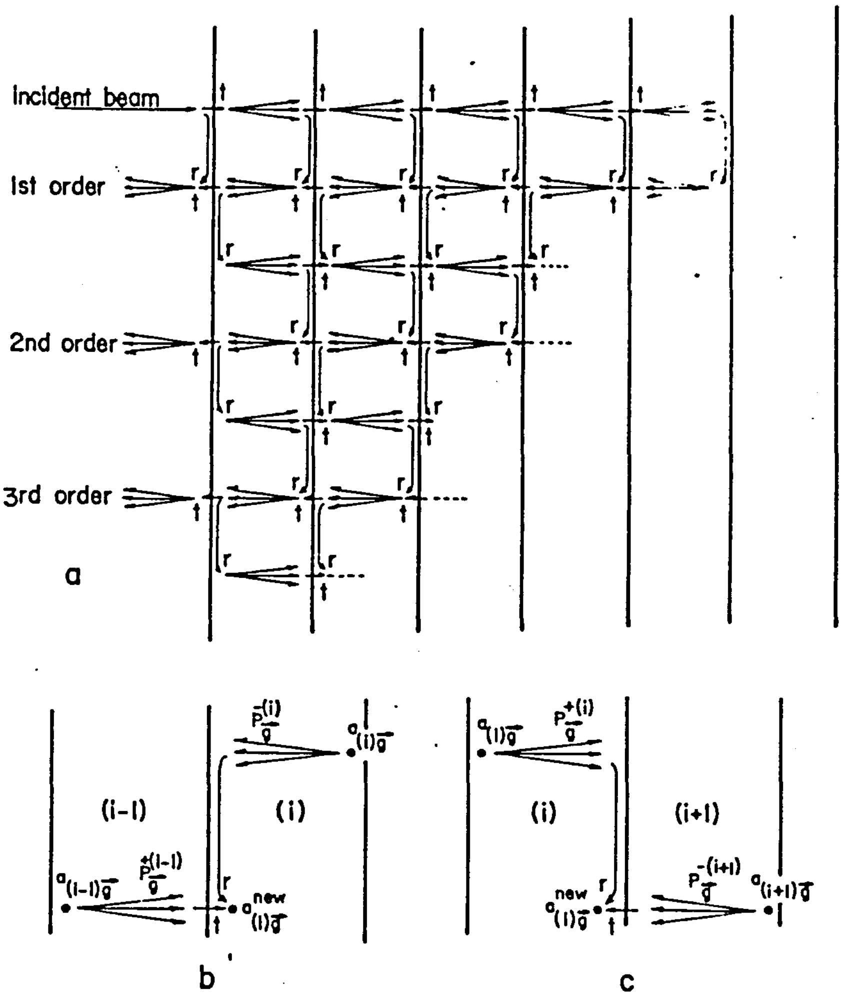

Fig.49 Mechanism of the Renormalized Forward Scattering perturbation method[3), (a) overall scheme, (b) and (c) details of each propagation step for penetration into and emergence out of the surface, respectively.

computed iteratively using two expressions, one for penetration (Fig.49(b)),

$$a_{(i)\vec{g}}^{new} = \sum_{\vec{g}'} \left[t_{\vec{g}\vec{g}'}^{++} P_{\vec{g}'}^{+(i-1)} a_{(i-1)\vec{g}'} + r_{\vec{g}\vec{g}'}^{+-} P_{\vec{g}'}^{-(i)} a_{(i)\vec{g}'} \right] \qquad (A.20)$$

and one for emergence (Fig.49(c)),

$$a_{(i)\vec{g}}^{new} = \sum_{\vec{g}'} \left[t_{\vec{g}\vec{g}'}^{--} P_{\vec{g}'}^{-(i+1)} a_{(i+1)\vec{g}'} + r_{\vec{g}\vec{g}'}^{-+} P_{\vec{g}'}^{+(i)} a_{(i)\vec{g}'} \right] \qquad (A.21)$$

where $P_{\vec{g}}^{\pm(i)}$ are the plane wave propagators between appropriate reference points on successive layers. By counting the surface barrier as i=1, the initial values for the iteration are,

$$a_{(i)\vec{g}}=0 \quad \text{for all } i,\vec{g} \quad \text{except } a_{(1)\vec{0}}=1 \qquad (A.22)$$

The RFS perturbation scheme uses typically about 10 layers and 3-4 orders of iteration for convergence and requires relatively small amounts of computation memories and time. This method fails, however, to converge well when the multiple scattering between any pair of successive layers is very strong and/or when an interlayer spacing becomes small (<1.0Å), because of requirement many evanescent plane waves for the description of the wave field. Under these conditions, the Layer Doubling method is more reliable than the RFS method.

Calculating mechanism of layer doubling is shown in Fig.50. Two different layers A and B which stack alternately are considered, and each layer has reflection and transmission amplitudes, r_A^{+-}, r_A^{-+}, t_A^{++}, t_A^{--} and r_B^{+-},r_B^{-+}, t_B^{++}, t_B^{--}, respectively. The combined pair has the diffraction amplitudes given by the following matrix equations,

$$R^{-+} = r_A^{-+} + t_A^{--} P^- r_B^{-+} P^+ (1 - r_A^{+-} P^- r_B^{-+} P^+)^{-1} t_A^{++},$$

$$T^{++} = t_B^{++} P^+ (1 - r_A^{+-} P^- r_B^{-+} P^+)^{-1} t_A^{++},$$

$$R^{+-} = r_B^{+-} + t_B^{++}P^{+}r_A^{+-}P^{-}(1 - r_B^{-+}P^{+}r_A^{+-}P^{-})^{-1}t_B^{--},$$

$$T^{--} = t_A^{--}P^{-}(1 - r_B^{-+}P^{+}r_A^{+-}P^{-})^{-1}t_B^{--}, \qquad (A.23)$$

where P^+ and P^- are the diagonal matrices propagating the plane wave from an atom center in layer A to an atom center in layer B and vice versa. Multiple scattering between the layers is taken into account exactly by the matrix inversion. For iteration, the results on the left-hand side of eq.(A.23) are substituted into the right-hand sides to produce new left-hand sides, and so on.

The Layer Doubling method consumes also much time owing to many evanescent waves for the description of the wave field when an interlayer spacing becomes more small (< 0.5Å). For that case, the combined space method for composite layer should be constituted.

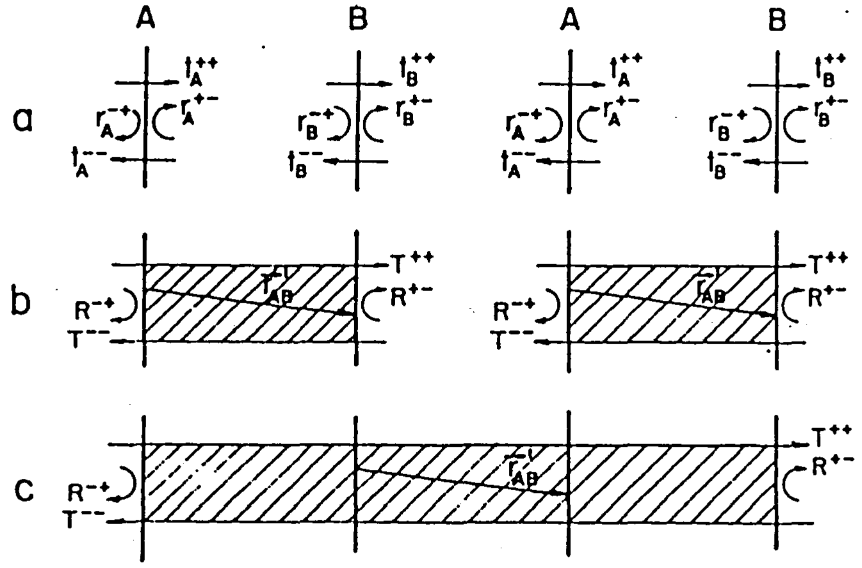

Fig.50 Mechanism of Layer Doubling.3)

F-5. Combined space method for composite layer$^{58)}$

The combined space method divides layers of a crystal into two groups. Multiple scattering within a layer having plural planes of small interplaner separation (composite layer; this includes the case of plural atoms per unit cell within a plane) is solved in the angular momentum space (L-space) representation using matrix inversion or iterations (Reverse Scattering Perturbation; RSP). On the other hand, multiple scattering between other crystal layers separated by larger interlayer spacing is solved in k-space representation using the RFS perturbation or the Layer Doubling method.

A composite layer with N subplanes (all subplanes have identical Bravais lattice, but their atoms may be of different species) is considered. Accordingly, if a unit cell being in a plane has n atoms, n subplanes are considered. If $T_{LL'}^{i}$ is defined as the scattering matrix including all those scattering paths within the composite layer and terminating at the subplane i in the spherical wave ($L=(\ell,m)$) representation, the diffraction matrix elements $M_{\vec{g}\vec{g}'}^{\pm\pm}$ for the entire composite layer are obtained,

$$M_{\vec{g}'\vec{g}}^{\pm\pm} = -\frac{16\pi^2 i}{A}\sum_{LL'}\frac{Y_L(\Omega(\vec{k}_{\vec{g}'}^{\pm}))\,Y_{L'}^{*}(\Omega(\vec{k}_{\vec{g}}^{\pm}))}{\vec{k}_{\vec{g}z}^{+}}\sum_{i=1}^{N}[R_{\vec{g}'}^{i\pm}(R_{\vec{g}}^{i\pm})^{-1}\,T_{LL'}^{i}], \qquad (A.24)$$

where

$$R_{\vec{g}}^{i\pm} = \exp(\pm i\vec{k}_{\vec{g}}^{\pm}\,\vec{r}_i). \qquad (A.25)$$

$T_{LL'}^{i}$ is connected with the scattering matrix, $\tau_{LL'}^{i}$, contains all scattering paths within a subplane i, and $\tau_{LL'}^{i}$ is connected with the scattering t-matrix of a single atom in the subplane i,

$$t_{\ell}^{i} = \frac{1}{2|\vec{k}_0|}\exp(i\delta_{\ell}), \qquad |\vec{k}_0| = \sqrt{2(E - V_{0r} - iV_{0i})}. \qquad (A.26)$$

F-6. Temperature effect

The effect of thermal vibrations is represented by the Debye-Waller factor e^{-M}. The relation between the two sets of phase shifts $\delta_\ell(T)$ and $\delta_\ell(0)$ is given$^{2)}$ by,

$$\exp(i\delta_\ell(T))\sin\delta_\ell(T) = \sum_{\ell'\ell''} i^{\ell'}\exp(-2\alpha\kappa^2)\ j_{\ell'}(-2i\alpha\kappa^2)$$

$$\times \exp(i\delta_{\ell''}(0))\sin\delta_{\ell''}(0)\left[\frac{4\pi(2\ell'+1)(2\ell''+1)}{(2\ell+1)}\right]^{\frac{1}{2}} B^{\ell''}(\ell'0,\ell0), \quad (A.27)$$

where $\kappa^2=|2(E-V_0)|$, $B^{\ell''}(\ell'0.\ell0)$ is given by eq.(A.16), j_ℓ is the spherical Bessel function of first kind. In the case that thermal vibrations are isotropic,

$$\exp(-M_x) = \exp(-\alpha|\vec{k}-\vec{k}'|^2), \quad (A.28)$$

and in the high temperature limit (Θ_D/T is small),

$$\alpha \simeq \frac{3h^2T}{2mk_B\Theta_D^{\ 2}}\ , \quad (A.29)$$

or in the low temperature limit,

$$\alpha \simeq \frac{3h^2}{2mk_B\Theta_D}\left(\frac{1}{4} + 1.642\frac{T^2}{\Theta_D^{\ 2}}\right)\ , \quad (A.30)$$

where k_B is the Boltzman factor and Θ_D is the Debye temperature. The high temperature limit is more appropriate to most of LEED experiments.

$\delta_\ell(T)$ calculated in this way is not real. The imaginary component is always positive, therefore, less flux is scattered than is incident on the ion-core, that is, the flux conservation in the scattering process is sacrificed.

Appendix G. Accuracy of calculations on diffracted intensity

G-1. Examples of calculations for different set of parameters

In order to confirm that the I-V curve calculated by a rather

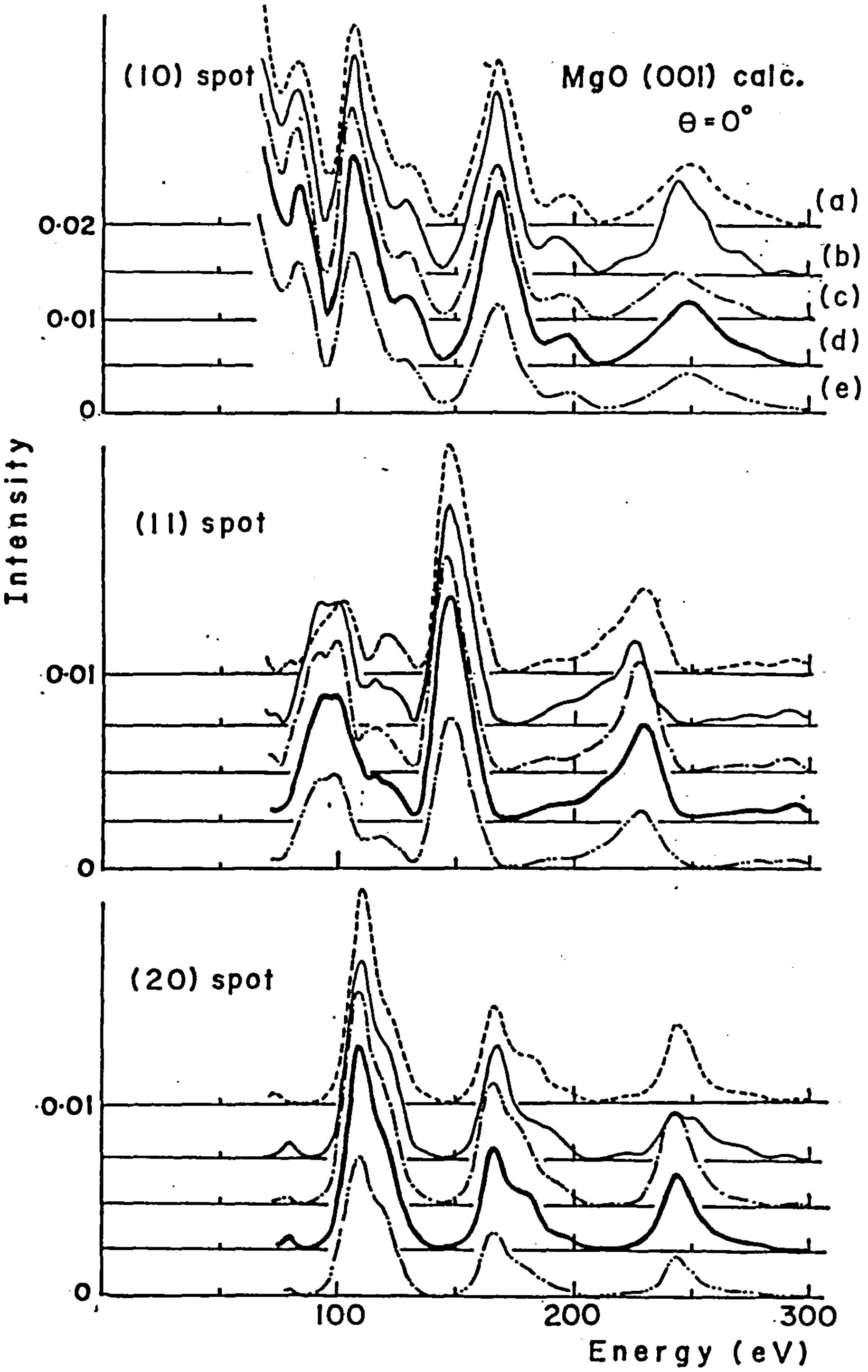

Fig.51 Calculated I-V curves of (10), (11) and (20) beams for MgO(001) surface. Curve d is calculated under the following conditions; (i) phase shifts of the Hartree-Fock approximation are used, (ii) 29 beams are included, (iii) ℓ_{max}=4, (iv) T=0K. Other curves are calculated by using one different parameter in comparison with the curve d, namely, curve a: phase shifts of the Hartree approximation are used, curve b: 69 beams are included, curve c: ℓ_{max}=6, curve e: T=400K (Θ_D=900K).

simple set of parameters has a sufficient accuracy for the present purpose, several theoretical curves have been calculated for different or more improved parameters. Examples of them are shown in Fig.51. Curve d is a standerd one. Other curves are calculated using one different parameter in comparison with the curve d. Namely, curve a is calculated using the phase shifts obtained by the Hartree approximation. Curve b is calculated including 69 beams. Curve c is the result of the calculation using 7 phase shifts ($\ell_{max}=6$). Curve e is calculated using the phase shifts in which a temperature effect (T=300 K) is included. The Debye temperature is assumed to be 900 K.

These curves are very similar to curves d except in some respects. For example, one can see that the profile of (11) spot of curve a in energy region lower than 100eV is not same. It seems that what kind of potential is used for the calculation of phase shifts is very impotant in low energy region, but hardly causes influence upon the curve in the energy region higher than 100eV. Kinniburgh$^{29)}$ has pointed out that the calculations excluding exchange potential were better. However, measurements in such low energy region have been impossible in this study. Some other difference will be discussed when it is appropriate in the text.

G-2. Comparison between RFS perturbation and Layer Doubling methods

As mentioned in Appedix F-4, multiple scattering between successive layers is dealed with the RFS perturbation method or the Layer Doubling method. I-V curves based on two methods are compared as an example of calculations for Fe(001) surface shown in Fig.52. Because these curves are very similar, the RFS perturbation method is good enough for the case of large layer spacing, namely, d =1.43Å for Fe(001) surface.

By the way, in comparison with the kinematical calculations for the same surface structure and the scattering condition in Fig.48, there are many notable respects, namely, appearance of many peaks and shoulders, a broadening of the peak width and the change of relative intensities etc.

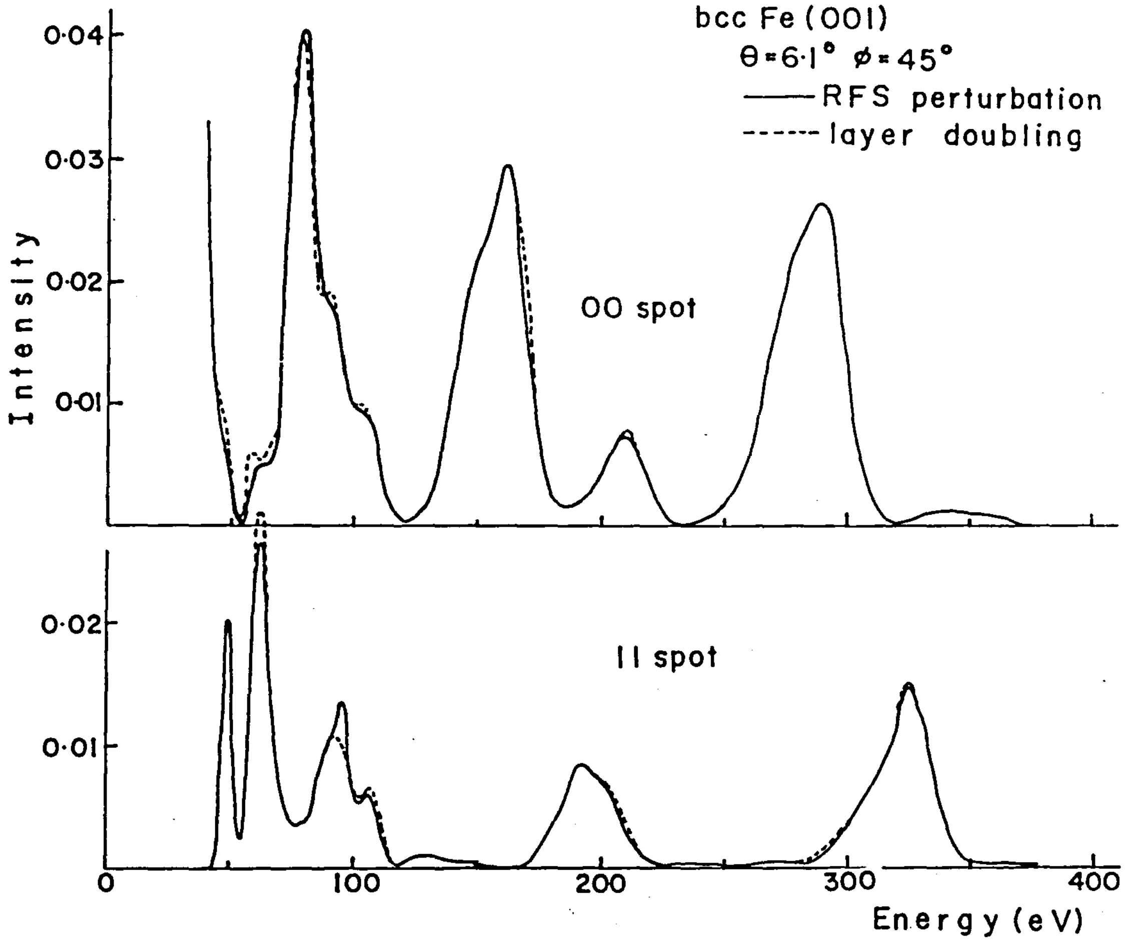

Fig.52 Calculated I-V curves for bcc Fe(001) surface by different layer stacking methods of RFS perturbation and Layer Doubling.

Appendix H. Final state effect; angular distribution of photoemission from atoms

According to Liebsch$^{8)}$, the interaction of the outgoing wave with the atomic potential causes the final state to consist of a superposition of spherical waves,

$$\psi_f(r) = 4\pi \sum_{L}^{\infty} Y_L(\Omega(\vec{k}_f))(-i)^{\ell}\exp(i\delta_\ell)R_\ell{}^f(\kappa r)Y_L(\Omega(\vec{r})), \qquad (A.31)$$

where $R_\ell{}^f(\kappa r)$ is the radial solution of Schrodiger equation. Inserting eq.(A.31) into eq.(3.1), the differential cross section can be written in the form,

$$\frac{d\sigma}{d\Omega} \sim \Big| \sum_{m=-1}^{1} Y^*_{1m}(\Omega(\vec{A})) \sum_{L_f} Y_{L_f}(\Omega(\vec{k}_f))(-i)^{\ell_f}\exp(i\delta_{\ell_f})R_{\ell_f\ell_i} I(1m,L_fL_i)\Big|^2 \qquad (A.32)$$

where the identity,

$$\frac{\vec{A}}{|\vec{A}|} \cdot \frac{\vec{r}}{|\vec{r}|} = \frac{4\pi}{3} \sum_{m=-1}^{1} Y^*_{1m}(\Omega(\vec{A}))\ Y_{1m}(\Omega(\vec{r})) \qquad (A.33)$$

is used. The angular momentum of the initial state is denoted by $L_i=(\ell_i,m_i)$ and $R_{\ell_f\ell_i}$ is the radial matrix element. The Gaunt coefficient,

$$I(1m;L_f,L_i)=\int d\Omega_r Y_{\ell m}(\Omega(\vec{r}))Y_{L_f}(\Omega(\vec{r}))Y_{L_i}(\Omega(\vec{r})), \qquad (A.34)$$

determines the selection rules imposed by the transition process,

$$\ell_f = \ell_i + 1$$
$$m_f = m - m_i\ , \qquad (A.35)$$

where m specifies the orientation of the polarization vector of light.

References

1) H.Sakama, A.Kawazu and K.Ueda; Phys.Rev.B34(1986)1369
2) J.B.Pendry; Low Energy Electron Diffraction (Academic press, London, 1974)
3) M.A.Van Hove and S.Y.Tong; Surface Crystallography by LEED (Springer-Verlag, Berlin,1979)
4) B.Feuerbacher, B.Fitton and R.F.Willis ed; Photoemission and the Electronic Properties of Surfaces (John Wiley & Sons, Chichester, 1978)
5) M.Aono, T.C.Chiang, J.A.Knapp, T.Tanaka and D.E.Eastman; Solid State Commun. 32(1979)271
6) K.Jacobi, C.v.Muschwitz and K.Kambe; Surface Sci. 93(1980)310
7) K.Kambe; Surface Sci. 86(1979)620
8) A.Liebsch; in ref.4, p.167
9) G.Ottaviani; J.Vac.Sci.Technol. 16(1979)1112
10) S.S.Lau, J.S.-Y.Feng, J.O.Olowolafe and M.-A.Nicolet; Thin Solid Films 25(1975) 415
11) M.Onellion, M.A.Thompson, J.L.Erskine, C.B.Duke and A.Paton; Surface Sci. 179(1987)219
12) G.J.Mate, P.Pestana and M.Kiwi; Phys.Rev.B26(1982)3841
13) C.L.Fu, A.J.Freeman and T.Oguchi; Phys.Rev.Letters 54(1985)2700
14) C.Binns, P.C.Stephenson, C.Norris, G.C.Smith, H.A.Padmore, G.P.Willams and M.-G.Barthes-Labrousse; Surface Sci. 152/153(1985)237
15) H.Namba and Y.Murata; J.Vac.Soc.Japan 20(1977)419 (in Japanese)
16) H.Ehrhardt, L.Langhams, F.Linder and H.S.Taylor; Phys.Rev. 173(1968)222
17) H.Suzuki and K.Wakiya; BUTSURI(Phys.Soc.Japan) 28(1973)705 (in Japanese)
18) K.Ueda; OYO BUTURI (Japan Soc.Appl.Phys.) 47(1978)690 (in Japanese)
19) W.Berndt; Rev.Sci.Instrum 53(1982)221
20) E.Lang, P.Heilman, G.Hanke, K.Heinz and K.Muller; Appl.Phys. 49(1979)287
21) Y.Murata; to be published
22) Y.Kanaji, H.Nakatsuka, T.Urano and Y.Taki; Surface Sci. 86(1979)587
23) P.W.Palmberg and T.N.Rhodin; J.Appl.Phys. 39(1968)2425
24) D.C.Jackson, T.E.Gallon and A.Chambers; Surface Sci. 36(1973)381
25) T.Kanaji, T.Urano, A.Hiraki and M.Iwami; Proc.8th Int.Vac.Congr.(Cannes,Sept, 1980)vol.I,p.117
26) A.Schulz, R.Courths, H.Schulz and S.Hufner; J.Phys.E, Metal Phys. 9(1979)L41
27) T.Kanaji, T.Kagotani and S.Nagata; Thin Solid Films 32(1976)217
28) K.O.Legg, M.Prutton and C.G.Kinniburgh; J.Phys.C7(1974)4236
29) C.G.Kinniburgh; J.Phys.C8(1975)2382
30) C.G.Kinniburgh; J.Phys.C9(1976)2695
31) W.Berndt; Proc.8th Int.Vac.Congr. (Cannes, Sept., 1980)p.1133

32) M.R.Welton-Cook and M.Prutton; Surface Sci. 74(1978)276

33) Y.Murata, S.Murakami, H.Namba, T.Gotoh and K.Kinosita; Proc.7th Int.Vac.Congr. (Vienna,1977)p.2439

34) T.Gotoh, S.Murakami, K.Kinosita and Y.Murata; J.Phys.Soc.Japan 50(1981)2063

35) Y.Murata; J.Phys.Soc.Japan 51(1982)1932

36) M.R.Welton-Cook and W.Berndt; J.Phys.C15(1982)5691

37) F.Herman and S.Skillman; Atomic Structure Calculations (Prentice Hall, Englewood Cliffs, NJ,1963)

38) C.Kittel; Introduction to Solid State Physics, 2nd ed.(Wiley,New York,1956)

39) C.Satoko, M.Tsukada and H.Adachi; J.Phys.Soc.Japan 45(1978)1333

40) P.W.Palmberg; Anal.Chem. 45(1973)549A

41) W.Okamoto and K.Terakura; private communication

42) M.Causa, R.Dovesi, C.Pisani and C.Roetti; Surface Sci. 175(1986)551

43) W.B.Peason; A Handbook of Lattice Spacing and Structures of Metals and Alloys (Pergamon press,London,1958)

44) S.Nakanishi and T.Horiguchi; private communication

45) J.W.Gadzuk; Phys.Rev.B10(1974)5030

46) A.Liebsch; Phys.Rev.B13(1976)544

47) E.N.Sickafus; Rev.Sci.Instrum. 42(1971)933

48) V.Heine; Phys.Rev. 153(1967)673

49) M.L.Tarng and G.K.Wehner; J.Appl.Phys. 44(1973)1534

50) G.E.Rhead; J.Vac.Sci.Technol. 13(1976)603

51) J.L.Beeby; J.Phys.C1(1968)82

52) R.S.Zimmer and B.W.Holland; J.Phys.C8(1975)2395

53) E.G.McRae; Surface Sci. 11(1968)479

54) D.W.Jepsen, P.M.Marcus and F.Jona; Phys.Rev.Letters 26(1971)1365

55) K.Kambe; Z.Naturf. 22a(1967)332

56) J.B.Pendry; J.Phys.C4(1971)3095

57) M.A.Van Hove and J.B.Pendry; J.Phys.C8(1975)1362

58) S.Y.Tong and M.A.Van Hove; Phys.Rev.B16(1977)1459